Université Lille I - Sciences et Technologies

Laboratoire de Mécanique de Lille (UMR CNRS 8107)

École Doctorale Science Pour l'Ingenieur Lille Nord-de-France

Année 2015 - N° d'ordre : 41911

Thèse

Pour l'obtention du grade de

Docteur de l'Université Lille I - Sciences et Technologies

Discipline : Génie Civil

présentée par:

Mahban Sadat HOSSEINI

Numerical simulation of hydro-mechanical behaviour of nano porous materials: Application to cement paste

---

Soutenue publiquement le 2 décembre 2015 devant le jury composé de

J.M. Torrenti	Professeur, IFSTTAR	Rapporteur
F. Benboudjema	Professeur, ENS Cachan	Rapporteur
J.F. Georgin	Maître de Conférences, INSA de Lyon	Examinateur
T. Rougelot	Maître de Conférences, Université Lille 1	Examinateur
N. Burlion	Professeur, Université Lille 1	Directeur de thèse
J.B. Colliat	Professeur, Université Lille 1	Directeur de thèse

Laboratoire de Mécanique de Lille
Boulevard Paul Langevin, Cité Scientifique, 59655, Villeneuve d'Ascq cédex

Acknowledgements

Though only my name appears on the cover of this dissertation, a great many people have contributed to its production. I owe my gratitude to all those people who have made this dissertation possible and because of whom my graduate experience has been one that I will cherish forever.

I would like to express my deepest gratitude to my advisor, Pr. Jean-Baptiste COLLIAT, for his excellent guidance, caring, patience, and providing me with a perfect environment for doing research. His guidance was useful to me from the beginning of the research and throughout the writing of this thesis. I would like to thank Pr. Nicolas BURLION, who let me experience the research in this field and helping me to develop my background in experimental field. I would like to thank Dr. Thomas ROUGELOT, who as a good friend, was always willing to help and give his best suggestions.

I would also like to thank my friends in Lille and my colleagues in LML. Their support and care helped me overcome setbacks and stay focused on my graduate study. I greatly value their friendship and I deeply appreciate their kindness in exchange of knowledge, skills and for all the fun we have had in the last three years. I am also grateful to the former and current staff at Polytech'Lille and LML, for their various forms of support during my graduate study.

Last but not the least, I would also like to thank my family for the support they provided me through my entire life and in particular, I must acknowledge my husband and best friend, Hamid, without whose love and encouragement, I would not have finished this thesis.

Abstract

One of the most important issues in civil engineering about structures is their durability. A structure during his lifetime faces different environmental situations, like different relative humidities. Thus, it is crucial to characterize materials behaviour like the shrinkage against these changes. Some information are needed to predict it. One of the principal information is the sorption-desorption isotherm. In cement-based materials just as cement paste after the hydration process, there remain generally extremely fine pores in the material. Consequently obtaining isotherm experimentally is considered as a substantially time-consuming experience.

Therefore, it is of interest to model the isotherm from a numerical point of view. A hysteresis is also noticeable between the curves of sorption and desorption. This phenomenon is related to the structure of the porous network and the presence of ink-bottle pores. It has been shown throughout different researches that it strongly depends on particular details of the pores geometry. This physical phenomenon with such complicated effects makes complications in the modelling of isotherm hysteresis. This has been a field of study of intense researches. However, there are not many models relying on true physical effects which take place during drying and saturation.

In the present work, in order to model a porous media, a numerical morphology of the geometry of the porous media has been presented by means of a Random Field excursion. Random Field parameters are defined based on experimental values. The advantage of this study is to model the porous network without any assumption on the shape of pores. Once the porous media has been reproduced, the morphological analysis must be done in order to model water transfers. Following the simulation of sorption-desorption isotherm, the second step is to evaluate strains induced due to desiccation and to find an estimation of drying shrinkage. For mechanical simulations, capillary pressure, and disjoining pressure were considered as the intervening physical phenomena. Finally the macroscopic shrinkage in terms of relative humidity was obtained by applying these forces on the porous network at microscopic scale.

Resumé

Un des points les plus importants en génie civil concerne la durabilité des structures. Au cours de sa vie, une structure est confrontée à différentes situations environnementales, tels que différentes humidités relatives. Il est donc crucial de caractériser le comportement des matériaux tels que le retrait par rapport à ces changements. Certaines informations sont nécessaires afin de pouvoir prédire cela. Une des principales informations est l'isotherme de sorption-désorption. Dans les matériaux à base de ciment, tout comme la pâte de ciment après le processus d'hydratation, il reste généralement des pores extrêmement fins dans le matériau. Par conséquent, obtenir l'isotherme expérimentalement est considéré comme une expérience coûteuse en temps.

C'est pour cette raison que la modélisation numérique de l'isotherme porte un grand intérêt. Une hystérésis est également perceptible entre les courbes de sorption et de désorption. Ce phénomène est lié à la structure du réseau poreux et la présence des petits pores se trouvant enfermés derrière les grands pores (des pores de bouteille d'encre). Il a été démontré tout au long de différentes recherches qu'il dépend fortement des détails particuliers de la géométrie des pores. Ce phénomène physique avec ces effets complexes entraîne beaucoup de complications dans la modélisation de l'hystérésis d'une isotherme. Ce fut un champ d'étude de recherches intensives. Pourtant, il n'y a pas beaucoup de modèles reposant sur de véritables effets physiques qui ont lieu au cours du séchage et de la saturation.

Dans cette thèse, afin de modéliser un milieu poreux, une morphologie numérique de la géométrie du milieu poreux a été présentée par l'intermédiaire d'une excursion de champs aléatoires. Les paramètres du champ aléatoire sont basés sur les valeurs expérimentales. L'avantage de cette étude est de modéliser le réseau poreux sans aucune hypothèse sur la forme des pores. Une fois que les milieux poreux ont été reproduits, l'analyse morphologique doit être effectuée afin de modéliser les transferts d'eau. À la suite de la simulation de l'isotherme de sorption-désorption, la deuxième étape consiste à évaluer les déformations induites par la dessiccation et de trouver une estimation du retrait de dessiccation. Pour les simulations mécaniques, la pression capillaire et la pression de disjonction ont été considérées comme les phénomènes physiques intervenants. Finalement, le retrait macroscopique a été obtenu en fonction de l'humidité relative en appliquant ses forces sur le réseau poreux.

Contents

Principal Notations

$f(x)$	Random function
M	Definition domain of random function
σ^2	Variance
$\mathcal{C}$	Covariance function
L_c	Correlation length
D	Hitting set
$\mathbf{A_D}$ or $\mathbf{A}$	Excursion set
u	Level set value
$\mathcal{L}_0, \mathcal{L}_1, \mathcal{L}_2, \mathcal{L}_3$	Characteristic values of morphology
$\mathbf{S}$	Binary set
Ei	Structuring element with size i
$\ominus$	Erosion
$\oplus$	Dilation
$\bullet$	Opening
$\circ$	Closing
$\mathbf{I}$	Marker
$\mathbf{C}$	Mask
$\delta_E(\mathbf{A})$	Dilation applied on set $\mathbf{A}$ considering structuring element of size E
$R_E(\mathbf{A})$	Geodesic reconstruction applied on set $\mathbf{A}$ considering structuring element of size E
w	Water content
RH	Relative humidity
m	Mass
S_w	Water saturation degree
P_g	Gas pressure
P_{atm}	Atmospheric pressure
M	Molar mass
R	Perfect gas constant
T	Temperature
ρ	Density
r_c	Capillary radius
δ	Thickness of adsorbed water layer
$\mathbf{V}_i^d$	Drained volume during drying at RH level i
$\mathbf{V}_i^f$	Filled volume during wetting at RH level i
γ_0	Surface energy of the solid without adsorbed water
γ	Surface energy of the solid with adsorbed water
A	Constant corresponding the material and its structure
L_0	Initial length
L_{RH}	Measured length at certain relative humidity
$\epsilon(RH)$	Deformation at certain relative humidity
$\epsilon_v(RH)$	Volume deformation at certain relative humidity
P_c	Capillary pressure
ρ_l	Density of water

M_l	Molar mass of water
P_d	Disjoining pressure
P'_d	Modified disjoining pressure considering pore size
ρ_a	Density of adsorbed water
M_a	Molar mass of adsorbed water
E_e	Elastic strain energy
V_p	Pore volume in which pressure P is applied
σ	Stress
ϵ_{rd}	Strain due to drying
d	Pore diameter
$\underline{\underline{\underline{\underline{C}}}}$	Elasticity tensor
E	Modulus of elasticity (Young's modulus)
ν	Poisson's ratio
μ, λ	Lamé constants
$\mathbf{M}_i$	Set representing meniscus places at relative humidity level i
$\mathbf{V}_i$	Set representing volume of pores with size i

- **Abbreviations**:

MAT1	2D porous network consists of one excursion set ($L_c = 0.003\mu m$) with the porosity of 56%
MAT2	2D porous network consists of two excursion sets union ($L_c = 0.003, 0.05\mu m$) with the porosity of 56%
MAT3	2D porous network consists of five excursion sets union ($L_c = 0.011, 0.02, 0.03, 0.05, 0.07\mu m$) with the porosity of 40%
MAT4	2D porous network consists of seven excursion sets union ($L_c = 0.003, 0.005, 0.008, 0.011, 0.02, 0.03, 0.05\mu m$) with the porosity of 56%
MAT5	3D porous network consists of eight excursion sets union ($L_c = 0.005, 0.009, 0.012, 0.02, 0.04, 0.065, 0.1, 0.15\mu m$) representing cement paste with $W/C = 0.8$ and the porosity of 32%
MAT6	3D porous network consists of eight excursion sets union ($L_c = 0.005, 0.008, 0.011, 0.015, 0.025, 0.04, 0.07, 0.12\mu m$) representing cement paste with $W/C = 0.5$ and the porosity of 25%

Note: In this document, the term 'Adsorption' corresponds to the adhesion of atoms, ions, or molecules from a gas or liquid to a surface. This process creates a film of the adsorbate on the surface of the adsorbent. It differs from the term 'sorption' which corresponds to the wetting process in this document. Adsorption is a surface-based process while sorption involves the whole volume of the material.

General Introduction

Cement-based (or cementitious) materials such as concrete, mortar and cement paste are widely used in the field of civil engineering, i.e. buildings, bridges, tunnels and other structures. During their lifetime, these structures or their components are subjected not only to mechanical loading, but also to variations of temperature and relative humidity (RH). These changes have a great influence on their durability, which is one of the most important issue related to civil engineering structures. This is particularly true for applications such as nuclear power plants, disposal and storage of radioactive wastes.

Drying phenomenon leads to several effects on the cement-based materials:

- It produces deferred deformations: drying shrinkage and drying creep. These deformations lead to losses of pre-stress and can increase the displacement.
- The skin area of concrete tends to shrink more than the central areas. The consequences are the creation of tensile stresses in skin and compressive stresses in center. Micro cracks on the surface can affect the mechanical properties and the mass transfer (diffusion, permeation).
- The saturation degree has an important influence on the gas transfer properties and the diffusion coefficient.
- The saturation degree also has influences on pathologies such as Alkali–silica reaction or internal sulphate attack.

Considering more specifically the change of RH, cement-based materials exhibit, at the macroscale, a quite complex behaviour which can be presented through their sorption-desorption isotherms. The latter are the curves describing water content in terms of RH. They are obtained by applying different relative humidity levels on the material sample and measuring its mass at each step during drying and wetting after achieving equilibrium. Typically, it takes a couple of years to dry and re-humidify a material specimen of a few centimeters size, and usually several cycles are required. In order to reduce this time, a statistical based strategy has been proposed at LML [1, 2] to reduce samples size and thus to achieve equilibrium states faster. However, recognizing complete experimental characterization of the hydro-mechanical response of these materials is still a long lasting process. Another solution is the numerical simulation of both the drying and wetting processes, which is the objective that this thesis is trying to contribute to.

At the microscale, cement-based materials are consisting of a very fine and narrow pores in their structures, which spans more than five orders of magnitude in size. Actually, the smaller pores are not larger than a few nanometers, thus leading to consider cementitious materials to belong to the nanoporous materials class. According to the IUAPC isotherms are classified in 6 major types which is illustrated in Fig. 1. Cement-based materials usually belong to type IV which corresponds to a solid whose porosity varies from a few nanometers to few micrometers.

Turning to numerical simulation of the drying/wetting process, one clearly faces two main challenges:

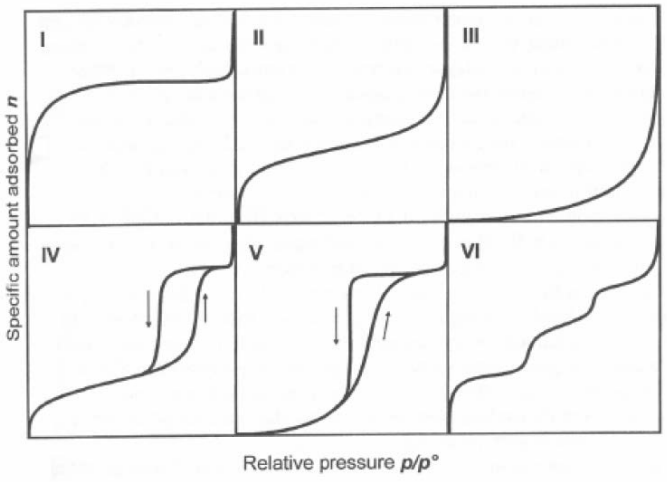

FIGURE 1: Isotherm classification by type (IUPAC 1985)

– Firstly, to model the mass transfer, mainly corresponding to a two-phase flow within tiny pores.

– Secondly, to accurately represent the complexity of the pore space geometry.

Tackling those two challenges at once is certainly not a new issue, but not a realistic one as well. In a paper in 1984, Matheron [3] already insisted on the main difficulty for a similar but simpler problem dealing with soils permeability: even if considering slow and permanent flows (thus allowing to use the simplified linear Navier flow equation), one needs to add some boundary conditions that are extraordinary complex due to the geometry of the pore space. Hence, facing the two previous challenges, two pragmatic and parallel strategies can be drawn:

– First to provide an accurate and complete description of the two-phases flow, within a simplified geometry. In the literature, it is developed for different materials such as soil [4], clay [5] and dentine infiltration [6, 7].

– Second to provide a fine and accurate description of the geometry of the pore space, combined to a simplified (mainly stationary in time) representation of the mass transfer. In some studies, they consider pores as spherical [8–10] or cylindrical objects [11].

The framework developed and presented in this thesis belongs to the second way. Clearly, we do believe that the apparent complexity of the sorption-desorption isotherms at macroscale (non-linearity, hysteritical effect, ...) is, at the first order, related to the complexity of the morphology of the pore space[1]. Moreover this 'direct' link between those two complexities (at micro and macroscale) is particularly true when dealing with equilibrium (stationary in time) states. So our strategy is twofold:

i) To provide a rich and accurate morphological (geometrical and topological) description of the pore space of a cement paste, through a digital 3D simulated image. It is worth noting

[1]Of course we do not pretend that the physics of the flows has no influence on the apparent hydro-mechanical behaviour of cementitious materials. Obviously it earns a large part of the kinetics related to drying or wetting.

that it would have probably been better to work on an experimental 3D representation. However, it is not possible at the moment because of shortcomings of observation methods at nanoscale.

ii) Based on this description that represents a very large amount of information, to extract (in the sense of image filtering) the pertinent data related to both drying and wetting. Typically those data can be the volume of water which is drained when applying a decrease of the environmental RH.

The first part of this framework requires a quite general and versatile morphological model. It is related to the excursion sets of Random Fields (RF), which both provide no limitation in shapes and a simple (in a statistical sense) control of geometrical and topological measures. This theory has been developed and applied for very different fields (see [12] for a review) and has recently been used by [13] and [14] for cementitious materials.

Turning to the second part, we propose to couple classical image filtering techniques to the laws that describe the simple mechanisms involved in the process of drying/wetting in the stationary case: Kelvin-Laplace law and adsorption layer. The right choice of filtering techniques is related to the so-called morpho-mathematical operations [15]. The latter are based on operations using a 'structuring element' for which the shape and size can be adapted to the physics we aim to describe.

This thesis is thus divided into five chapters as follows:

The first chapter presents a general review from the literature on the structure of cement-based materials and especially cement paste. Different components of these materials are addressed. Hydration process and changes in components due to hydration are explained and different types of water and porosity in materials are detailed. After specification of cement-based material structure, drying process and dimensional variations due to drying are discussed. In the following, some experimental protocols are reviewed in order to characterise hydro-mechanical behaviour of cement-based materials followed by a synthesis of obtained results from the literature [1, 2, 16–18].

In the second chapter a morphological model is proposed in order to represent the porous network with all its complexity and without any assumption on the shape of pores. The proposed model is based on excursions of Random Fields. Thus the definition of Random Fields and the excursion set are mentioned. A wide range of morphological models could be generated using this technique and the characteristic values of morphology are expressed in order to classify them. Then an application to nanoporous materials is performed by representing 2D morphological models. In order to analyse these morphological models, morpho-mathematical operations such as erosion, dilation, opening, geodesic reconstruction and geodesic distance are defined. Finally sensitivity of the morphological model to input data is evaluated.

Third chapter represents an application to cement-based materials and especially cement paste. The input data of these models are chosen considering experimental results like mercury intrusion. Thus the experimental protocol of this test is detailed and the obtained pore distribution

for cement paste with $W/C = 0.8$ and 0.5 are illustrated. Two morphological models are developed in 3D, representing cement paste with $W/C = 0.8$ and 0.5 respectively, and their similarity to the real material is investigated. Some properties like total porosity, open porosity, tortuosity and pore distribution are obtained numerically using morpho-mathematical operations. Then they are compared with experimental values in order to validate the numerical models.

The fourth chapter includes application to sorption-desorption isotherm. The physical definition and the associated phenomena are reviewed. Then appropriate morpho-mathematical operations are applied in order to simulate the material state during drying and wetting. In experimental results, a hysteresis between sorption and desorption isotherm is observed, which is induced due to the presence of ink-bottle pores. In the numerical modelling, the effect of these type of pores have also been taken into account and the hysteresis is simulated through numerical operations. At the end of this chapter the influence of adsorbed layer on the pore walls is studied and the sensitivity of sorption-desorption isotherm to the geometrical and physical parameters is evaluated.

The fifth chapter is dedicated to dimensional variations due to drying, and drying shrinkage is addressed to study the mechanical behaviour. The experimental protocol is reviewed in order to measure the drying shrinkage. Different drying mechanisms are explained and the numerical simulation is applied considering capillary pressure and disjoining pressure. In the following, the sensitivity of the obtained shrinkage is evaluated with the changes in the morphological model.

Finally, concluding remarks are made on the general framework, and perspectives are expressed in order to improve the numerical simulations.

Chapter 1

Microstructural characteristics of cement-based materials

Contents

1.1 Introduction

By definition, a material is called cement-based when the binding agent is a hydraulic cement. Concrete is composed of cement, water and aggregates, while mortar is composed of sand, cement and water. Aggregates have generally stable behaviour over time. Therefore, the behaviour of mortar or concrete is dependent on the physical structure and changes of the cement paste over time. Consequently, studying the cement paste behaviour against different changes is very important. Studying the material behaviour against water is one of the most important issue for a good understanding of physical phenomena in this type of materials, especially in order to assess the durability of a structure. Indeed, water is part of the material structure which cooperate in hydration process of the cement, and is present in various forms in the hardened material [19].

This chapter aims to provide a review on the structure of cement-based materials, characterization of the porosity and pore distribution. It also includes the different roles and states of water within these materials and the process associated with drying phenomenon. At the end of this chapter some experimental studies are reviewed and their results are synthesised.

1.2 Structure of cement-based materials

1.2.1 Portland cement

Cement results from the fine grinding of clinker and a small amount of calcium sulphate (about 5%) as a setting regulator. Clinker is obtained by a mixture of limestone (80%) and clay (20%) at high temperature (145°C). The limestone gives lime (CaO) while the clay provides silica (SiO_2), alumina (Al_2O_3) and iron oxide (Fe_2O_3). The four main clinker phases, which are not pure substances due to the presence of minor elements in the clay and limestone, are [20]:

- Tricalcium silicate Ca_3SiO_5 (C_3S) representing 50 to 70% of clinker weight
- Dicalcium silicate Ca_2SiO_4 (C_2S) representing 10 to 20%
- Tricalcium aluminate $Ca_3Al_2O_6$ (C_3A), which represents 8 to 10%,
- Tetracalcium aluminoferrite Ca_4AlFeO_5 (C_4AF) representing 5 to 15% of clinker weight.

1.2.1.1 Hydration process

Cement hydration is a set of chemical reactions that occur between cement and water. These reactions begin by mixing water and cement and they continue during curing. However they will be slower over the time. [21–24].

Adding water to cement causes hydration of its constituents, which becomes highly insoluble and also a stable and resistant binder from mechanical point of view is created. Numerous chemical

reactions take place during hydration, and its mechanism has been proposed by Le Chatelier [25].

In general, when cement is placed in contact with water, the surface of the cement grains is covered with water molecules. The cement components are then dissolved, and are found in the form of ions (calcium ion, hydroxyl, aluminates, silicates, and sulfate) in solution. When the ionic concentration exceeds the product solubility, ions precipitate as hydrates. This phenomenon continues until complete dissolution of the cement components. The kinetics of this hydration process decreases over time, because of a decrease in the diffusion of water to the hardened cement [1]. Thus, the maturation period of the material can be several months or even years. Fig. 1.1 shows the volumetric relations obtained in the study of Jensen and Hansen [26], for a hydrating cement paste at a high W/C ratio. W/C defines the water mass proportion depending on the amount of non-hydrated cement. This diagram corresponds to a closed system and there is not any transport of moisture in the cement paste. It gives the volume changes of various phases constituting a cement paste with the degree of hydration α. At the beginning of this reaction, only the non-hydrated cement and water are present. Then, capillary water reacts with the cement to form a hydrate gel (here decomposed into its solids fraction and its liquid fraction). By this reaction empty pores are generated in the cement paste structure and the volume of hydration products is smaller than the initial components. This 'chemical' contraction is known as Le Chatelier, and was quantified by Tazawa et al. [25] from the stoichiometric relationship of hydration of cement and by experimental measurements. A contraction of about 11% was determined. The reaction continues until all the capillary water react to form hydrates. Here the maximum degree of hydration α_{max} is equal to 1. This reaction may be incomplete in the case where the amount of water introduced in the initial mixture is not sufficient to hydrate all the cement. For example in the cement paste with W/C ratio less than 0.42 [27], this value may vary between 0.39 [28] and 0.44 [29].

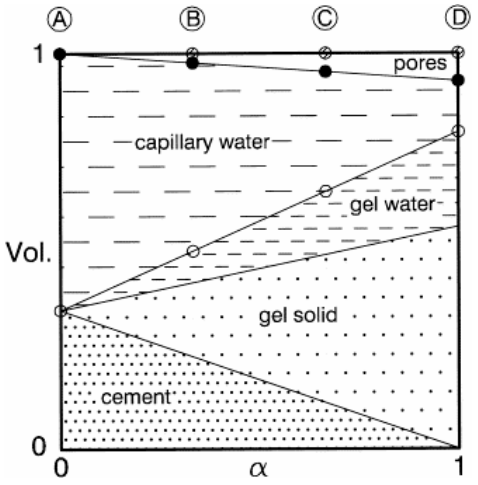

FIGURE 1.1: Volumetric phase distribution of cement paste as a function of the degree of hydration, at $W/C = 0.6$ [26]

1.2.1.2 Hydration products

The main hydrates created during the hydration process, according to research carried out by Powers and Brownyard [30], are:

- Hydrated calcium silicates (denoted 'CSH'), which constitute 50 to 70% of formed hydrates
- Calcium hydroxide (portlandite, denoted 'CH') which constitutes about 25% of hydrate
- Hydrated calcium aluminate (several forms such as C_4AH_{13}, C_2AH_8 and C_3AH_6)

CSHs form the major part of the hydrates which ensure the mechanical stability of the cement-based materials. The generally used observation technique are ineffective and the structure of CSH (mineralogical, molecular arrangement) is not exactly known. Several experimental approaches have been proposed in order to have the most accurate representation of their structure. For example, a study using nuclear magnetic resonance has been performed on the hydrate gel and its constituents to determine their microstructure [31–33]. The hydration process was also observed by electron microscopy in order to classifying hydration products [34].

CSHs are represented in the form of gels (low crystallinity and high proportion of water in their composition). The particles of CSH are layered micro crystals in which sheets consisting of 2 or 3 microcrystals linked by ionic bonds or surface forces. The proportion of mineral constituents of these CSHs depend on different parameters including the condition in which they were formed, the ratio of C/S in solution and the saturation degree of cement paste.

Based on the direct and indirect information and experimental observations, different models have been proposed for the structure of CSH [35–37]. They are generally represented CSH gel as sheets arrangement with the stored water between them. Fig. 1.2 shows the proposed model by Jennings [38] and the description of how water is contained within the particles. Fig. 1.2(I) illustrates single sheet of C-S-H with all evaporable water removed, and a saturated globule without water adsorbed on the surface. Fig. 1.2(II) also represents CSH structure during drying and rewetting (A: Fully saturated globule with monolayer on the surface, B: Partially dried with much of the interlayer water and monolayer removed, C: All evaporable water is removed to represent the dried state and D: Resaturated state.)

Fig. 1.3 is a schematic illustration of a globule and its immediate neighbours during ageing process. Time, drying, temperature and probably applied stress change the structural form the open to the tighter packs as represented on the right side of figure. During ageing the large gel pores are reduced in size and volume, the globules align.

Calcium hydroxide (portlandite) represents another significant part of hydrates. It presents in the form of hexagonal solid crystals between partially hydrated cement grains around pores or near aggregates. The rest of hydrates consists of different types of hydrated calcium aluminates, which formed as hexagonal plates or cubic crystals and hydrated calcium sulfo-aluminate [19].

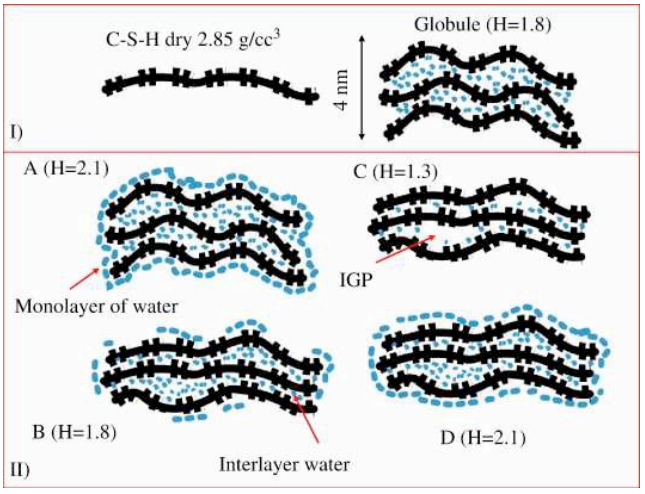

FIGURE 1.2: A schematic of a globule with water contents representing different relative humidities [38]

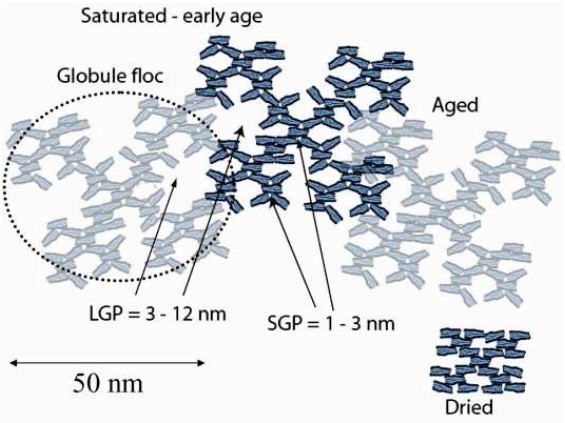

FIGURE 1.3: The ageing process schematically represented as progressing from left to right [38]

1.2.2 Porosity

In the hydration process of cement paste, the generated porous network depends on the arrangement of various hydration products. The porosimetric analysis of cement paste reveals two types of pore. Capillary pores, corresponding to the peak of large diameter, and pores of hydrates, corresponding to the peak of smaller diameter. Fig. 1.4 shows the pore distribution of cement paste for various W/C ratio. For higher W/C, the curve shifts to large diameters.

The capillary pores, whose diameter varies from a few hundred to thousands angstroms, are initially filled by the mixing water. For a given age, by increasing W/C ratio, the dimension and the volume of these capillary pores also increase, and for a given W/C ratio, the volume of capillary pores decrease during hardening of the material. The pores of hydrates represent the interlayer spaces. Their size is in the order of nanometer which depends on conditions of hydration, and thus is an intrinsic characteristic of formed hydrates. Increasing the amount

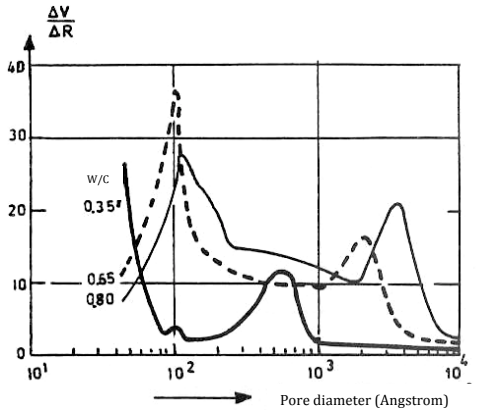

FIGURE 1.4: Pore distribution curve for cement pastes with different W/C [20]

of hydrates during maturation leads to an increase in the microporosity. The total volume represented by this intrinsic microporosity is about 26% of hydrates volume [20].

1.2.3 Water in hardened cement paste

Water is present in various forms in the hardened cement paste. Typically there are three types of water:

- Free water: Strongly ionized from the first moment, it exists in capillary pores (macropores) greater than 500 angstroms. It is drained by drying.
- Bound water: This type of water is associated with the hydration reaction of cement grains and it enters into the composition of hydrates.
- Adsorbed water: The attached water to the surface of solid, this attachment may be by physical or chemical binding forces.

Physical adsorption is introduced due to van der Waals forces. It is reversible and it is possible to have one or more layers on the surface of solid. In the chemical adsorption, there is a transfer or sharing of electrons. The adsorbed molecule is not in his free state and the involved energies are greater and longer lasting in this case. Accordingly, the chemically adsorbed water is considered as a bound water. Sierra [39] proposed a water distribution method in the structure of CSH, based on the model of Feldman and Sereda [40]. This distribution is shown in Fig. 1.5. It divides the water into three categories in descending order of binding energy with the solid.

- Hydroxylic water: It is located on the inner and outer faces of the sheets and is bonded to Si atoms or Ca atoms.
- Inter sheets water (or internal): It is fixed between the sheets by hydrogen bridges with hydroxyl.

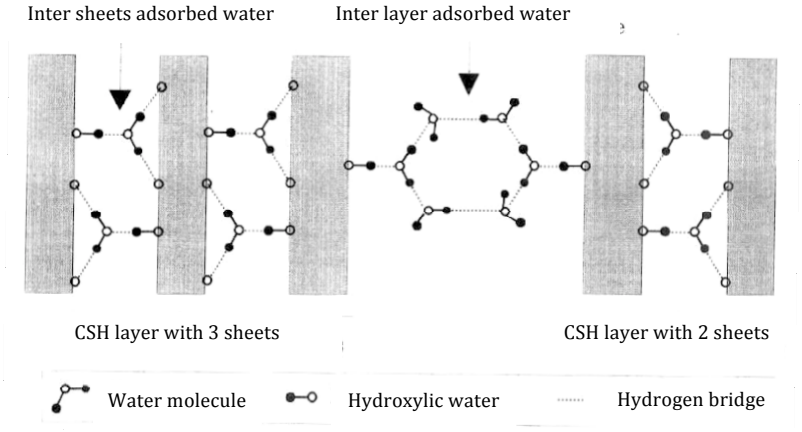

FIGURE 1.5: Water distribution in the structure of CSH [39]

- Inter layer water (or external): It is placed between the CSH layers and is subjected to the interlayer forces because of the small space between layers.

Another classification related to the characterization of porous network is often used [19]. It classifies water in two categories of evaporable and non-evaporable water (which remains in the material upon drying in an oven at $105°C$ [27]). In other way this classification consists of:

- Evaporable water: Free water and physically adsorbed water
- Non-evaporable water: Bound water and chemically adsorbed water

1.2.4 Cement paste-aggregate interface

Adding aggregates to cement paste creates a new zone in the material which is cement paste-aggregate interface also referred as Interfacial Transition Zone (ITZ). By the presence of aggregates, there is an excess water in the interface area which changes the hydration conditions in this zone. Therefore the structure of cement paste changes in the distance of few microns from aggregate surface. By increasing aggregate size or W/C ratio, this distance increases but it is always less than $50\mu m$. Porosity in this area is more than the porosity of other parts of cement paste, consequently it becomes one of the weakest points against mechanical or chemical actions, in the structure of usual concrete.

1.3 Drying process of cement-based materials

In order to have an appropriate mixture in ordinary concretes, the amount of water should be greater than that required to complete hydration. Thus, within the material, there is an amount of water which can evaporate when environmental relative humidity is lower than that prevailing in the material. Fig. 1.6 shows the water content change over time during drying, in

a concrete specimen. Water concentration gradient appears between the core and the surface in contact with the environment. These gradients are very strong on the surface, due to the low permeability and low diffusivity of the material. The drying phenomenon is very slow and becomes slower over the time.

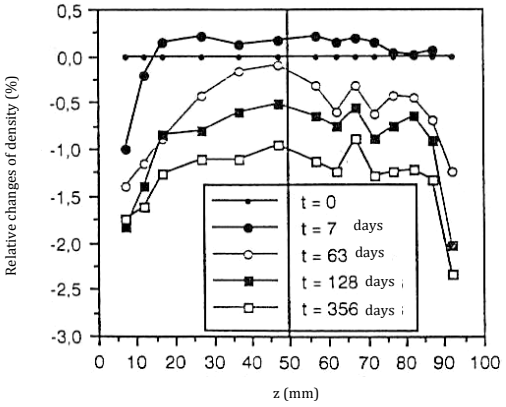

FIGURE 1.6: Evolution of water content of a concrete sample, two opposite surfaces are exposed to a relative humidity of 53.5% at $20^{\circ}C$, [19]

Different transport mechanisms are involved in the drying of hygroscopic cement-based materials. Hygroscopy is the ability of material to attract and hold water molecules from the surrounding environment. This is achieved through either capillary condensation or surface adsorption. These phenomena are responsible for the dimensional variations and drying shrinkage.

In the saturated material, the capillary network is filled with continuous liquid water. When the pores on the surface are drained, a capillary flow is established from inside to the outside of material. Thus, as the capillary phase remains continuous and the permeability is relatively strong, the transfer in the liquid phase due to capillary forces is continue. Therefore, at high relative humidities, the water transfer is governed by capillary pressure.

At intermediate relative humidities, both of the liquid phase and gas phase exist. By decreasing relative humidity, pores are drained and there is no more continue liquid phase in the material. There is diffusional transfer of moisture by evaporation. In such cases, the movement of water into these capillary pores occurs by evaporation-condensation, where meniscus are created.

At low relative humidities transfer in the gas phase is dominant. In addition, a liquid film with the thickness of few molecules is adsorbed on the solid surface. In this case, in addition to the gas diffusion, migration of water molecules called surface diffusion occurs in the porous network. Consequently, the drying is a transitory diffusion phenomenon which is not linear [41]. It should be noted that Mainguy [42] showed that, in the case of drying, the permeation of liquid water can be considered as dominant phenomenon in the normal humidity and temperature conditions.

1.3.1 Drying shrinkage

The macroscopic consequence of drying the cement-based materials is shrinkage. This drying shrinkage depends on the state of internal water. Thus its mechanism is related to the water

and solid connections at considered relative humidity [24, 43, 44]. Three different mechanisms are proposed to explain the drying shrinkage [19]. Shrinkage due to capillary pressure which is related to drying the capillary water, shrinkage due to the variation of surface energy related to the physically adsorbed water and shrinkage due to variation of disjoining pressure which is linked to micropores (CSH pores).

When three phases (solid, liquid water and water vapour) are present, shrinkage by capillary pressure occurs. The humidity difference between the environment and the cement-based material creates a thermodynamic disequilibrium. The pressure of liquid phase decreases following the decrease in the pressure of water vapour in the material (the pressure of gas phase is constant and equal to the atmosphere pressure). Thus a difference between gas and liquid pressure appears which is called capillary pressure and it increases by drying. The contraction in the solid matrix and finally the shrinkage is generated due to the depression in liquid phase. In this model of shrinkage by capillary depression, the material state is assumed close to saturation [19]. However, this mechanism is used to describe the drying shrinkage of the concrete at the range of 100% to 40% relative humidity. In addition, it allows to model the drying shrinkage and its effect on the mechanical behaviour [22, 45, 46].

However, Wittmann explains [44, 47] (using Munich model) that the drying shrinkage at relative humidity range of 100% to 40% is induced due to variation of disjoining pressure. The concept of this model was initially introduced by Powers [48]. The existence of this mechanism has been demonstrated on quartz sheets by Splittgerber test [19]. As shown in Fig. 1.7 a quartz sheet is placed on a support which is also made of quartz glass. Then, the relative humidity of ambient air is gradually increasing. When it reaches 50%, the sheet of quartz moves away from the support, because the repulsive forces overcome the attractive forces which are van der Waals forces. In desorption, when relative humidity decreases below 30%, the gap between the sheet and the support disappears, because the attractive forces become larger again. These experiments also show that there is a hysteresis between sorption and desorption.

At Relative humidities less than 40%, shrinkage is induced due to the variation of surface energy [44, 49]. This surface energy depends on the relative humidity and the adsorbed amount of water. The decrease of relative humidity in the range of 0% to 40%, increases the surface energy and leads to contraction of the porous network. This mechanism is experimentally verified by the test proposed by Wittmann on the cement paste with W/C ratio of 0.45 and 0.6 [49].

Fig. 1.8 illustrates the obtained desorption isotherm for different cement-based materials by Baroghel-Bouny and Godin [50]. Desorption isotherm is the curve representing variation of water content in terms of relative humidity at constant temperature. In this isotherm CO represents cement paste, CH: high performance cement paste, BO: normal concrete and BH: high performance concrete. The obtained curve shows the existence of two distinct phases. When relative humidity is in the range of 100% to 44%, the change depends on the composition of cement-based materials. When relative humidity is less than 44%, water content evolution is similar for all composites. It shows that the hygrometric equilibrium takes place in the CSH pores which is the common phase in all these compositions.

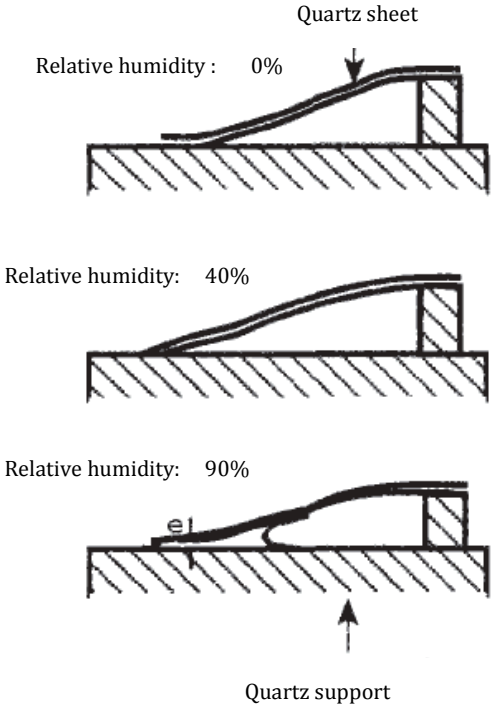

FIGURE 1.7: Splittgerber test [19]

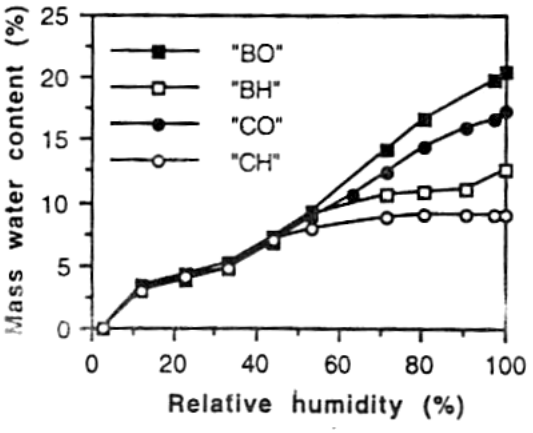

FIGURE 1.8: Obtained desorption isotherm for different cement-based materials [50]

1.4 Overview of experimental studies

In the previous section the structure of cement-based materials, the drying process and its influence on the porous network was generally discussed. Different experimental studies [1, 2, 16–18] were performed to evaluate the behaviour of cement-based materials and effects of various parameters were observed. In this section the studied parameters and experimental conditions of some of these studies are reviewed at first, and then in the following sections, some of their results about the hydro-mechanical behaviour of cement-based materials are synthesized.

Szczesniak [16] performed experimental efforts to illustrate the influence of spherical aggregate

size and cement paste saturation level on drying shrinkage and swelling. In the first part of this study, the material condition during curing was observed. Accordingly, the applied load on the samples were those resulting from internal change of water content and creation of cement paste from mixture constituents and no external mechanical restrain or load were applied. In the next part of this work, the considered material dried in ambient condition and the drying process and shrinkage were studied. This mechanism leads to more sever cracking, however, its initiation is strongly affected by the previous microcracking induced during maturation.

Szczesniak [16] used mono-diameter aggregates in order to reduce the number of analysed factors. The glass and polystyrene spheres were used as aggregate particles. Each series of composite was a mixture of cement paste and spheric aggregates, same as composites proposed by Bisschop and Van Mier [51]. In a first approach, aggregate particles with the same diameter were placed in a composite. This type of composite is not commonly used in practical engineering. To study different parameters, four types of material were tested; cement paste (with two W/C ratio of 0.8 and 0.5), mortar with natural aggregates (dried and saturated aggregates), mortar with rigid glass spheres (with two aggregates volume fraction of 35% and 59% ; and glass aggregates with different diameters 1, 2, 4, 6 mm), and the mortar with soft polystyrene spheres (with two aggregate diameters 2, 3 mm).

Rougelot [1] focuses on multi-scale couplings under hydro-mechanical and chemical stresses due to drying and leaching. Firstly, the studied material was dried by imposing different relative humidity levels in order to obtain desorption isotherm. And in the continue, the second solicitation was related to leaching of the material. These two solicitations cover behaviour of material at short, medium (drying) and long term (leaching). The influence of cracking on drying, leaching and hydro-mechanical couplings were studied. The experiences were applied on two types of material: cement paste and mortar; with two W/C ratio of 0.8 and 0.5. The siliceous aggregates were used in mortar. Obtaining equilibrium state at each relative humidity level, regarding the low permeability and diffusivity of materials is relatively long. Thus, tests were applied on the samples with smallest possible dimension, $20 \times 20 \times 160$ mm prismatic samples. For each test 3 samples were studied. Test samples were protected against premature drying by a plastic and left at room temperature for one day before being demolded. Hydration reaction in cement-based materials is very slow and it could continue for several months. The demoled samples were preserved in a lime saturated environment at 20°C , during at least four months. The samples mass increased regularly during maturation. After 130 days, their mass was stable, indicating that the hydration process could be negligible. This point was considered as the saturated state for samples which were the reference point in the applied tests.

Yurtdas [17] investigated short and long term of mechanical behaviour due to drying. The influence of drying on the material is a kind of catalyst for the development of chemical degradation (ions attacks, aggressive liquids and gas) by the creation and growth of microcracks. Although the influence of desiccation on the mechanical behaviour in long term has been known, few studies were engaged on the evolution of the mechanical behaviour in the short term according to desiccation. A part of this thesis was intended to identify these effects. The experiments were performed on two types of mortar sample (cylindrical and prismatic) with two W/C ratio 0.5 and 0.8. The curing period was 1 month and all measurements were started from a saturated

(or almost saturated) state to a dry (or almost dry) state, in order to fully characterize the behaviour as a function of water content.

Brue [18] studied high performance concrete with different types of cement and W/C ratio. The temperature and relative humidity were other studied parameters. The first set of concrete samples were made using CEM I and CEM V. Obtained shrinkage in CEM I samples were less than CEM V samples. This is attributed to the nature of cement that is the main difference in their compositions and which induces more porosity for CEM V. In the following of this study, concrete samples were desaturated to reach the dry state and then they were resaturated. The full cycle of drying and saturation is very long, thus some samples were dried in oven and the re-saturation was performed, in order to obtain results faster. These two protocols evaluated the material behaviour due to drying and re-saturation. In order to investigate the temperature effect on porous network, sorption-desorption isotherm for three different temperatures (20°C, 50°C and 80°C) were obtained.

In the following, performed tests to assess influence of different parameters, will be explained and the obtained results will be discussed.

1.4.1 Sorption-desorption isotherm

In the study of Rougelot [1], the prepared samples were kept in water saturated with lime during maturation and after reaching the saturated state, they were taken out and were imposed to different relative humidity levels in order to study the material behaviour due to drying and saturation. The temperature was fixed at 20°C. Relative humidity was controlled using a climatic chamber. Specific relative humidities as 3%(salt: silica gel) and 100% (pure water) could be obtained at 20°C using saturated salt solutions. Mass of samples were regularly measured until reaching stable mass. When mass variation during 7 days was less than 0.1%, that was considered as a stable mass. It was supposed that there was no more water transfer within the material. Samples mass after drying in the oven at 90°C represent the dried state. In order to investigate temperature effect on the sorption-desorption isotherm, relative humidity variations were applied at 50°C and 80°C.

Fig. 1.9 and Fig. 1.10 show obtained desorption isotherm by Rougelot [1] for cement paste and mortar with different W/C. In a given W/C, mortars and cement pastes have a qualitatively similar form of isotherm. This result tends to prove that in these materials, the presence or absence of aggregate does not significantly modify the hydraulic behaviour. It can be explained by the fact that the used aggregates were siliceous aggregates with very low porosity, therefore they were not sensitive to relative humidity changes.

For mortars or cement paste, when W/C ratio increases during desorption water content decreases faster. Because by increasing W/C ratio, the porosity also increases. However, a reversal trend occurs at high relative humidities.

Fig. 1.11 shows the temperature effect on desorption isotherm. when temperature increases, desaturation leads to very low saturation levels, while relative humidity is still high. These

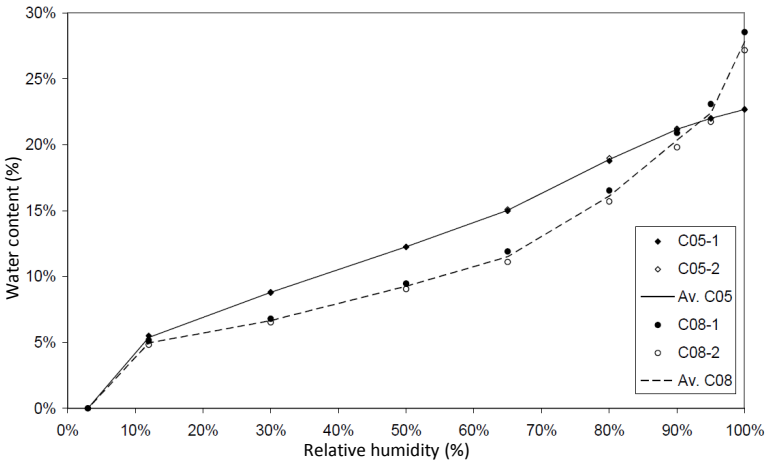

FIGURE 1.9: Desorption isotherm of cement paste [1]

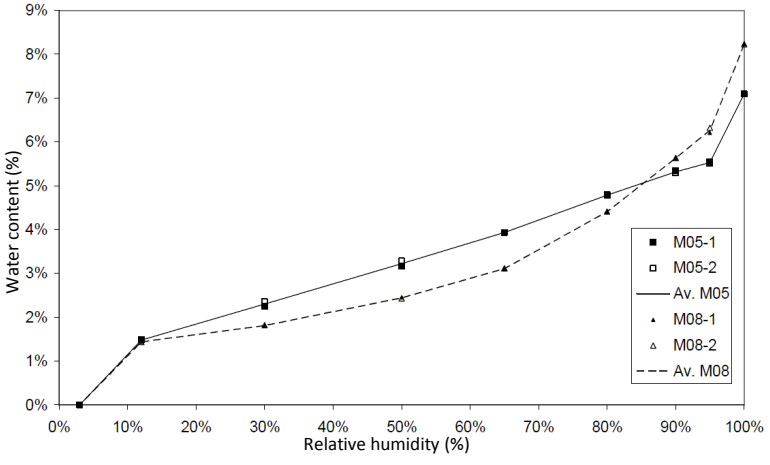

FIGURE 1.10: Desorption isotherm of mortar [1]

differences between 20°C and 50°C, compared to 80°C, indicate that the amplification of the drying mechanisms with temperature would lead to the drying of CSH pores.

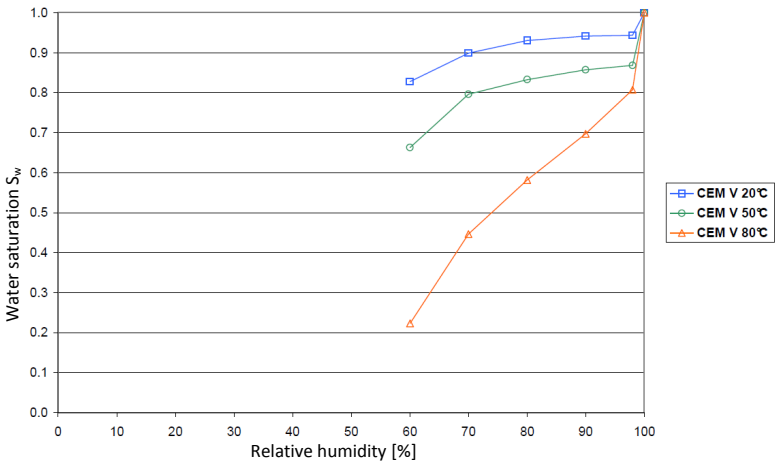

FIGURE 1.11: Temperature effect on desorption isotherm of concrete [18]

1.4.2 Pore distribution

Pore distribution can be obtained by applying mercury intrusion test. The used samples in this test were cylindrical ones (diameter 36 mm, thickness 10 mm) which were sampled from blocks of $100 \times 100 \times 100$ mm. The saturated samples were dried at 60°C until reaching constant weight. This temperature was chosen for two reasons: It avoids large water gradients in the material during drying, that reduces cracks induced by drying. The other reason is the fact that the mercury could not have accessed to all sizes of pores, including fine pores, and drying at 60°C leads to drain pores which are accessible to mercury. The sample was placed under a vacuum of $50 \mu m Hg$ for 5 minutes, and then it was filled under low pressure (3kPa), the pressure was increased progressively with a duration of 20 seconds, in each pressure the equilibrium should be reached. The volume of injected mercury in each pressure level was registered to obtain pore distribution. Finally, the mercury was extracted by reducing pressure.

Pore distribution of porous materials can also be obtained using desorption isotherm. In the study of Rougelot [1], pore distribution of cement paste and mortar were obtained using water vapour desorption isotherm and it was compared to the mercury intrusion results in Fig. 1.12.

The obtained porosity by mercury intrusion test is always less than obtained porosity by water vapour desorption test. Because the mercury could not penetrate to fine pores which were drained at $90°C$. Thus in mercury intrusion test even in maximum pressure ($200 MPa$) the porous network is not fully saturated by mercury. Desorption porosimetry provides a good estimation of narrow pores (below $10nm$). Conversely, the mercury porosimetry is best suited to study pores with diameter greater than $50nm$. It is also illustrated in the curve that fine pores

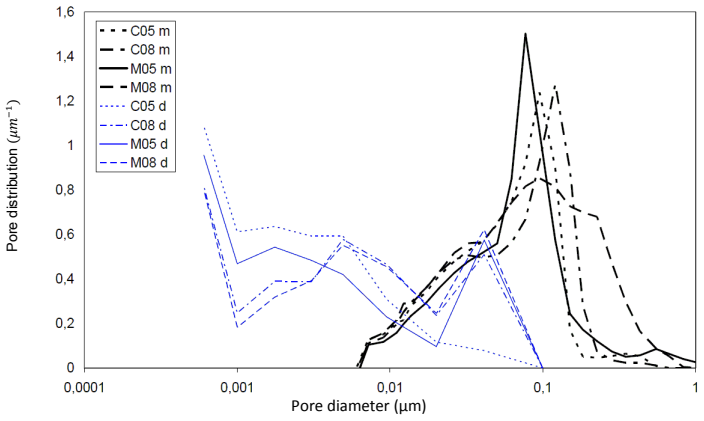

FIGURE 1.12: Pore distribution ('m' for mercury intrusion, 'd' for water vapour desorption, 'C' for cement paste, 'M' for mortar, '05' for $W/C = 0.5$, and '08' for $W/C = 0.8$ [1]

were not estimated by mercury intrusion test but their distribution was measured by water vapour porosimetry.

Rougelot [1] observed that the presence of aggregates and W/C ratio does not have any influence on pore distribution for pores with the size of 1 to 3 nm. Pores with diameter between 3 and 12 nm are sensitive to the W/C, but not in the presence of aggregates. Pores with diameter between 60 and 100 nm are determined by intrusion of mercury. These type of pores are sensitive to the W/C ratio, as well as the presence of aggregates.

Despite the long duration of test, using desorption isotherm to obtain pore distribution gives a more appropriate result for the study of the microstructure of cement-based materials. In the mercury intrusion technique, drying sample at $60°C$ before mercury injection, reproduces cracks in the structure of porous network and it is the most significant shortcoming of this test.

1.4.3 Drying shrinkage

The experimental tests could be performed on samples in order to evaluate their dimensional variations due to drying. During curing time, samples mass increased and in most cases, the height of samples also increased which is called swelling. In the second stage, samples were placed in a climatic chamber and relative humidity changed progressively. During this stage mass and hight of samples were regularly measured in order to determine water saturation degree and shrinkage. In different references [1, 16, 18] the influence of aggregate size, W/C ratio and temperature on dimensional variations was assessed.

Three intervals were observed during drying process:

- 0% to 10% mass loss: No significant height change
- 10% to 65% mass loss: Proportionality between shrinkage and mass loss
- 65% to 100% mass loss: No significant height change

Fig. 1.13 based on the study of Szczesniak [16] illustrates that drying shrinkage strongly depends on aggregate diameter. The smaller the aggregate are, the bigger the shrinkage becomes. But the total deformation is not go to infinity with decreasing aggregate diameter. Because at a certain point, aggregate diameter (aggregate till now being the biggest particle inside the composite) is the non-hydrated cement grains.

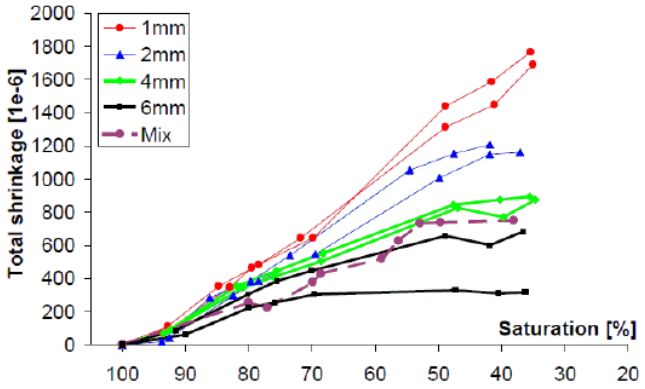

FIGURE 1.13: Influence of aggregate diameter on drying shrinkage [16]

Drying shrinkage induces cracking in the sample. Bisschop et al. [51] show that the cracking also depends on the size of aggregate. It was noted that for 1mm balls, microcracks remain superficial and mainly due to the effect of the structure. When the diameter of balls increases, for example for the composites with 6mm balls, these microcracks extend in the mass of the sample to propagate in all of the sample. The biggest and widest cracks were observed for composites with bigger aggregates. It was observed that when the size of the aggregate increases, there are more important cracking and they are oriented in all directions. In the case of small aggregates, this cracking was observed in the direction of the hydric gradient and remained on sample surface.

Rougelot [1] also studied the influence of W/C ratio on porosity and isotherm. By increasing W/C ratio, the porosity of material and following to that the drying shrinkage increases. Fig. 1.14 shows the porosity in terms of W/C ratio for mortar. By comparing the obtained results for mortar and cement paste in Fig. 1.15, it was observed that in a certain W/C , drying shrinkage in mortar is less than cement paste. The three phases of drying process were also observed in this study and in addition, these three phases were better observed in mortar compared with the cement paste.

Fig. 1.16 shows the variation of drying shrinkage according to W/C ratio and the volume fraction of aggregate used in the material. For the same aggregate proportion, shrinkage increases by increasing W/C ratio. The kinetics and the amplitude of shrinkage are more important by reducing aggregate contents. For the same W/C ratio, when volume fraction of aggregate reduces, the shrinkage increases with a more important amplitude.

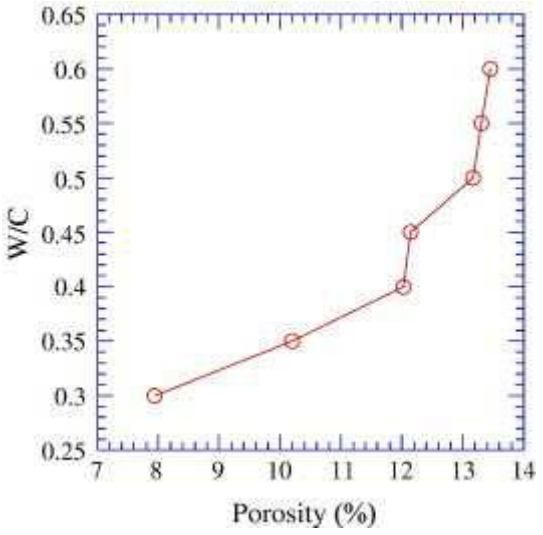

FIGURE 1.14: Influence of W/C ratio on the porosity of mortar [52]

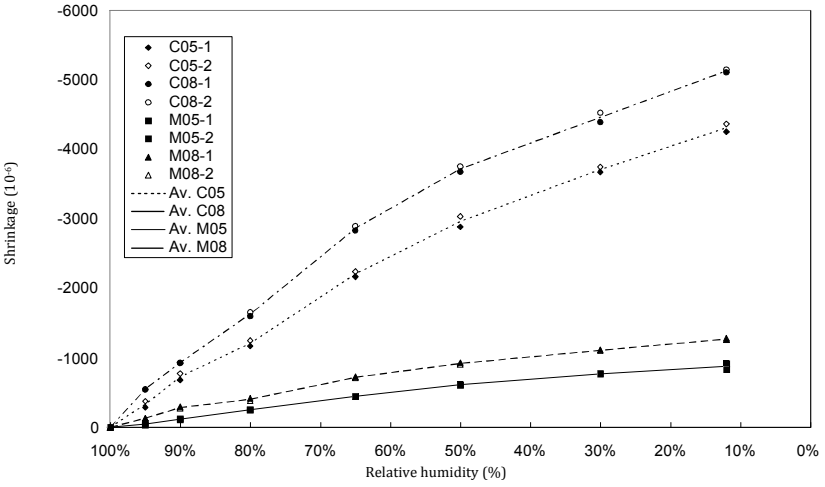

FIGURE 1.15: Shrinkage in terms of relative humidity ('C' for cement paste, 'M' for mortar, '05' for $W/C = 0.5$ and '08' for $W/C = 0.8$ [1]

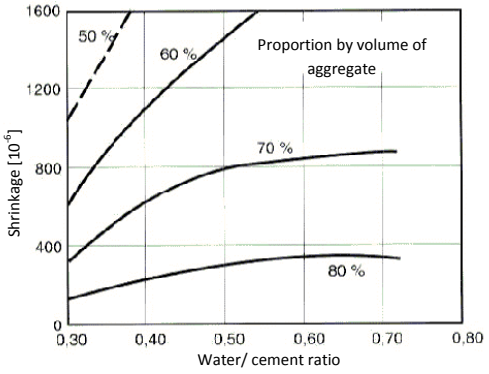

FIGURE 1.16: Influence of W/C and aggregate volume fraction on shrinkage at $RH = 50\%$ and $T = 21°C$ for 6 months [53]

Brue [18] performed tests at three different temperatures (20°C, 50°C and 80°C). Fig. 1.17 shows the drying shrinkage in terms of relative humidity for the concrete made of CEM V. It was observed that the form of curves are similar at different temperatures, however, the amplitude depends on the temperature. The drying shrinkage at $RH = 60\%$ and at 50°C is 1.6 times higher than the shrinkage at 20°C. At 80°C, the shrinkage is approximately 2.6 times greater than those at 20°C. These values confirm the major influence of the temperature on the dimensional variations associated with the drying process.

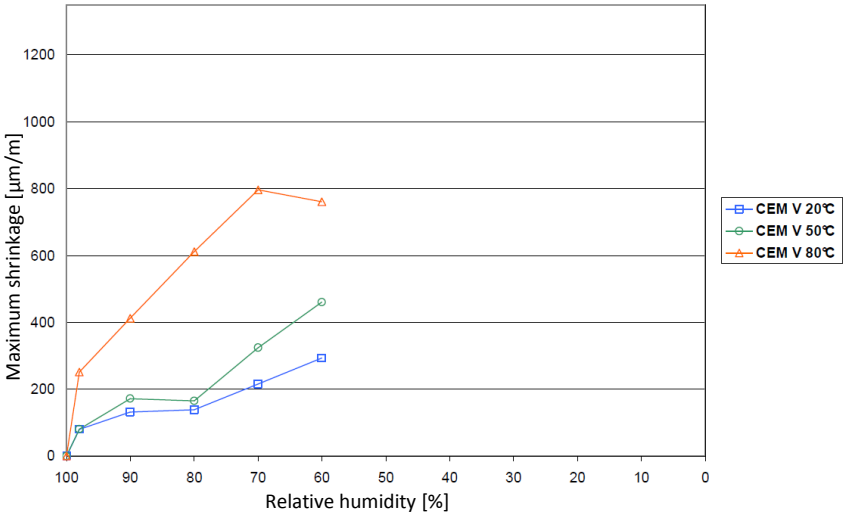

FIGURE 1.17: Influence of temperature on shrinkage for concrete with cement type CEM V [18]

1.5 Conclusions

The structure of cement-based materials regarding its hydric behaviour was reviewed in this chapter and it could be conclude that:

- These materials contain a complicated porous network.
- The structure of porous network depends on the formulation of material (water cement ratio, ...) and the environmental conditions these materials are facing (relative humidity, temperature and ...)
- The microstructure of material changes over time. These modifications begin at first because of the hydration process and curing which continue in long term.
- **It is supposed that a large part of the complexity of hydro-mechanical behaviour at macroscale comes from the complexity of porous network.**

- In order to recognize the structure of porous network, the perfect solution is to obtain their exact morphology using experimental techniques.
- However, regarding the shortcomings in the observation methods, for the moment it is not possible to have a realistic image of nanoporous network in 3D.
- Therefore, they should be simulated using different numerical models. The first method is the hydration model [14] which is based on the formulation and conservation conditions of materials. This model is not already validated, thus, another method which is the morphological modelling being employed in this thesis.

Chapter 2

Morphological modelling of heterogeneous materials

Contents

2.1 Introduction

Predicting the hydro-mechanical behaviour of a porous media necessitates two steps. The first step is to construct a realistic porous media model on the way to build up its morphology. The second step consists of imposing the governing equations of a given phenomenon on this particular model. In order to simulate the hydro-mechanical behaviour of cement-based materials from the first step, a numerical model must be proposed to represent the porous network. In various models developed for cement-based materials in the literature [54, 55], pores are often considered as a particular shape, for example in the model developed by Ranaivomanana et al [11], they consider cylindrical pores with a calibration parameter. This parameter can also be interpreted as the radius which pores feature a more oblong form than cylindrical shape. By decreasing this parameter, pores become progressively flattened. This type of pore model is shown in Fig. 2.1 [54].

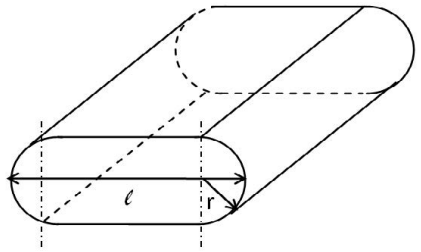

FIGURE 2.1: Oblong geometry fine pores [54]

In the study of Rougelot [1], for modelling sorption-desorption isotherm, pores are also considered as cylindrical elements.

In some other approaches, pores are considered as spherical elements. For example Varloteaux et al [55] simplified void spaces of the porous media as a network of connected nodes. Nodes represent pore bodies which are connected together by cylindrical channels with a circular, triangular or quadratic cross section. A representation of this model is illustrated in Fig. 2.2. This distinction between pore-bodies and pore-connections and their simplified geometry makes complex problems easier to solve through the use of analytical solutions.

In all of the above presented models, physical parameters such as porosity must be computable. For example in the model of Varloteaux [55], the porosity is calculated from the volume of pore-bodies and pore-connections. In this cubic structure, the choice of a suitable size distribution of pore channel is a key parameter to the construction of a representative porous media.

As mentioned above, modelling of porous network in most studies [1, 8, 11, 55, 56] is a conceptual representation of a porous medium without describing the exact morphology of the medium. Consequently simulations based on these models could not give a realistic explanation of heterogeneous materials behaviour.

In order to have a more realistic geometry of the porous network, another porous network modelling is being recently developed. In this method synchrotron computed microtomography is

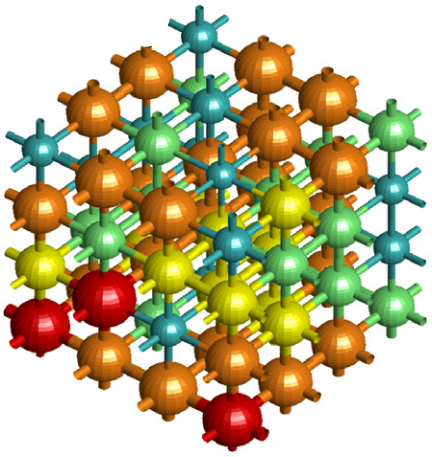

FIGURE 2.2: A simplified porous network model [55]

used to generate 3D data sets at micrometer scale [57–60]. Despite the advantages of this method to reproduce a realistic model of porous networks, using synchrotron computed microtomography is an expensive and time consuming procedure. Another shortcoming of this technique is its accuracy to model small pores. It is not able to model nanopores of the porous network. Therefore this study attempts to propose a more practical method, which gives a numerical model of nanoporous network knowing only few physical parameters.

This study also pursuits to propose a pore network modelling without considering any particular pore shapes, and could therefore gives an accurate general representation of the nanoporous network. In this approach pores are modelled using the definition of Random Fields excursion. Before describing the functionality of this model, the principle of Random Fields should be explained along with some examples of models based on excursion of Random Fields.

In this study five different types of nanoporous materials are modelled and analysed in both 2D and 3D . Nanoporous network with one class of pores (hereafter called MAT1), nanoporous network representing the union of two classes of pores (hereafter called MAT2), nanoporous network representing the union of five classes of pores (hereafter called MAT3) and nanoporous network with pore distribution similar to cement paste consists of 7 classes of pores (hereafter called MAT4) are generated in 2D. In 3D, nanoporous network with pore distribution similar to cement paste with two different W/C ratio 0.8 (hereafter called MAT5) and 0.5 (hereafter called MAT6) are also treated. It should be noted that for 2D networks the grid size is 5000^2 and for 3D it is 800^3.

2.2 Models based on excursion of Random Fields

Considering different scales, cement-based materials such as concrete, mortar or cement paste are heterogeneous media. To study their behaviour, the first step is to model the morphology of these materials. Nowadays, CMT (Synchrotron Computed Micro-tomography) is used to measure the real geometrical structure of porous media [61] at micrometer scale. However, the

reconstruction of nanoporous media which necessitates generation of realistic media is still an issue. In this study, a random aspect using Random Fields is applied to model a representative nanoporous media. In the following this technique is reviewed.

2.2.1 Random Fields

The most common representation of heterogeneities in literature [8, 56] is often performed using objects with simple geometrical definitions such as spheres [62], ellipsoids [63] or cylinders [11]. These methods are so much simplified that they can hardly represent the porous network. Moreover, the amount of information necessary to describe these morphologies can become important when a large number of objects are considered. In the model with spheric objects $4N$ and for model with ellipsoid objects $7N$ information is required, where N is the number of objects in network. For these reasons, it is better to turn to morphological models with a random aspect such as excursion sets [13]. In this method, initial morphologies are generated with random shapes which gives a better representation of porous networks. In addition, only four parameters (mean, variance, correlation length, threshold) are required in order to generate a morphological model of porous network.

The use of correlated Random Fields gives a considerable improvement to morphological modelling. Indeed, in addition to the usual characteristics of random variables such as mean or variance, the correlated aspect leads to a spatial structure for the fields. It means that, in the generated models using correlated Random Fields, there is a continuous spatial distribution of properties such as means, variance and etc.

This section covers both theoretical and numerical basis of correlated Random Fields. Then, mathematical tools to characterize excursion sets expressed in literature [12] will be presented.

2.2.1.1 Gaussian correlated Random Fields

A Random Field is defined as a random function $f(x)$ over a space M that takes values in $\mathbb{R}$ [64]. As mentioned before, a Random Field is generated by knowing at least two parameters, means and variance. The most popular type of variables distribution is Gaussian, and the presented framework is based on this distribution. However, it is applied in a more general case, using a wilder range of distribution known as Gaussian related [13].

The spatial structure for the random field is obtained using correlated aspect which can statistically be controlled through the definition of a covariance function [13]. It means that for any couple $(x, y) \in M^2, g(x)$ and $g(y)$ are not two independent variables. They are correlated. The measure of this correlation is made through the covariance function $\mathcal{C}$ and can be defined for a zero mean distribution by equation (2.1):

$$\mathcal{C}(x, y) = \mathbb{E}\{g(x)g(y)\} \tag{2.1}$$

In this study the covariance functions are not detailed. But it should be mentioned that for a Random Field with certain parameters, different results could be obtained considering different covariance functions such as Gaussian, Cauchy, Exponential, Spherical and etc.. However, Gaussian is one of the most commonly used covariance functions which is also used here to generate correlated Random Field. It is defined by two parameters when the mean value is considered as zero (equation (2.2)).

$$\mathcal{C}(x) = \sigma^2 exp(-\frac{x^2}{L_c^2}) \tag{2.2}$$

Variance σ^2 characterizes the distribution and the other one called correlation length L_c assigns a certain characteristic length-scale. The role of the correlation length on the generated results will be displayed later in this chapter.

In the presented framework f will always be taken as a Gaussian Random Field and the random variables are related to Gaussian covariance function. The value of mean is considered as zero and $\sigma^2 = 1$ could be an appropriate choice. Fig. 2.3 shows a representation of Gaussian Random Field over a three-dimensional space ($M \subset \mathbb{R}^3$) which is generated using the program 'R'.

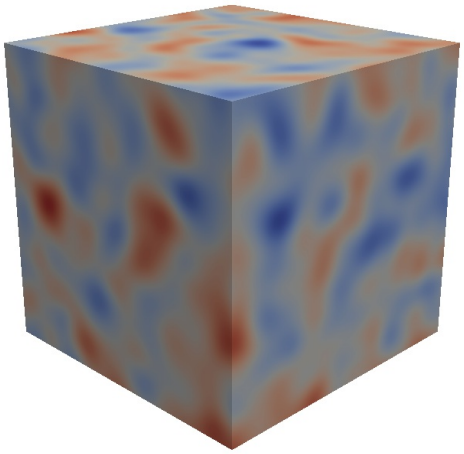

FIGURE 2.3: Realisation of a correlated Random Field

2.2.2 Excursion set

The desired model representing cement-based materials usually includes two components, pores and matrix. While Gaussian correlated Random Field gives a set of random variables defined in certain domain, an operation must be applied on Random Field to transform it to a binary model corresponding to heterogeneous materials. This transformation operation is called thresholding.

An excursion set is a subset of correlated Random Field defined by thresholding. This operation creates randomly shaped morphologies which are the transformation of a continuous field to a

binary one. Lets $f(x)$ be a realisation of Random Field defined as above and $D \subset \mathbb{R}$ a given hitting set. The excursion set $\mathbf{A_D}$ is defined by the subset of M where f takes its values in D, $\mathbf{A_D}$ is also defined by equation (2.3).

$$\mathbf{A_D} \triangleq \{x \in M | f(x) \in D\} \tag{2.3}$$

An example of this principle is illustrated in Fig. 2.4 for a one dimensional case, where u is the threshold value, and the hitting set is the open subset of $\mathbb{R}$, $D = [u, +\infty[$. Examples of three dimensional excursions are given in Fig. 2.5 for two different thresholds.

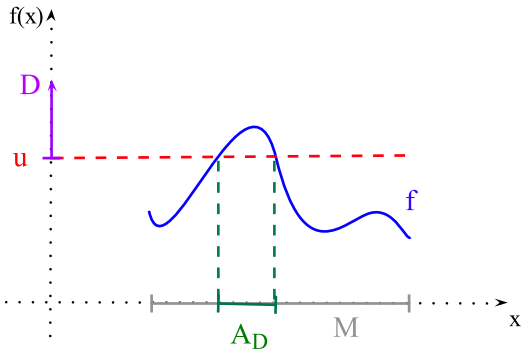

FIGURE 2.4: Schematic representation of a one-dimensional excursion

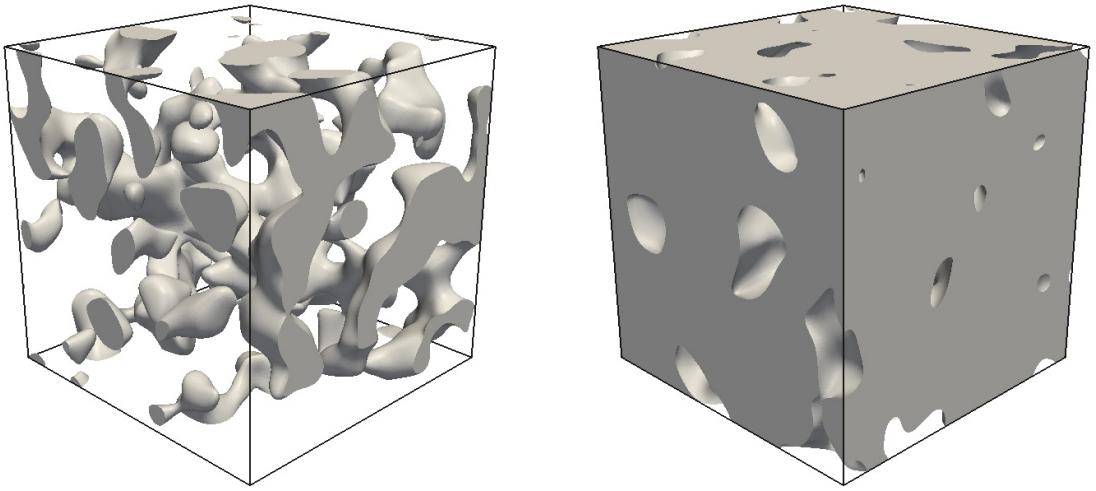

FIGURE 2.5: Two excursion sets of the same realisation with different thresholds

As mentioned in section 2.2.1.1 covariance function has an important influence on the generated Random Field and accordingly excursion set. In Fig. 2.6 Gaussian Random Fields were generated in a domain of $1\mu m$ considering zero for mean, $L_c = 0.2\mu m$, $\sigma^2 = 1$. However, different covariance functions were considered in order to illustrate their effects. Then excursion sets were obtained considering $u = 0.5$, and a noticeable diversity was observed in different cases, which comes from the influence of the covariance function.

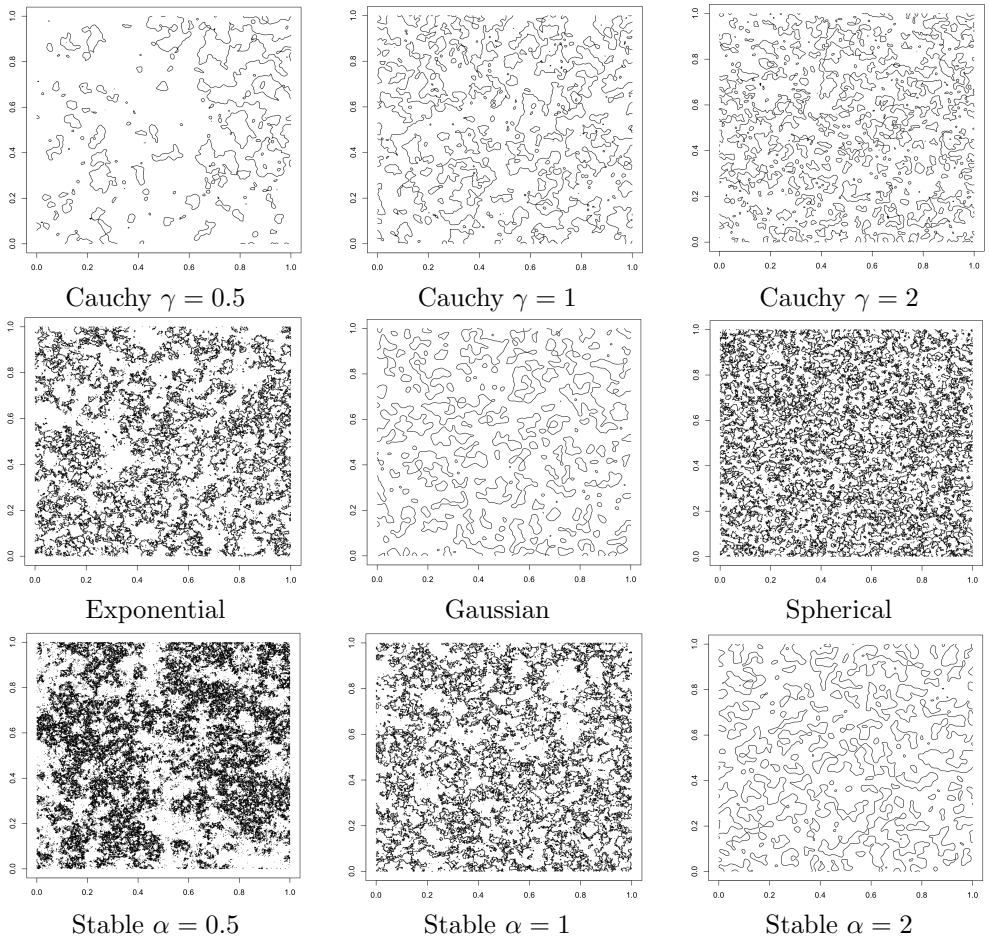

FIGURE 2.6: Level sets correspond to $u = 0.5$ considering different covariance functions

2.2.2.1 The role of correlation length

As previously expressed, different parameters should be determined to define the Random Fields, such as means, variance and correlated length. In the following, Gaussian Random Field is considered with zero mean and $\sigma^2 = 1$. But the value of correlated length could be determined according to the desired pore distribution. In the application of Gaussian Random Fields to model a porous media, this parameter could represent the average size of pores in the network.

Fig. 2.7 illustrates the role of the correlation length on the Random Field structure, where Fig. 2.7a shows the distribution with large L_c and Fig. 2.7b with small L_c. Both of these porous media have the same porosity, but the pores are differently distributed. In Fig. 2.7a large L_c reproduces great pores whereas the small L_c in Fig. 2.7b represents the same porosity generating small pores.

2.2.2.2 Determination of input data using experimental values

As described in previous sections, to generate a morphological model representing cement-based materials, the first step is to define a Random Field. Hence, the value of mean, variance and correlation length should be determined. In the next step, the thresholding is applied to

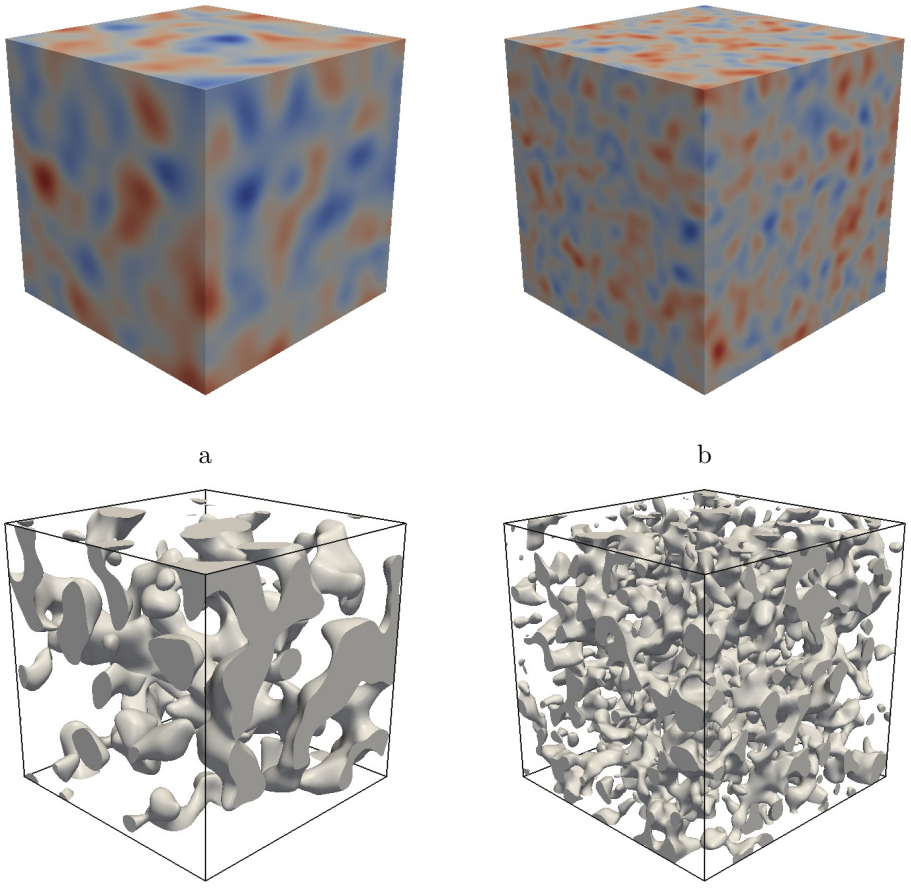

FIGURE 2.7: Impact of L_c on Gaussian Random Field (a: Large L_c , b: Small L_c)

Random Field and a binary model (excursion set) is obtained. In this step the choice of threshold value and hitting set have significant effects on the obtained morphology.

As shown in Fig. 2.5, threshold value has an important influence on the resulting morphology. Low values lead to high volume fraction excursion set. This model could be a proper representation of porous network. On the other side, high values lead to a morphology where just several disconnected components are introduced. The latter excursion has a low volume fraction and could represent pores in a porous network or aggregates in concrete.

The Random Field parameters (mean, variance, correlation length) could be linked, on one hand, with threshold value and on the other hand, with the geometric characteristics of the desired model such as volume, surface and Euler characteristic.

Hence, it is very important to determine these characteristics in a primitive step. The geometric characteristics like surface and volume could be derived from experimental studies. For example the volume of pores could be obtained from mercury intrusion test and the surface of pores could be detected in BET experience.

On the other side, concerning Random Field parameters, the value of mean and variance were determined former, considering Gaussian correlated Random Field and the correlation length

which represent the pore size distribution of the porous network could be derived from mercury intrusion result.

The relation between Random Field parameters, threshold value and the geometric characteristics of network shows that the resulting morphology could be influenced by several items during the thresholding process. Modifying these parameters gives a wide range of morphologies (Fig. 2.8). In this figure looking at horizontal axis, correlation length decreases left to right and looking at vertical axis, the influence of threshold value is illustrated.

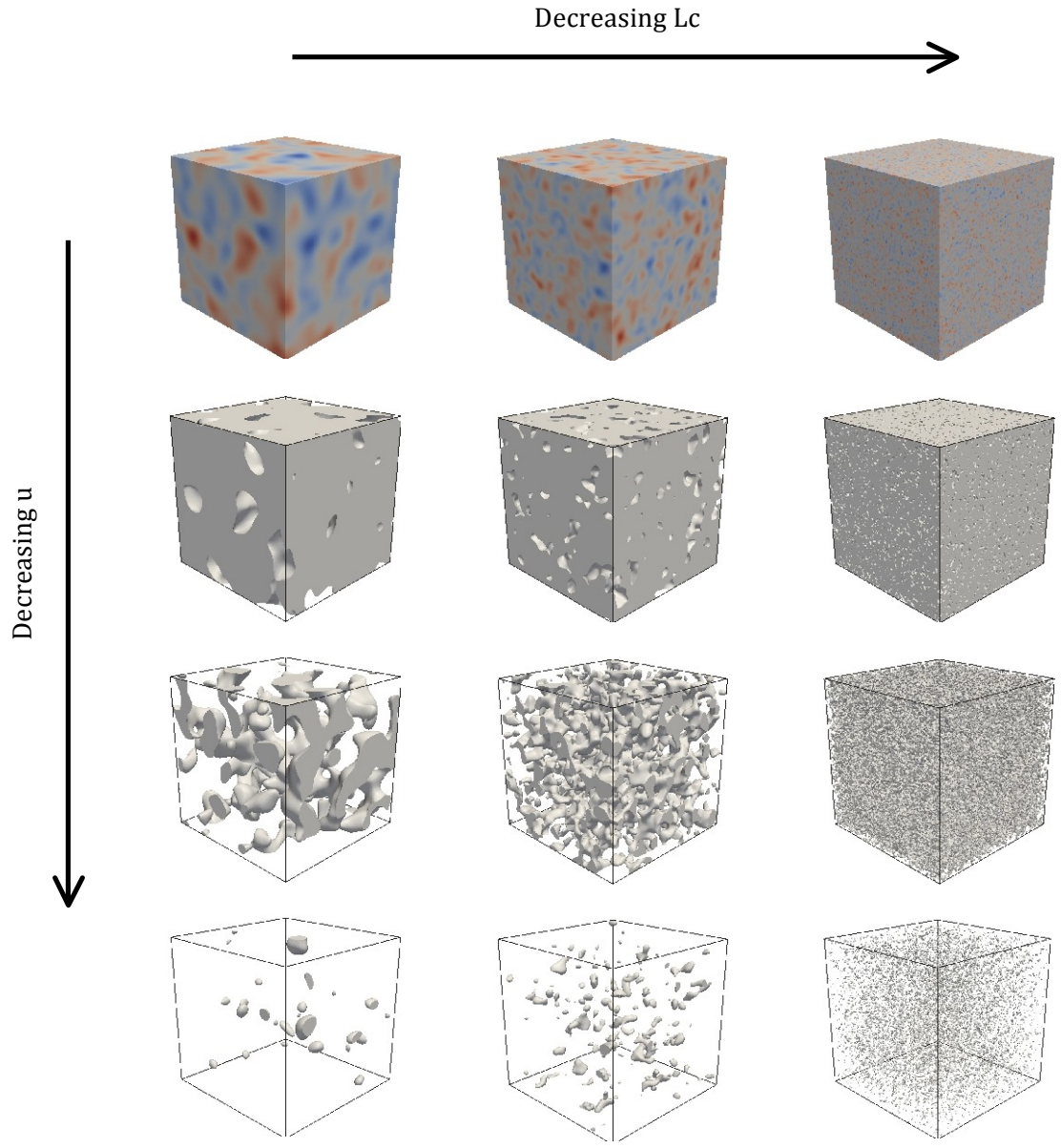

FIGURE 2.8: Wide range of morphologies considering different parameters (L_c decreases left to right, u decreases up to down)

The characteristic values of morphology and their properties need to be considered to classify these morphologies. They are studied in two categories of geometrical and topological properties. They are detailed in the next section.

2.2.3 Characteristic values of morphology

In the previous section it has been expressed that for a particular threshold value and certain Random Field parameters it is possible to have several morphologies. In order to provide a global description of a morphology and its classification, morphological properties and characteristic values have to be studied. Thus, they are defined in two categories of geometrical and topological properties.

The mathematical framework in the work of Adler [64] provides geometrical and topological measures of excursion sets, wherein a powerful and accurate morphological tool is represented. Since the excursion sets have been defined, it is usually required to have some information about their properties, such as how many components they have, what is the size of components, how long is their boundaries and etc. It has been proved that in a N-dimensional space, N + 1 descriptors are enough to fully describe it. There are different definitions of these characteristics in literature [12], in this study the Lipschitz-Killing curvatures [65] (here after LKCs) are chosen. In our three dimensional case, four LKCs are denoted by $\mathcal{L}_j$, $j = 0, ..., 3$, providing both geometrical ($\mathcal{L}_1, \mathcal{L}_2, \mathcal{L}_3$) and topological ($\mathcal{L}_0$) descriptions of the excursion set $\mathbf{A_D}$ [12]. In the following, the properties are described under the title of geometrical and topological properties.

2.2.3.1 Geometrical properties

Geometrical properties such as volume and surface, investigate the geometry of the model based on excursion set of Random Field. In order to have a more accurate determination, they could be defined by:

- $\mathcal{L}_3(\mathbf{A_D})$ is the volume of $\mathbf{A_D}$
- $\mathcal{L}_2(\mathbf{A_D})$ is half the surface area of $\mathbf{A_D}$
- $\mathcal{L}_1(\mathbf{A_D})$ is twice the calliper diameter of $\mathbf{A_D}$

The calliper diameter is defined for two parallel planes and it obtains by averaging the distance between planes for all rotations of $\mathbf{A_D}$.

2.2.3.2 Topological properties

Contrary to other LKCs, Euler characteristic represent the topological properties. In three dimensions, it is defined by :

$$\mathcal{L}_0(\mathbf{A_D}) = \#\{connected\ components\} - \#\{handles\} + \#\{holes\} \tag{2.4}$$

For example, a sphere, a cube or a cone have an Euler characteristic of 1. Two full sphere or a hallow sphere, both have an Euler characteristic of 2. In the case of two solid spheres, there are two connected components and in the case of a hallow sphere, there are a connected component

TABLE 2.1: LKCs for a cube of dimension a and a sphere of radius r

LKC	Meaning	Value for a cube	Value for a sphere
$\mathcal{L}_0$	Euler characteristic	1	1
$\mathcal{L}_1$	Twice the calliper diameter	$3a$	$4r$
$\mathcal{L}_2$	Half the surface area	$3a^2$	$2\pi r^2$
$\mathcal{L}_3$	Volume	a^3	$\frac{4}{3}\pi r^3$

and a hole. Examples are showing that Euler characteristic is only based on topological aspects, it could be the same without any geometrical similarity.

Table 2.1 summarizes all LKCs and their values for a cube of dimension a and for a sphere of radius r.

Following the work of Adler [12], a probabilistic link has been made between excursion set properties and Random Field thresholding parameters. It gives an explicit equation for expectations of the LKCs. It is not the purpose of this work to give full details on these equations, however, full proof and details can be found in literature [12, 66]. Considering a Gaussian Random Field whose components have a zero mean and are isotropic with variance σ^2, general equations can be simplified and four equations corresponding to four LKCs can be written in terms of L_c, u and σ^2. Where L_c is the correlation length of the Random Field and u is the threshold value.

These equations are developed here for Gaussian Random Fields generated considering Gaussian covariance in a cube of dimension T. Therefore we have the needed functions of threshold for the volume, surface area, the mean diameter and Euler characteristic.

$$E\{\mathcal{L}_0(\mathbf{A_D})\} = [\frac{\sqrt{2}}{2\pi^2}\frac{T^3}{L_c^3}(\frac{u^2}{\sigma^2}-1) + \frac{3\sqrt{2}}{2\pi^{3/2}}\frac{T^2}{L_c^2}\frac{u}{\sigma} + \frac{3\sqrt{2}}{2\pi}\frac{T}{L_c}]e^{-\frac{u^2}{2\sigma^2}} + \psi(\frac{u}{\sigma}) \tag{2.5}$$

$$E\{\mathcal{L}_1(\mathbf{A_D})\} = [\frac{\sqrt{2}}{\pi^{3/2}}\frac{T^3}{L_c^2}\frac{u}{\sigma} + \frac{3\sqrt{2}}{4}\frac{T^2}{L_c}]e^{-\frac{u^2}{2\sigma^2}} + 3T\psi(\frac{u}{\sigma}) \tag{2.6}$$

$$E\{\mathcal{L}_2(\mathbf{A_D})\} = \frac{\sqrt{2}}{\pi}\frac{T^3}{L_c}e^{-\frac{u^2}{2\sigma^2}} + 3T^2\psi(\frac{u}{\sigma}) \tag{2.7}$$

$$E\{\mathcal{L}_3(\mathbf{A_D})\} = T^3\psi(\frac{u}{\sigma}) \tag{2.8}$$

Consequently, as the first application, there is an occasion to represent the porous media by knowing its pore volume fraction and specific surface, afterwards the values of L_c and u are derived using above equations and the correlated Random Fields excursion sets are introduced.

2.2.4 Simulation of Random Fields using 'R'

R is a programming language and software environment for statistical computing. R and its libraries implement a wide variety of statistical techniques, including linear and non-linear modelling. Many of standard functions are written in R, which makes it easy for users to apply them. Random Fields package offers various tools to simulate different kinds of Random Fields like multivariate, spatial, spatio-temporal Gaussian Random Fields [67] and etc. Several methods

for the simulation of Random Fields in R^d exist such as Turning bands, FFT, Karhunen-loève and etc. [68].

In this study R is used to generate the Random Field in a cubic domain considering characteristic values obtained from experimental results. The used script is presented in appendix A.

2.2.5 Representing the grain size distribution

In the previous section, the method to generate numerical porous network model was explained but this numerical model should be compared with a real porous medium to confirm their similarity. One of the means to do this comparison is through the verification of the pore distributions between them. Generally in order to produce a numerical model which is sufficiently similar to the experimental one, union of several Random Fields with different L_c must be used. As mentioned before L_c represent the pore size distribution. When a morphological model is introduced considering only one correlation length, pores are distributed in small interval around the value of L_c. In this study, a 2D porous network which is called MAT1 was generated considering one correlation length $L_c = 0.003\mu m$ in a domain of $1\mu m$ and the porosity of 56%. Fig. 2.9 shows the porous network. Fig. 2.10 illustrates the pore distribution and confirms that pores are distributed in a small interval around L_c. The hydric behaviour of this porous network will be studied in the following chapters.

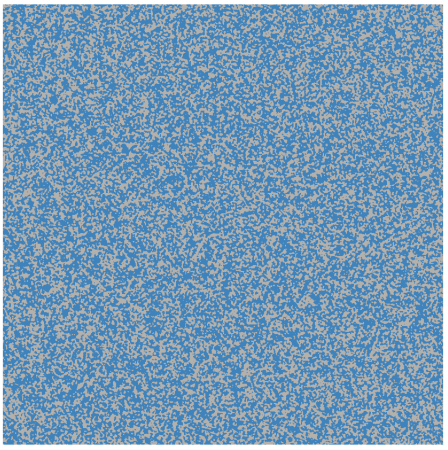

FIGURE 2.9: Porous network consists of one class of pore (MAT1) with 56% of porosity, $L_c = 0.003\mu m$ in a domain of $1\mu m$

Whereas, pore distribution curves often show that in the real material, pores are distributed in a large interval of diameters. Consequently in some cases in order to have a porous network model with a pore size distribution similar to the experimental one, an alternative method should be performed to represent an excursion set that integrates several Random Fields with different correlation lengths. In this approach the union of several excursion sets are used and it should be also possible to control their geometrical and topological properties.

One of the important geometrical properties is the pore volume fraction which must be kept constant. When there is an excursion set with only one L_c or in some other cases where there

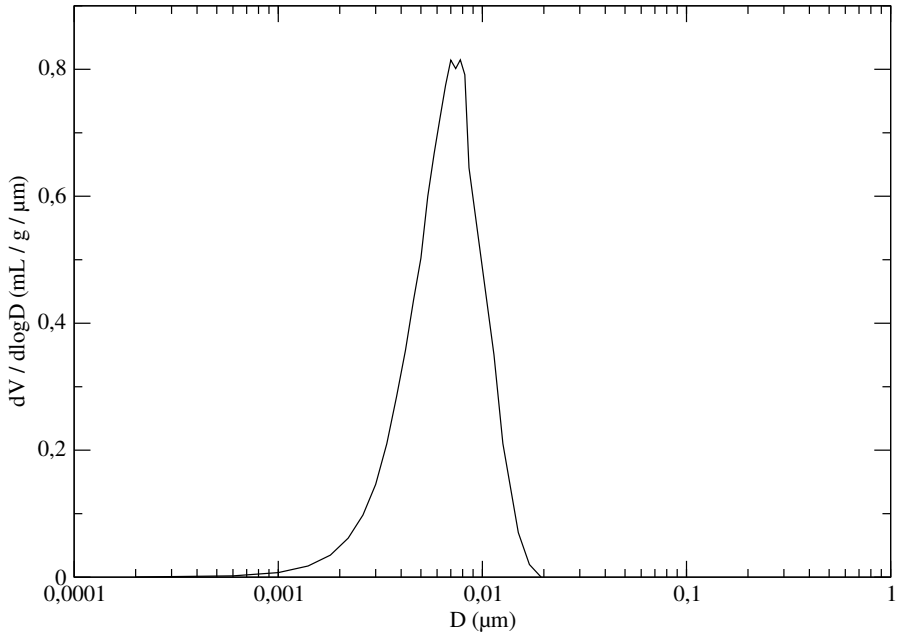

FIGURE 2.10: Pore distribution of Porous network consists of one class of pore (MAT1)

are union of several excursion sets with different L_c, the volume fraction must have the same value in both cases. Hence, it is important to take into account the overlap of small pores and bigger ones in the case of union. Fig. 2.11(a) shows an example of two excursions with different correlation lengths in 2D, both of them are defined in the same domain. The excursion ($\mathbf{A_D}^1$) with big correlated length is shown in light grey and the excursion ($\mathbf{A_D}^2$) with small correlation length is shown in dark grey. Fig. 2.11(b) illustrates the union between them. So it could be observed that to achieve a certain pore volume fraction for an obtained porous network morphology, the volume fraction of each component must be increased to counteract the overlap effect.

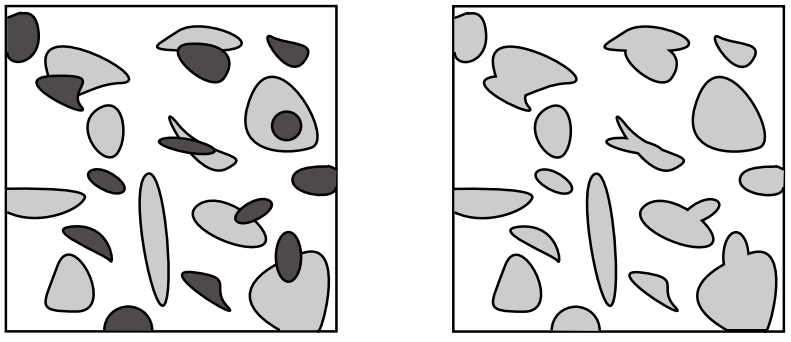

FIGURE 2.11: Union of several excursions

In the following, the mathematical equations are addressed in order to explain the union of several excursion sets.

In this method a set of K independent excursions $\{\mathbf{A_D}^k\}, k = [1..K]$ with certain characteristics is considered. The most important characteristic is the correlation length L_c^k. And finally, the union of all excursions is obtained as a new excursion which represent a set of several characteristic lengths. These excursions are referred as:

$$\mathbf{A_D}^{\cup} = \bigcup_{k=1}^{K} \mathbf{A_D}^{k} \tag{2.9}$$

In order to find LKCs of union, for the union of two excursions represented in Fig. 2.11, it is obvious that they could be obtained by equation (2.10):

$$\mathcal{L}_n(\mathbf{A_D}^{\cup}) = \mathcal{L}_n(\mathbf{A_D}^{1} \cup \mathbf{A_D}^{2}) = \mathcal{L}_n(\mathbf{A_D}^{1}) + \mathcal{L}_n(\mathbf{A_D}^{2}) - \mathcal{L}_n(\mathbf{A_D}^{1} \cap \mathbf{A_D}^{2}) \tag{2.10}$$

But for the union of K excursion sets it is more complicated. In the work of Roubin [13], detailed explanations could be found in order to estimate different LKCs of the resulting excursion after union. General equations are mentioned below.

If K excursions are considered with these correlation lengths ($L_c^1 > ... > L_c^k > ... > L_c^K$, the LKCs can be computed by equation (2.11):

$$\mathcal{L}_n(\mathbf{A_D}^{\cup}) \approx \mathcal{L}(\mathbf{A_D}^{1}) + \sum_{k=2}^{K} \mathcal{L}(\mathbf{A_D}^{k}) \left(1 - \bigcup_{l=1}^{k-1} \Phi_N(\mathbf{A_D}^{l})\right) \tag{2.11}$$

Considering the Poincaré formula [69] the union of Φ_N is obtained by equation (2.12):

$$\bigcup_{k=1}^{K} \Phi_N(\mathbf{A_D}^{k}) \approx \sum_{k=1}^{K} \left((-1)^{k-1} \sum_{1 \le i_1 < i_2 < ... < i_k \le K} \Phi_N(\mathbf{A_D}^{i_1}) \Phi_N(\mathbf{A_D}^{i_2}) ... \Phi_N(\mathbf{A_D}^{i_k})\right) \tag{2.12}$$

In this procedure, the achieved excursion set has the characteristics of several Random Field excursions with different correlation lengths, therefore the pore distribution of obtained model has more similarity to the real porous network.

Here, an application of these equations for the union of two excursion sets ($K = 2$) with $L_c^1 > L_c^2$ is given in equation (2.13).

$$\mathcal{L}_n(\mathbf{A_D}^{\cup}) \approx \mathcal{L}_n(\mathbf{A_D}^{1}) + \mathcal{L}_n(\mathbf{A_D}^{2}) \left(1 - \mathcal{L}_N(\mathbf{A_D}^{1})\right) \tag{2.13}$$

In the other case, union of three excursion sets ($K = 3$) with $L_c^1 > L_c^2 > L_c^3$ is considered, and the result is shown in equation (2.14).

$$\mathcal{L}_n(\mathbf{A_D}^{\cup}) \approx \mathcal{L}_n(\mathbf{A_D}^1) + \mathcal{L}_n(\mathbf{A_D}^2)\Big(1 - \mathcal{L}_N(\mathbf{A_D}^1)\Big) + \mathcal{L}_n(\mathbf{A_D}^3)\Big(1 - \mathcal{L}_N(\mathbf{A_D}^1) - \mathcal{L}_N(\mathbf{A_D}^2) + \mathcal{L}_N(\mathbf{A_D}^1)\mathcal{L}_N(\mathbf{A_D}^2)\Big) \tag{2.14}$$

Regarding the presented equations in section 2.2.3 the area or the volume of union excursion could be obtained by considering $n = 2$ or $n = 3$ respectively.

2.3 Application to nanoporous materials

2.3.1 Morphological modelling in 2D

In the previous section, all necessary procedures to model a porous network using Random Field excursion was detailed and it was mentioned that in most cases the union of several excursion sets should be considered in order to obtain a more similar morphological model to the real porous network. In this section 2D examples are indicated to illustrate morphological modelling of a two phases material. A square of $1\mu m$ dimension on each side is considered as the modelling domain and a regular mesh with the fineness of 5000 points on each side was performed to capture even small pores in the medium. In the first example the union of two excursion sets are considered. The correlation lengths of constituent excursions are 0.003 and $0.05\mu m$. 56% of porosity was considered for this porous network and it is called MAT2. Fig. 2.12 shows the obtained porous network.

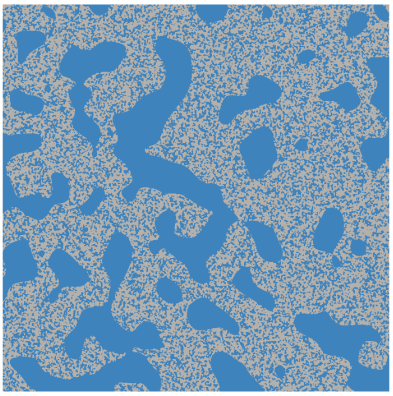

FIGURE 2.12: Union of two excursion sets ($L_c = 0.003, 0.05\mu m$) in a domain of $1\mu m$ with 56% porosity (MAT2)

In the second example, the porous network was created considering five excursion sets. The correlation lengths are $0.011, 0.02, 0.03, 0.05$ and $0.07\mu m$. The porosity of this network is 40% and is called MAT3. Fig. 2.13 shows the generated porous network.

In the next example, seven Random Fields with different correlation lengths of 0.003, 0.005, 0.008, 0.011, 0.02, 0.03, $0.05\mu m$ were generated. These values were chosen based on the pore

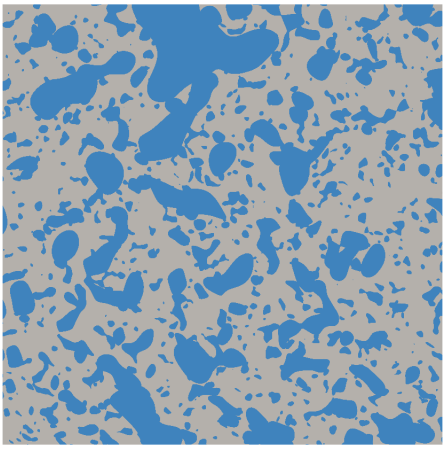

FIGURE 2.13: Union of five excursion sets ($L_c = 0.011, 0.02, 0.03, 0.05, 0.07\mu m$) in a domain of $1\mu m$ with 40% porosity (MAT3)

distribution of cement paste. In the experimental tests, the porosity of $30\% - 40\%$ was registered for the cement paste [1, 2]. However in 2D porous network, the porosity must be increased in order to have a connected network. Accordingly, for the generation of this porous network which is called MAT4, the considered porosity is set to 56%. After applying the threshold values, the union of these Random Fields accomplished so that a porous media with a wide range of pore distribution is obtained. Fig. 2.14 shows Random Fields with different correlation lengths and Fig. 2.15 illustrates the obtained porous media after performing union.

If the obtained morphological model is considered as a porous network, the blue parts could represent pores and the gray parts the matrix.

From a general point of view, the morphological model appears to make a good representation of porous media, and pores are well distributed in the domain. A combination of small and large pores could be seen obviously, which is the result of the union of several Random Fields with different values for L_c. However, the quality of these morphological models must be assessed numerically. For this purpose, morpho-mathematical operations are defined to investigate properties of obtained morphologies. In following sections, different examples of porous network, MAT1, MAT2, MAT3 and MAT4 are analysed using morpho-mathematical operations.

2.3.2 Morpho-mathematical operations

Mathematical morphology is a theory and technique for the analysis and processing of geometrical structures. It could be implemented for the gray scale images but it is most commonly applied to binary images.

As previously mentioned, here our morphological model consists of two components which are pores and matrix. Consequently the numerical model can be represented as a binary image. The morpho-mathematical operations are applied in order to analyse this morphological model.

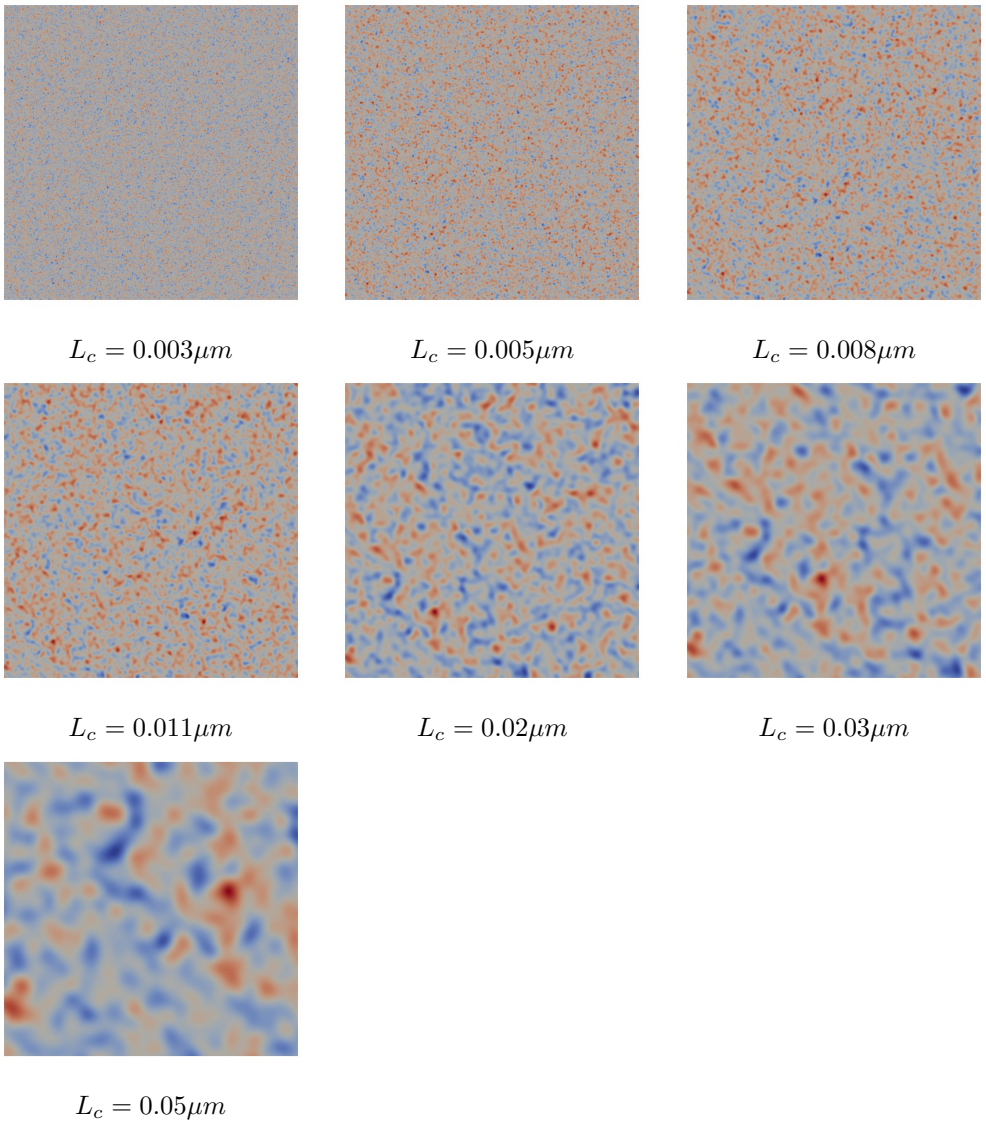

FIGURE 2.14: Random Fields with different correlation lengths

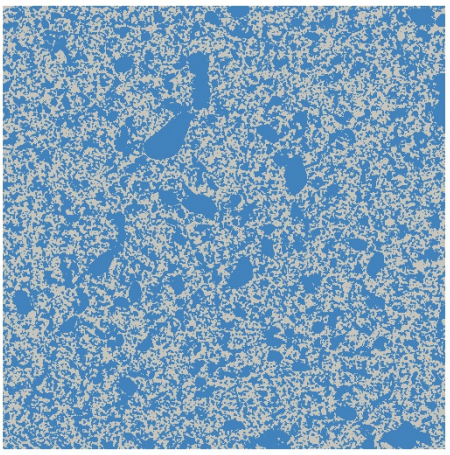

FIGURE 2.15: Morphological model of two phases material in a domain of $1\mu m$ considering union of seven excursion sets (MAT4)

In this approach, a large number of morpho-mathematical operators and techniques exist. Dilation and erosion are the basic operations. It is possible to develop more complicated operations such as opening, closing, geodesic reconstruction and etc. using these two basic operations [15].

In this section some of these operations are detailed.

2.3.2.1 Erosion, dilation

Morphology is based on set theory, thus the fundamental objects are sets. In the morphology of binary images, the sets consist of pixels in an image, pixels are labelled 1 (hereafter displayed as black) or those labelled 0 (hereafter displayed as white). Either black ones or white ones in a binary image may comprise the sets of interest. In this study, in the morphological model of the porous network, black pixels represent pores and the white ones the matrix. Black pixels are chosen to be sets of interest. When an operation is referred on the image, it shall be referring to operations on the set of all black pixels.

In morphological mathematics a test set is also needed. Such test sets provide a means of analysing shape information in the image. Lets E be a simple 3×3 set shown in Fig. 2.16, it is termed as the structuring element. The structuring element can be placed at any pixel in an image, although rotation of the structuring element is not allowed. In order to apply morpho-mathematical operations, some reference pixel in structuring element must be defined whose position defines where the structuring element has been placed. The choice of this reference pixel is often arbitrary. For example, if the set is symmetric the centre pixel may be chosen.

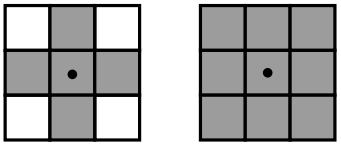

FIGURE 2.16: Typical shapes of the structuring elements, E (black(1), white(0))

The structuring elements could be considered with different shapes. Discs are a natural choice for them especially when the size criteria is interested, since they are isotropic (the same in all directions). However, calculations are very complicated, so another shape must be considered as the structuring element to simplify computing. Accordingly octahedron which has a close form to circle, is an appropriate choice.

Morphological operations transform the image. The most basic morphological operation is erosion. Suppose $\mathbf{S}$ is a set (a binary image or part of it) and E is a structuring element. To apply erosion on the black pixels of set, the reference pixel (i, j) of E is placed at each black pixel of set $\mathbf{S}$, then if (and only if) all of the structuring element pixels are placed in black pixels of set $\mathbf{S}$, the pixel (i, j) in the eroded image will be black. This is denoted $\mathbf{S} \ominus E$ and may be written:

$$\mathbf{S} \ominus E = \{(i, j) : E_{(i,j)} \subset \mathbf{S}\} \tag{2.15}$$

Then the reference pixel of structuring element should pass across all black pixels of set **S**. That is to say, applying erosion compresses the interest set in the morphology. To see how the erosion may be performed on a binary image, an example of a 2D image is shown in Fig. 2.17. In this figure the erosion of **A** by octahedron structuring element is illustrated and the eroded image **g** is obtained.

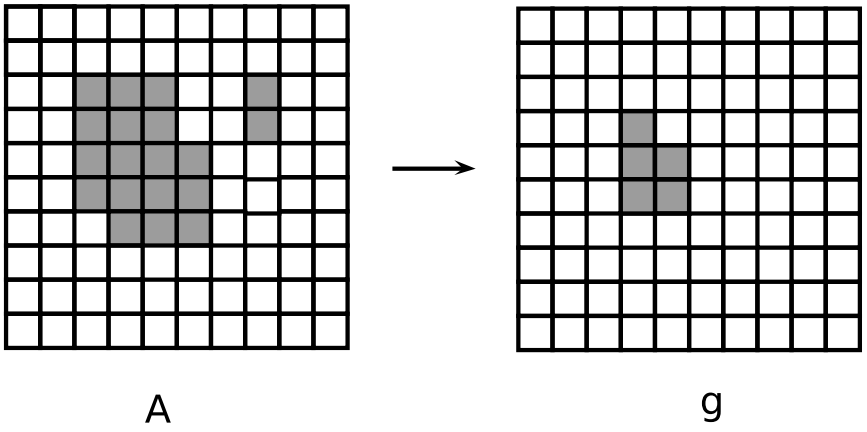

FIGURE 2.17: Erosion process

A complementary operation to erosion is dilation. It is defined simply as the erosion of the complement of a set.

In dilation there is also a structuring element called E, and its reference pixel is placed at (i, j). In this operation, if any of structuring element pixels is placed on the black pixel of set **S**, then the reference pixel of structuring element in (i, j) will be black in the dilated image. This is denoted $\mathbf{S} \oplus E$. Then the reference pixel of structuring element should pass across all pixels of set **S**.

Fig. 2.18 illustrates the dilation performed on a binary image **A** with structuring element of form octahedron, and the dilated image **k**. It is shown in this figure that applying dilation, in contrast to erosion, expands the interest set in the morphology.

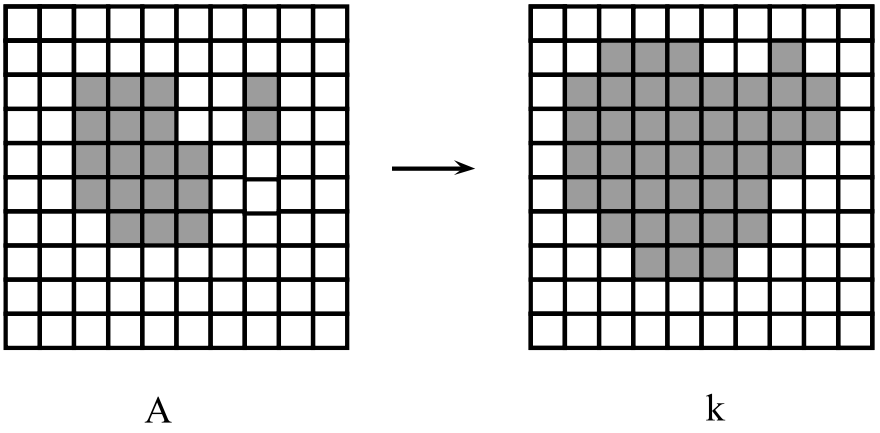

FIGURE 2.18: Dilation process

2.3.2.2 Morphological opening

Previously, the basic morpho-mathematical operations (erosion and dilation) were explained. In the following, two widely used operations in morphological image analysis and processing are discussed. These are the opening and closing operations which are performed using basic operations [70, 71]. Opening is an erosion followed by a dilation, and closing is a dilation followed by an erosion. Opening is denoted $\mathbf{S} \bullet E$, and closing is denoted $\mathbf{S} \circ E$. In this section, more emphasis is placed on the opening operation, because it is applied to obtain numerical pore distribution.

Fig. 2.19 shows the effect of opening on a binary image considering octahedron structuring element. Erosion is applied on the input image and afterwards the dilation is performed on the eroded image. Opening had the effect of removing small black speckle features in the white area of the image, it is equivalent to vanish the speckles smaller than the structuring element.

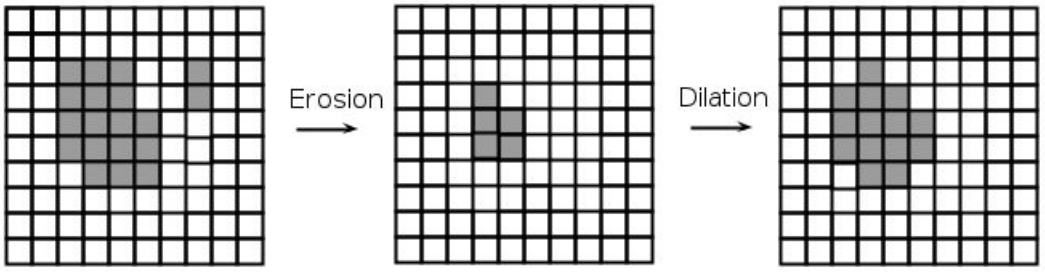

FIGURE 2.19: Opening process

The form and size of structuring element have an important influence on the result of morpho-mathematical operations. If opening operation is performed with different sizes of structuring element, pores smaller than the considered size of structuring element are vanished in each step. Put another way, a filtering of pore size is done in porous network which leads to obtain numerical pore distribution.

Morphological opening with different sizes of structuring element was applied on the 2D morphological model of the porous media and the curve of pore volume in terms of pore size were obtained. Fig. 2.20 to Fig. 2.23 illustrate the pore distribution and cumulative pore volume of the porous network examples.

Pore distribution is one of the tools to assess the quality of morphological model and its similarity to the real porous media. The peaks in this curve clarify that the distribution of pores is in such a way that a considerable volume of pores are with the size around the considered correlation lengths. In other words, the mean of pore size is around correlation lengths. However, there is a little shift which is the consequence of applying union of several Random Fields.

2.3.2.3 Geodesic reconstruction

In the following, another group of morpho-mathematical operations which are the geodesic operations are detailed. In this category there are geodesic dilation and geodesic reconstruction

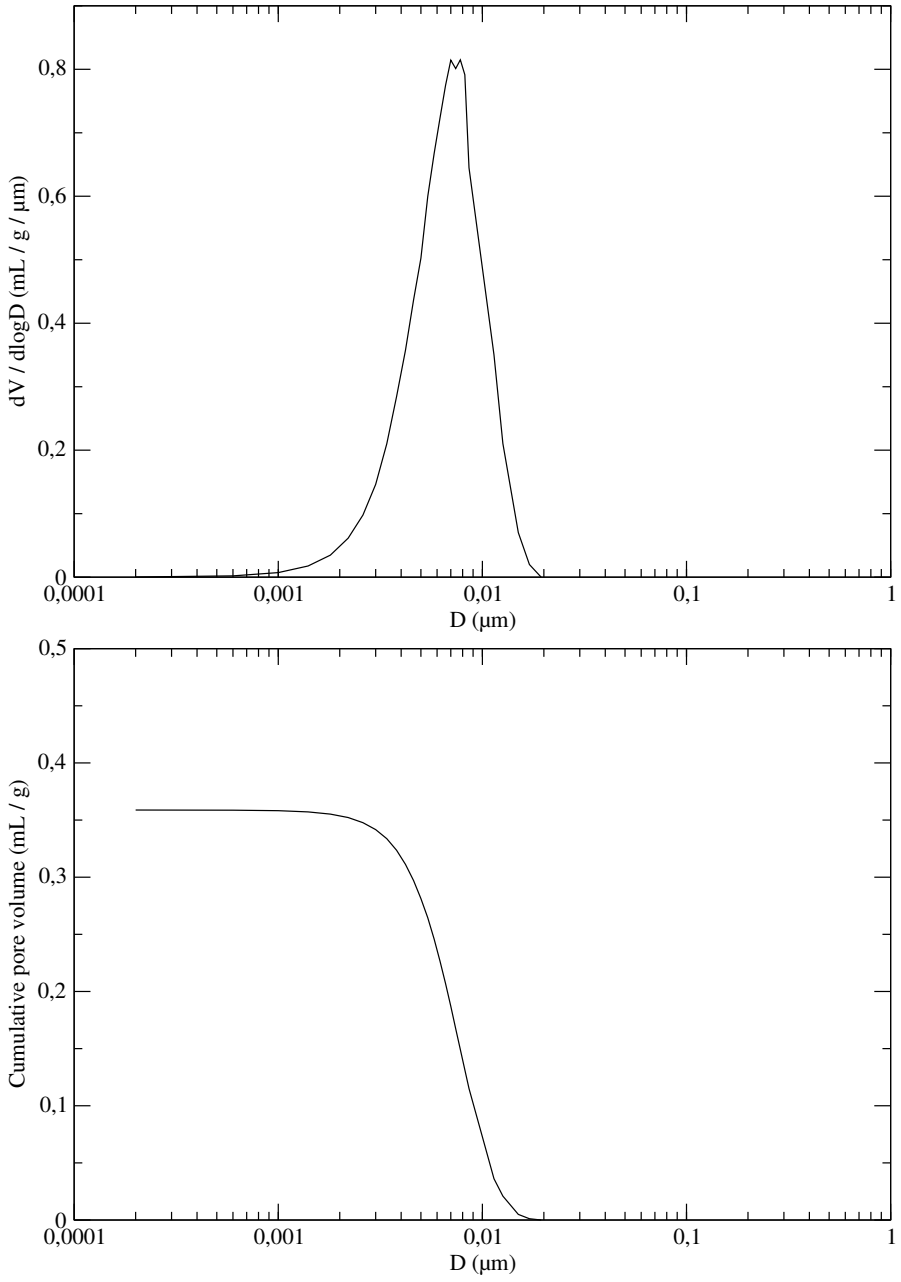

FIGURE 2.20: Cumulative pore volume and pore distribution of MAT1

as basic operations [70, 71]. In geodesic operations in addition to structuring elements, the marker and mask set must be determined.

In mathematical morphology for binary images, the geodesic reconstruction associates a set called *mask* and a subset of it called *marker*. Geodesic reconstruction is obtained by iteration of a geodesic dilation applied to the marker inside the mask. In a binary case, reconstruction by dilation is applied until stability of the geodesic dilation operation.

Geodesic dilation and geodesic reconstruction by dilation are developments of the basic dilation principles. In these operations the idea is using an additional binary image as a conditioning

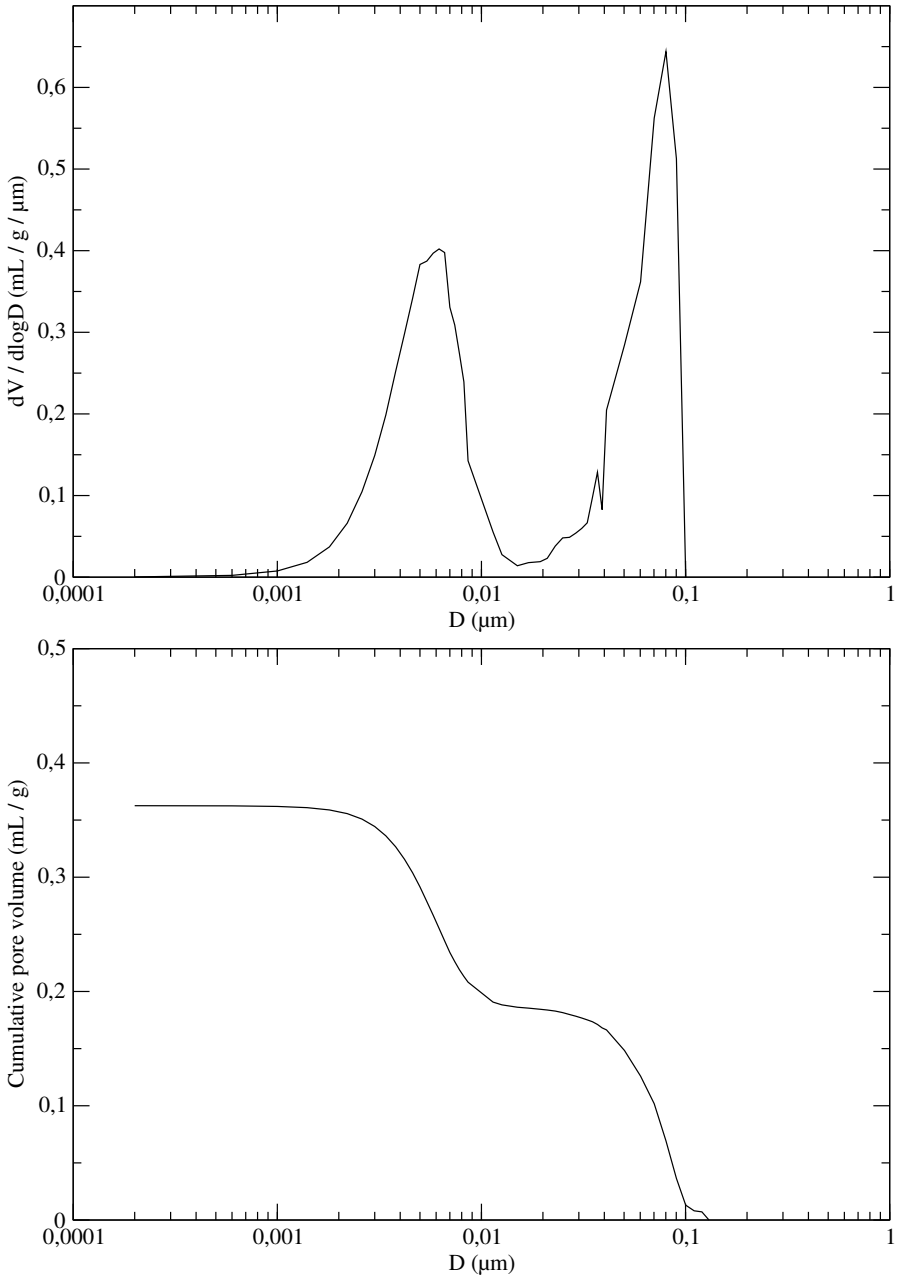

FIGURE 2.21: Cumulative pore volume and pore distribution of MAT2

mask which selectively limits the dilation process. This is achieved by saying that the final image is defined as the intersection of the basic dilation with this conditioning mask.

Suppose $\mathbf{I}$ is the marker and $\mathbf{C}$ the mask image, and $\cap$ is the boolean intersection operator, equation (2.16) shows geodesic dilation δ_E^r:

$$\delta_E^r = (\delta_E(\mathbf{I})) \cap \mathbf{C} \tag{2.16}$$

Where δ_E is the fundamental dilation with structuring element E.

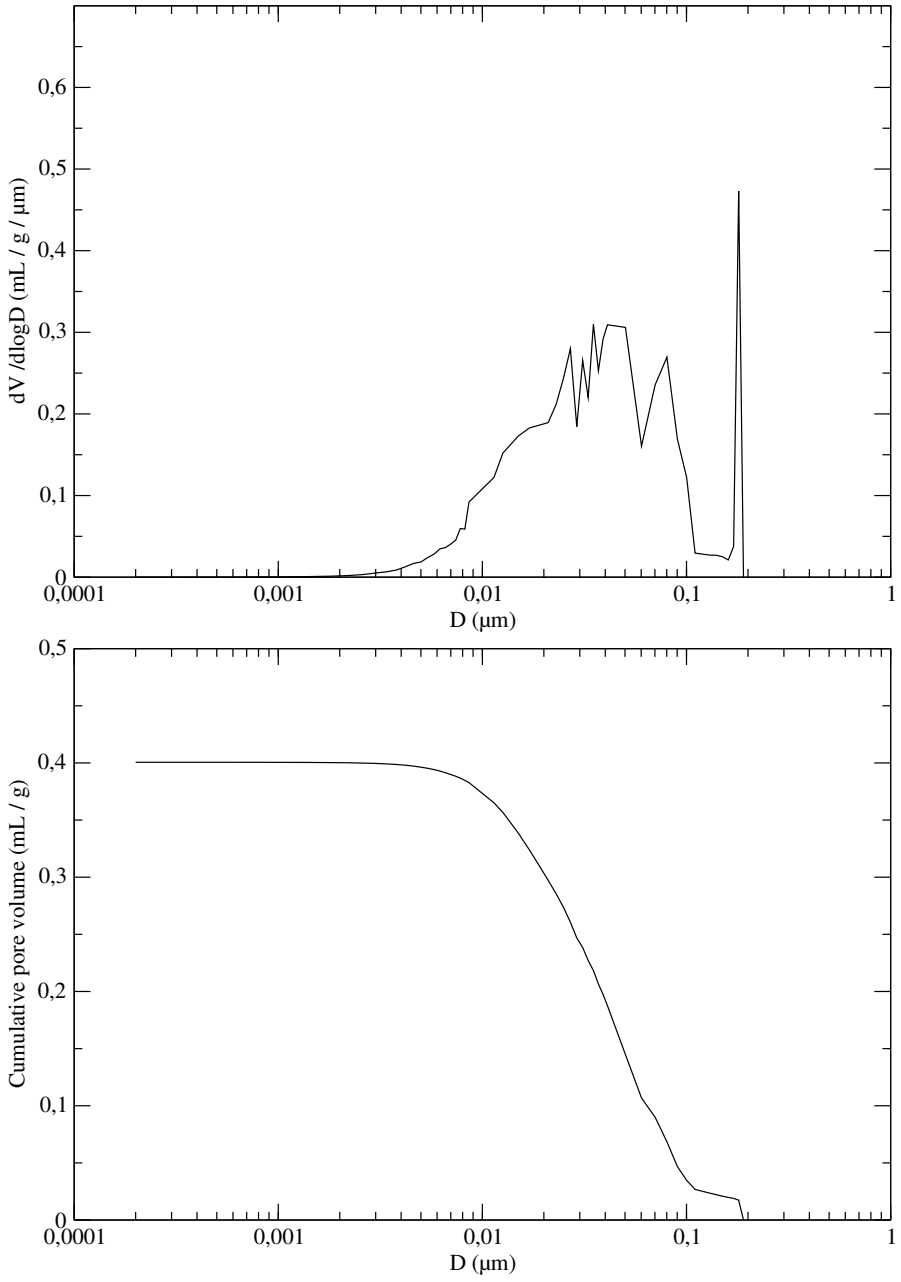

FIGURE 2.22: Cumulative pore volume and pore distribution of MAT3

Geodesic reconstruction consists of N iterations of the corresponding geodesic dilation as it is illustrated later.

Equation (2.17) shows the already given definition for geodesic reconstruction R^r_E.

$$R^r_E = \bigcup^{N\geq 0} \{(\delta^r_E)^N\} \tag{2.17}$$

Where δ^r_E is geodesic dilation and $\cup$ is the boolean union.

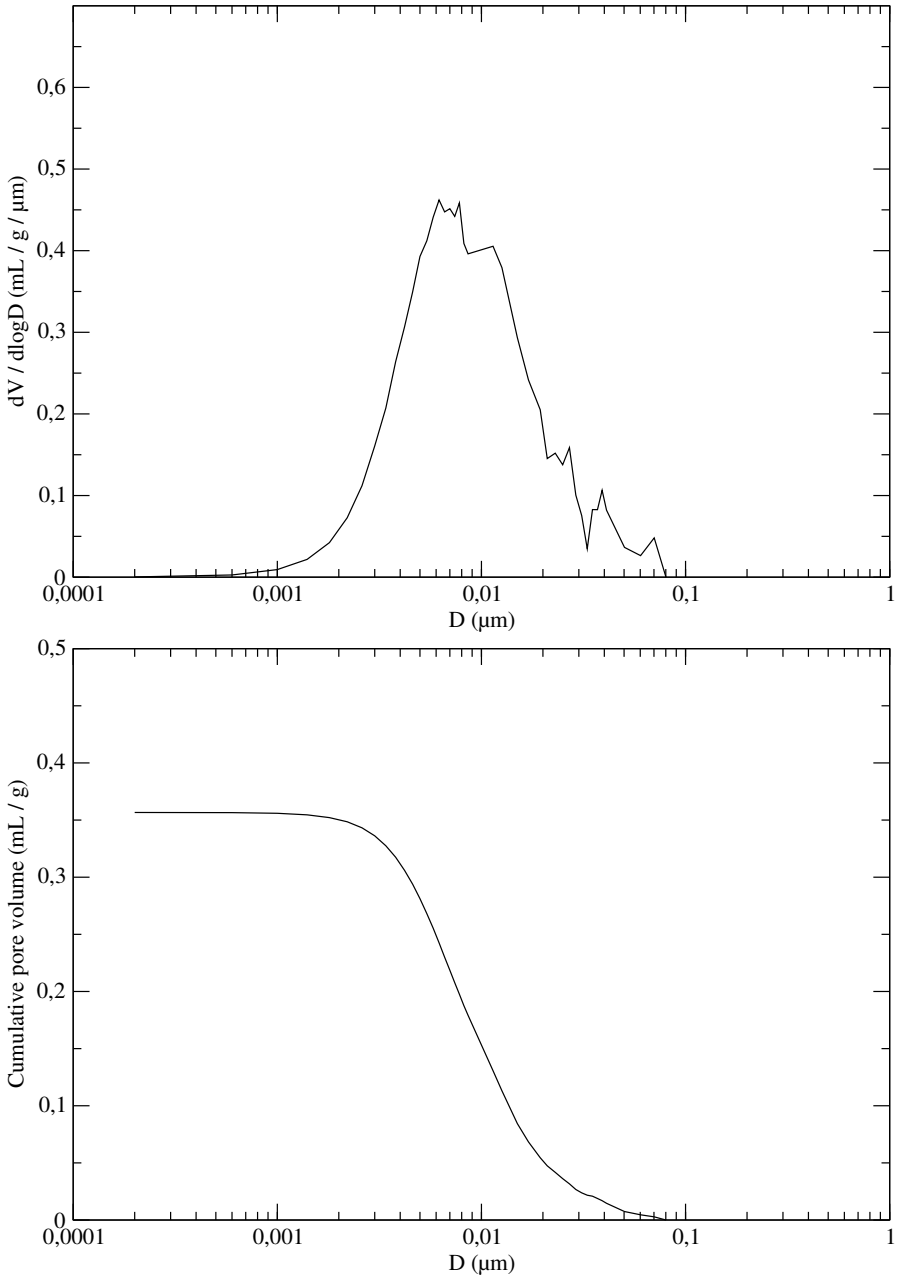

FIGURE 2.23: Cumulative pore volume and pore distribution of MAT4

Geodesic dilation grows region by the specified amount and then removes any growth which have not intersection with the conditioning mask. It should be noted that in the geodesic reconstruction case the intersection with the conditioning mask must be applied after each dilation. In other words, for a geodesic reconstruction of size N the compound operation of $(\delta_E(\mathbf{I})) \cap \mathbf{C}$ must be applied N times, and the geodesic reconstruction is an iteration of geodesic dilation for N times.

These two operations are shown in Fig. 2.24 and Fig. 2.25.

Regarding to the definition of geodesic reconstruction, it is clear that in this operation, in addition to the form and the size of structuring element, the choice of mask and marker have

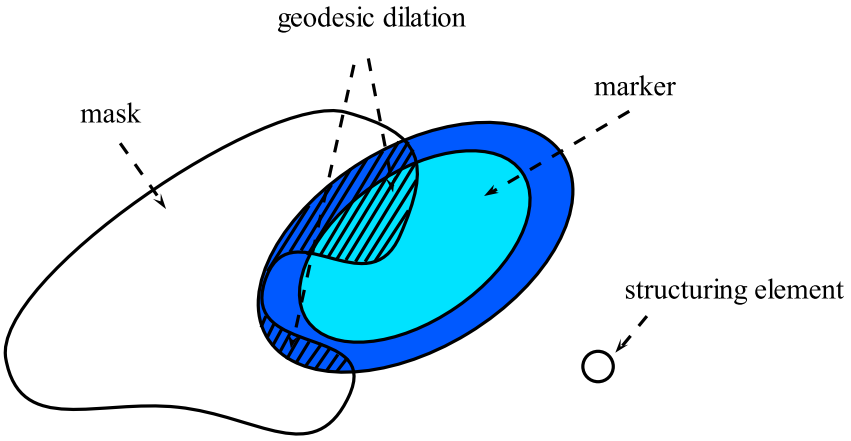

FIGURE 2.24: Geodesic dilation

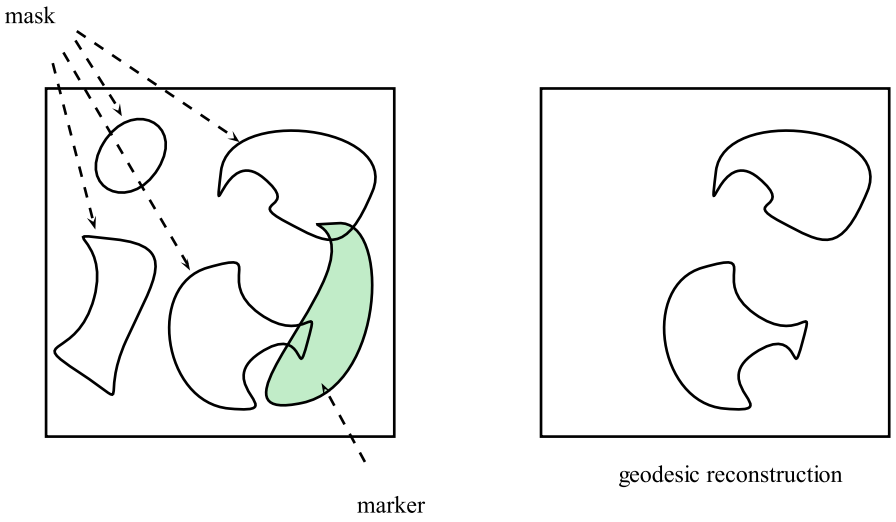

FIGURE 2.25: Geodesic reconstruction

an important influence on the result. For instance, if it is desired to determine objects which touch a particular object in the domain, the particular object should be selected as the marker and all objects in the domain as a mask. In this case, geodesic dilation starts from the set of all black pixels at the particular object and after several iterations, objects which touched that particular object are obtained. The iteration stops when the results of two consecutive iterations are identical and the obtained object does not change anymore. This operation is illustrated in Fig. 2.25.

The geodesic reconstruction by considering the boundary as a marker could be used to find the boundary-touching pores. In this case, the boundaries of domain should be considered as marker and all other objects as mask. Geodesic reconstruction considering boundaries as marker is shown in Fig. 2.26 and it results in connected porosity outwards. Fig. 2.27 shows the morphological model of a two phase material (MAT4) in left and the result of geodesic reconstruction considering boundary as a marker in right which results in displaying the connected pores outwards.

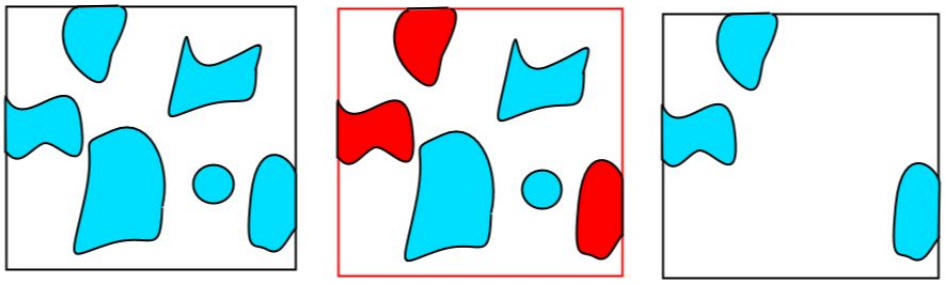

FIGURE 2.26: Geodesic reconstruction considering boundary as marker

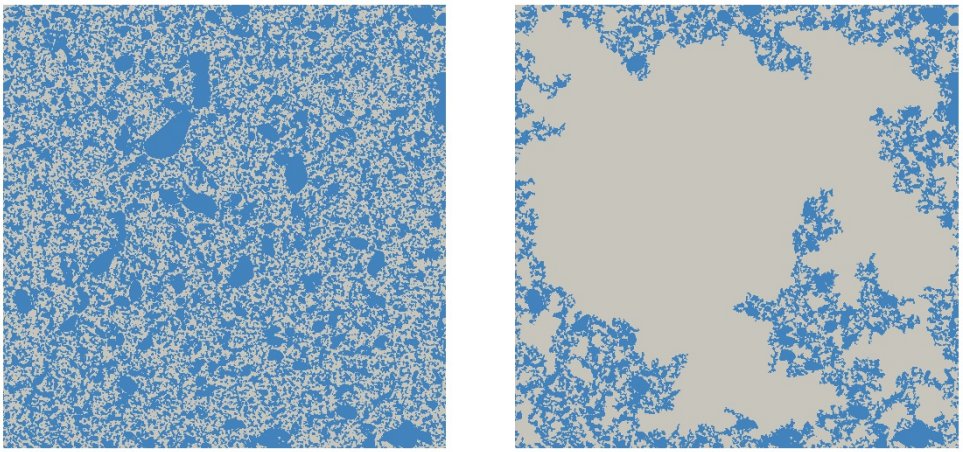

FIGURE 2.27: Morphological model of porous material (MAT4) and connected pores outwards

Geodesic reconstruction could also be applied in order to identify percolation in porous networks. When two opposite boundaries are considered as the marker, percolation of the porous medium between these two faces could be detected.

2.3.2.4 Geodesic distance

Geodesic distance is another morpho-mathematical operation that is applied in this study. Its concept is the number of steps that would be passed on carrying out geodesic reconstruction. That means the number of iterations of geodesic dilation in process of geodesic reconstruction.

By using this notion the percolation paths could be detected and the longest path from the center of the sample to the outwards is identified. This specification is useful to estimate the tortuosity of porous network.

Fig. 2.28 also illustrates the geodesic distance in one of studied examples of morphological model (MAT4). In this example the maximum distance geodesic is 6221 which is the number of geodesic reconstruction steps to pass from the boundary of domain to the center of it, by the longest path. Regarding the fineness of mesh, the maximum distance geodesic is equivalent to $1.8663\mu m$. It could be compared with the direct path to pass from boundary to the center of domain, $0.5\mu m$ and it gives a value which correspond to the tortuosity. Tortuosity is also one of the properties

of morphological model which should be considered in order to investigate its quality. In this example, 3.73 was obtained for tortuosity and it looks adequate.

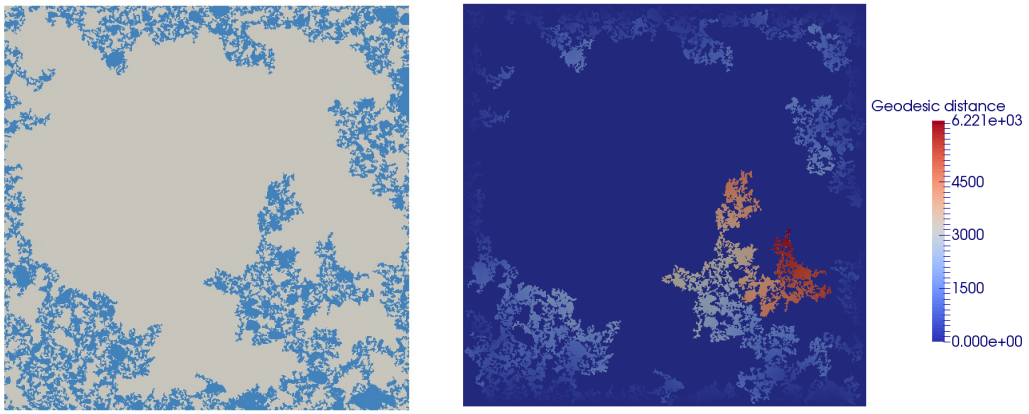

FIGURE 2.28: Connected pores outwards and its distance geodesic in 2D porous network (MAT4)

2.4 Evaluation of the sensitivity of morphological model

Thus far, required operations to apply morphological modelling of porous media as a two-phases heterogeneous material were expressed. Different properties of the morphological model such as pore distribution, connectivity and tortousity were assessed. At the beginning of the modelling, one of the most determinative and susceptible parameter in the generation of Random Field was the correlation length. As mentioned in section 2.2.2.1, in morphological modelling of porous media, this parameter represents the mean of pore size and the choice of it has a considerable influence on the obtained model and its properties. Different examples of porous network considering different correlation lengths were also illustrated in section 2.3.1. In this section, the sensitivity of the model regarding this parameter is assessed. For this reason, the illustrated morphological model of the porous network in 2D (MAT4) is considered another time. This model was generated using the union of seven Random Fields with different correlation lengths and its pore distribution was shown in section 2.3.2.2. In the following, the procedure to generate the morphological model was repeated considering six different Random Fields. In each try one correlation length was eliminated. Morphological opening was applied on the new porous network and the pore distribution was achieved for each case and the model sensitivity to this parameter was investigated.

Fig. 2.29 shows different pore distributions for the morphology generated without considering mentioned correlation length. It is clear that the value of this parameter has an undeniable role in the result. Its changes or even removing one of them could shift the place or the peak value. For example when Random Field with the smallest correlation length ($0.003\mu m$) was removed, lots of small pores with the diameter around $0.003\mu m$ were disappeared. In the same ways, a great amount of large pores were removed by discarding the Random Field with $L_c = 0.05\mu m$.

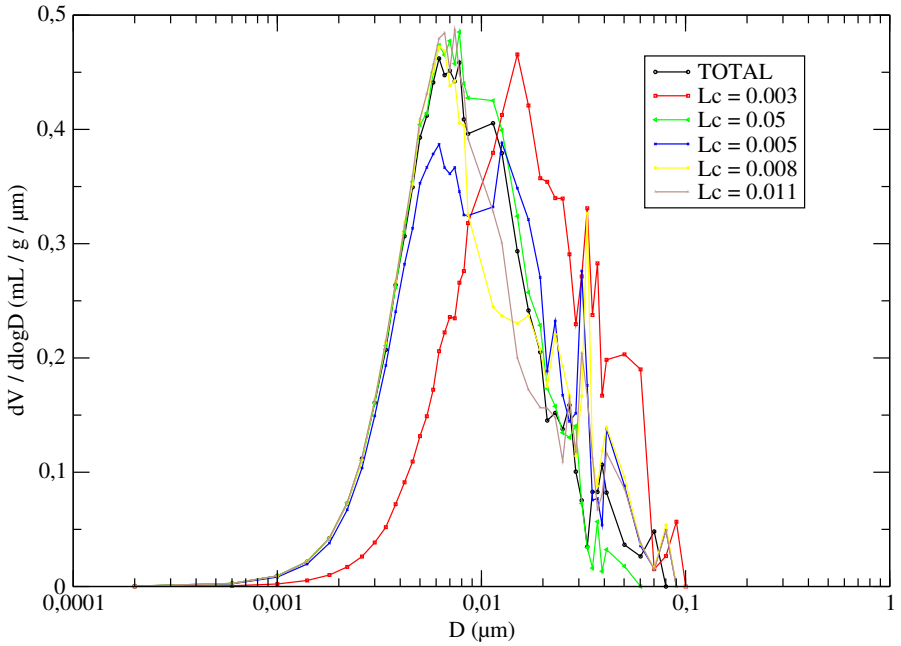

FIGURE 2.29: Pore distribution of the morphological model (MAT4) considering different correlation lengths

2.5 Conclusions

The proposed technique based on morphological modelling of heterogeneous materials was explained in this chapter and it could be concluded that:

- The morphological model of porous material is generated using excursion sets of Random Fields.
- Advantages of this method are:
  - **Contrary to other models, only four parameters (mean, variance, correlation length, threshold) are required to generate a morphological model of the porous network.**
  - **It is possible to control the geometrical and topological properties of the generated morphological model of porous network.**
  - It is possible to consider union of several excursion sets with different correlation lengths in order to have a wide range of pore distribution in the numerical porous network.
- Shortcomings of this method are:
  - Random Fields should be simulated using 'R' program. For 2D porous networks, 25×10^6 points are considered in the domain and the grid size is $0.2nm$.
  - In order to generate Random Fields, an appropriate covariance function should be selected. In this study the Gaussian covariance function was considered, but a real image of material obtained by experimental techniques allows to select a more appropriate covariance function.

- The morphological model of 2D nanoporous materials were generated and their pore distributions were reproduced.
- **The 2D point of view is not acceptable here because the percolation threshold in 2D is about 50%, thus in order to have a connected porous network, the porosity should be increased up to 50% which is too much for cement paste.**

Chapter 3

Application to cement-based materials

Contents

3.1 Introduction

Nowadays, heterogeneous materials have wide applications in the industry and one of the most important issues is to simulate their behaviour. In the previous chapter, creating a realistic model of the porous network was mentioned as the first step to simulate material behaviour. Different models in literature [8, 11, 56] were addressed and a numerical frameworks were explained in order to generate a porous network. In the proposed method, the porous network is modelled using Random Fields excursion. One of the most important advantages of this model is to construct numerical porous media without any assumption on the pore shapes. In this chapter the application of this model to cement-based materials is discussed. The morphological models are generated on 3D using porosimetry results, then they are analysed by applying morpho-mathematical operations.

3.1.1 Definition of framework: Multi-scale approach

First of all, it is very important to define the scales in which our model is used. In this section a short review on different observation scales is given and afterwards an appropriate framework is chosen.

Developed approaches for the study of cement-based materials are usually based on observations and measurements at the macroscopic scale [20]. These approaches suppose the material homogeneous at this scale. However, according to the complexity of the cement-based materials, the macroscopic approach reveals its limitations for certain complex solicitations. Furthermore, the macroscopic properties were related to the microstructure of the material, which is no longer considered homogeneous at this level. The study at this finer scale may provide useful elements for the understanding and modelling the behaviour of these material.

The experimental input data are obtained from the experiences carried out on macroscopic approaches [1, 2]. However the modelling is done at microscopic scale to better characterize the porous network. The effective physical phenomena are also defined at this scale. Hence, using multi-scale point of view gives a more comprehensive vision of the material behaviour at different scales.

In the following, a brief definition of each scale is given. This definition could be done in two classifications. The first classification is based on the studying length in the material. Macroscopic scale is defined as the length which is visible to the naked eye or above few hundred micrometers. The microscopic scale is determined between few nanometers and a few tens of micrometers. And finally the nanoscale is defined by a length of the order of Angstroms.

The second classification is based on the structure of material and its homogeneity. In some cases it may be different from the first classification described above. The macroscopic scale considers the material as a homogeneous unit where physical properties are identical in each points. By contrast, at microscopic scale, the material components are considered homogeneous while their collection is a heterogeneous unit. Finally nanoscale approach considers each molecules and atoms in the material.

In this study, porous network and cement-based material behaviour are simulated at microscopic scale. According to the second classification, the porous network is represented by a heterogeneous set which includes several homogeneous components such as pores and solid particles.

3.1.2 Choice of cement-based materials

As mentioned above, at microscopic scale, the cement-based material is a heterogeneous material with a set of several components. Moreover, the cement-based material could be considered as a porous network in which pores are essential components. Regarding that in pores there could be air or an adsorbed fluid like water. To determine the solid component of cement-based material there are several choices. One of the widely used materials in civil engineering and industry is concrete. It usually consists of three different elements, matrix, pores and aggregates. Therefore concrete has a very complex structure with the presence of different aggregates. It should be noted that the proposed model which is based on excursion of Random Fields, is able to simulate two components material. Hence, concrete as a studying material should be replaced with cement paste which is another basic material widely used in civil engineering. As cement paste is composed of matrix and pores, it is a more suitable choice for the presented modelling.

3.1.2.1 Cement paste structure

A cement and water mixture with relative mass proportions set by W/C ratio produces a hydrated cement paste. The main components of cement are: lime (CaO), silica (SiO_2), alumina (Al_2O_3) and iron oxide (Fe_2O_3). Additions may optionally be used and these additions could modify the cement composition and properties. When anhydrous cement is mixed with water, it results to the hydration of cement's constituents. The calcium silicate hydrates (CSH sheets) and portlandite ($Ca(OH)_2$) are formed during hydration. The amounts of these two hydrates depend on the chemical composition of cement, W/C ratio and the reaction time. CSH is the most important hydrate in the cement paste and it plays a major role in mechanical properties of the materials [20]. Currently, the exact structure of CSH has not yet been described and detailed with enough accuracy.

As mentioned above, cement-based materials are porous materials and their properties are strongly influenced by their porosity. As shown in Fig. 3.1 pores can be distinguished into two types according to their connectivity. Connected pores which are forming a continuous space in the pore network and allow the transport of fluid through the material, and isolated pores (or occluded) that do not have any communication with the outside. It should be noted that the porous network of the cement-based material has a very complex geometry with a randomly distributed microstructure. Consequently the presented model based on Random Field excursion could be an appropriate model for simulations.

As mentioned in chapter 2, some input data are needed for the modelling purpose. Initially the pore volume fraction and the pores distribution must be known to generate a Random Field and to determine the threshold value of excursion. These characteristics of real material are obtained from the experimental results [1, 2]. Therefore the starting point is the result of experimental

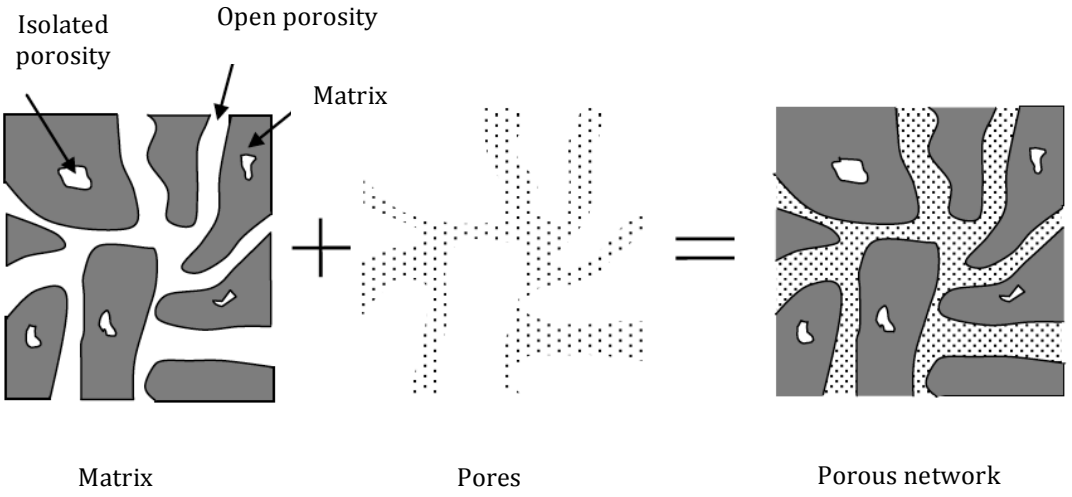

FIGURE 3.1: Schematic representation of different phases of a porous material [1]

studies like mercury intrusion test. In the next section, the procedure to obtain the experimental data are reviewed.

3.2 Experimental data

The characterization of the pore structure of cement-based materials can be detected by various experimental techniques that are complementary to each other. Indeed, a single technique is not able to provide an accurate indication of porosity distribution for all pore diameter range from few angstroms, corresponding to internal porosity between the CSH sheets, to several microns for capillary pores and air bubbles. Moreover, some techniques require preconditioning of samples, for example drying, which may induce changes in the investigated material (cracking) and leads to changes in the porosity and its distribution. Mercury intrusion, gas adsorption, desorption of water vapour as well as scanning by electronic microscopy are part of these techniques.

In this study for the experimental characterization of the structure of cement-based materials, the mercury intrusion test is selected due to its wide use, despite its limitations including not enough precision in the investigation of small pores. In the following, its measurement principles and the experimental protocols are explained.

3.2.1 Mercury intrusion test

As indicated in the latter section, pore distribution is needed to be determined as the input data for the numerical modelling of the porous networks. Knowing this distribution allows to indicate the structure of porous network and gives more information about the porosity in the cement-based materials. Therefore an experimental technique called mercury intrusion is performed in order to characterise the structure of the porous networks and a microstructural analysis of materials.

In this method a non-wetting liquid like mercury is imported in the porous network under different ranges of pressure. When the injection pressure increases, mercury penetrates to the smaller pores. The pore diameter (d) according to injection pressure (P) is given by equation (3.1):

$$d = \frac{-4\gamma Cos\theta}{P} \tag{3.1}$$

Where γ is the surface tension of mercury ($485mN/m$), and the contact angle between mercury and the pore solid surface is $\theta = 130°$.

The volume of injected mercury at each pressure increment gives the volume of pores with its corresponding diameter. In this technique, the injection pressure could increase up to $200MPa$, which corresponds in theory to pores with a diameter of $6nm$. It should be noted that the use of such a pressure could damage the specimen as well as internal cracks, and some changes in the porous network are expected. On the other hand, in low pressures, mercury could not access small pores. Hence, the choice of pressure limit is very important in order to obtain reliable results.

In this experiment, the used samples were of cylindrical form (diameter 36 mm, thickness 10 mm) which were sampled from blocks of $100 \times 100 \times 100$ mm. The samples are dried at 60°C until constant weight. Such temperature was chosen for two reasons: It avoids large water gradients in the material during drying, that reduces produced cracking by such drying. The other reason is the fact that the mercury intrusion test could not have access to very fine pores, and 60°C is a sufficient temperature to drain mercury accessible pores. After placing the sample under a vacuum of $50\mu mHg$ for 5 minutes, it is filled with low pressure (3kPa) and then the pressure increases. The sample is placed under pressure increment during 20 seconds and its mass is measured at the end. The volume of injected mercury corresponding to each injection pressure is registered to obtain pore distribution. Finally, the mercury extracts by reducing pressure [1, 18]. Fig. 3.2 shows pore distribution using mercury intrusion test for a cement paste with a water cement ratio of 0.8.

3.2.2 Characterization of fine microstructures

As mentioned earlier, the main shortcoming of mercury intrusion test is the limited range of pores diameter it can detect due to the limitations that exists for increasing the injection pressure which could misrepresent the real porosity. In the defined injection pressure interval, the small pores are not accessible by the mercury. Therefore, results of different methods could be regrouped to complete the missing information about pore distribution. For example the results of mercury intrusion could be enriched by using another experimental methods like FIB, SEM, TEM or microtomography. These techniques allow to detect small pores. A very short explanation of these methods are addressed here.

The Transmission Electron Microscopy (TEM) is a versatile and powerful tool for microstructural analysis in materials science. In certain observation areas, it could obtain a microstructural

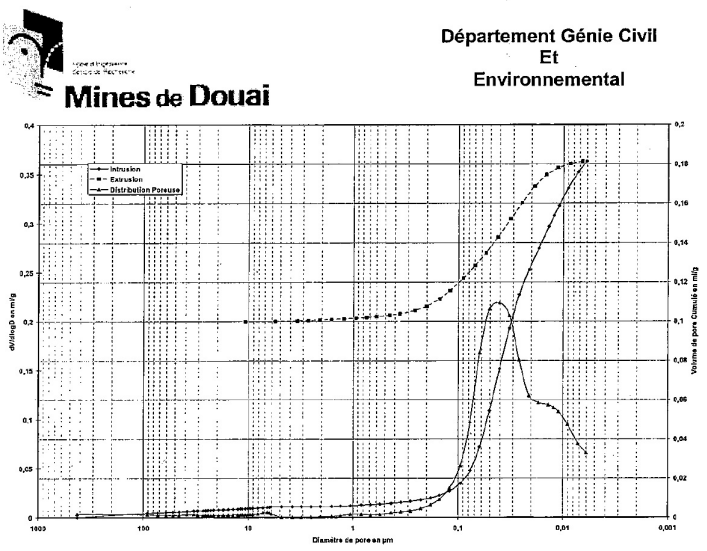

FIGURE 3.2: Porosity distribution for cement paste with $W/C = 0.8$ using mercury intrusion test [1]

image with a nanometer resolution. In this technique an image is formed from the interaction of electrons transmitted through the specimen [72].

Another method which is adequate to detect the nanostructure is the Focused Ion Beam (FIB). This method is used in fundamental material studies. In this technique a scientific instrument that resembles to a Scanning Electron Microscope (SEM) uses a focused beam of electrons to image the sample [73, 74].

Most of the explained methods above are destructive and using them needs to damage or cut the specimen. One of the non destructive methods which allows to characterize the microstructure of porous materials is the microtomography. This technique uses X-ray to reconstruct a three dimensional model of porous network based on cross section images [75–77]. The accuracy of this technique is in the order of micrometer and its not able to detect nanopores. Thus, it is not an appropriate method to model nano porous materials.

Consequently, the modelling in this study is performed considering the pore distribution obtained by mercury intrusion test. Thus, it should be remembered that using the result of mercury intrusion as the input data of numerical simulation could be the origin of some uncertainly in the simulation of small pores.

3.2.3 Determination of input data for numerical modelling

In the first chapter, the numerical modelling based on Random Fields excursion was detailed. This method is applied to model porous networks representing cement paste. For this modelling the needed input data are the pore volume fraction and its distribution. These information are exported from the mercury intrusion experiment done on the cement paste with two different water / cement ratio 0.5 and 0.8 in the work of Wu [2]. The experimental pore distribution curves are illustrated in Fig. 3.3 and Fig. 3.4.

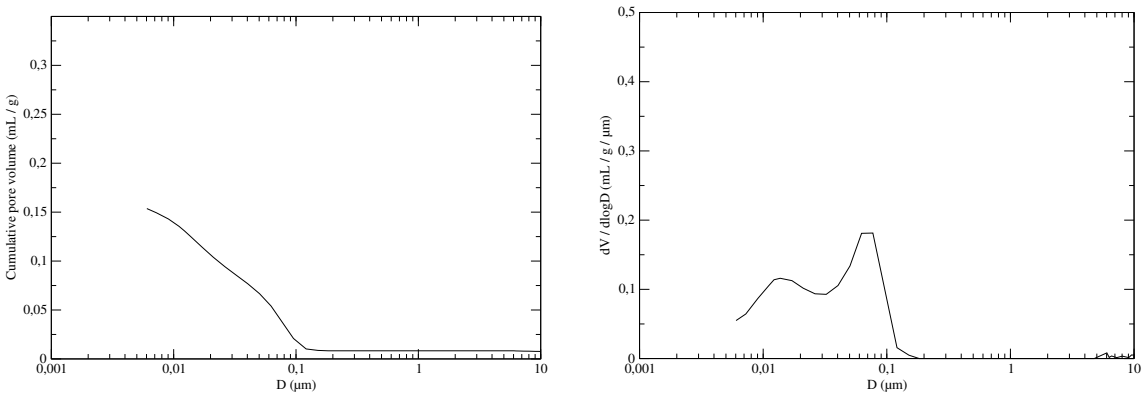

FIGURE 3.3: Mercury intrusion results for cement paste with $W/C = 0.5$ and a porosity of 25% [2]

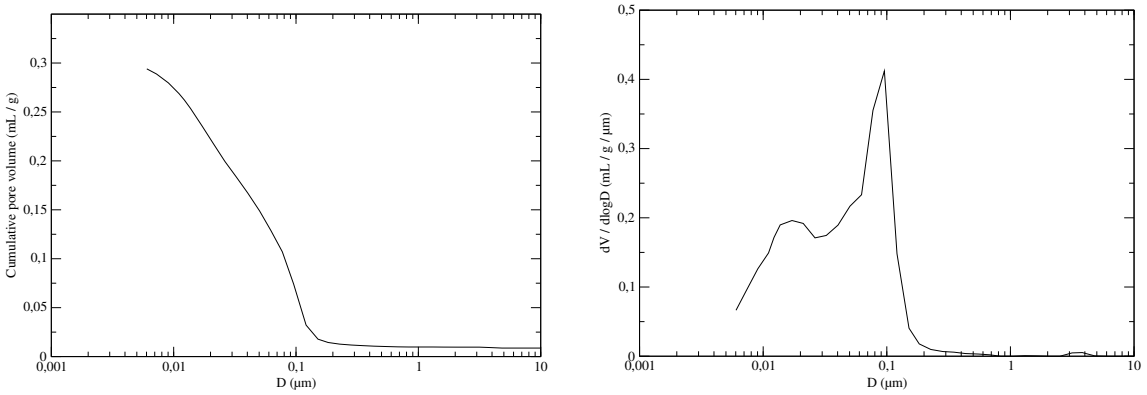

FIGURE 3.4: Mercury intrusion results for cement paste with $W/C = 0.8$ and a porosity of 32% [2]

Mercury intrusion results illustrate 32% porosity for cement paste with $W/C = 0.8$ and for $W/C = 0.5$, the porosity was around 25%. It should be noted that the mercury intrusion test is not able to detect closed porosity, therefore the resulted porosity using this technique does not include this type of pores. Regarding to the numerical models that is able to simulate both of open and closed porosity, it has been decided to increase experimental values with an assumption. There is a final 40% porosity for $W/C = 0.8$ and 30% porosity for $W/C = 0.5$. Fig. 3.5 also shows the comparison between mercury intrusion results for cement paste with $W/C = 0.5$ and $W/C = 0.8$.

Looking at resulted curves of mercury intrusion test, pores are distributed in an extensive pores diameter interval. Therefore, several Random Field excursions with different correlation lengths must be considered in the numerical modelling. As expressed in chapter 2 the correlation length represents the average pores size in the numerical model and its value could be derived considering the pore distribution curve. Accordingly, the experimental curve is decomposed into several parts and the average pores diameter of each part corresponds to the correlation length value. After applying excursion for each Random Field, their union represents the whole porous network. The procedure and required equations to attain union of several excursion sets was detailed in section 2.2.5. The pore volume fraction of each part is determined using the cumulative porosity

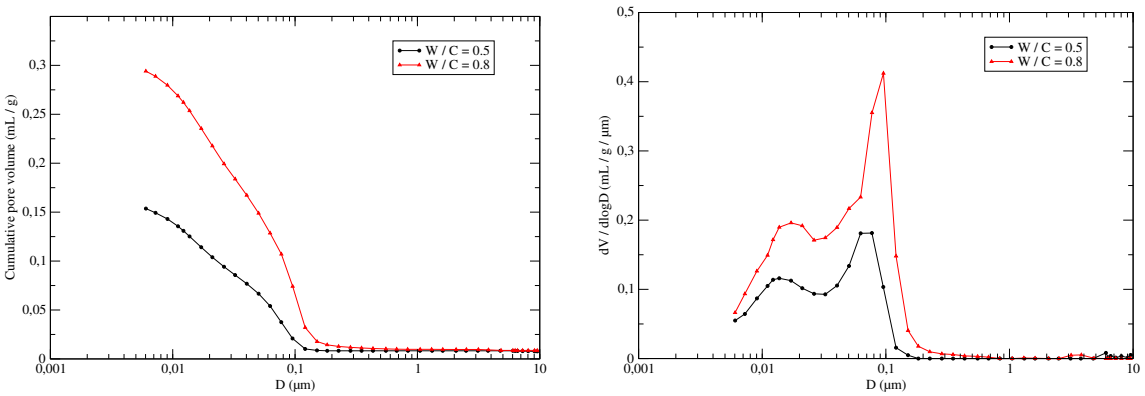

FIGURE 3.5: Comparison of mercury intrusion results for cement paste with $W/C = 0.8$ and $W/C = 0.5$ [2]

curve. When union of several Random Field is applied, the overlap of pores must be taken into account. Consequently, the obtained pore volume fraction should be increased.

Afterwards, based on mathematical equations shown in chapter 2, the threshold value and the hitting set corresponding to each Random Fields should be determined.

3.3 Morphological model of cement paste

In the previous sections, the procedure to generate the morphological model of porous media knowing mercury intrusion results such as pore volume fraction and pore distribution was detailed. It was expressed that several Random Fields with different L_c should be introduced. And based on the experimental pore distribution, it has been decided to generate the numerical model for cement paste with $W/C = 0.8$, using eight different Random Fields taking 0.15, 0.1, 0.065, 0.04, 0.02, 0.012, 0.009, $0.005\mu m$ as the correlation length. This porous network is called MAT5 hereafter. Regarding the experimental curve corresponding to cement paste with $W/C = 0.5$, these eight values for correlation lengths were chosen: 0.12, 0.07, 0.04, 0.025, 0.015, 0.011, 0.008, $0.005\mu m$ and the generated network is called MAT6 hereafter. In chapter 2, 2D morphological model examples were shown, but here for the modelling intent, it is extended to 3D. Thus the studying materials are simulated in a cubic domain with $1\mu m$ on each side. A regular mesh with 800 points on each side is performed, in total there are 512 million points in the mesh. Fig. 3.6 illustrates Random Fields which are used to simulate MAT6. Then the threshold value of each Random Field was calculated and the excursions were applied.

After the performance of union, as the primary result of modelling, a numerical porous network is obtained and illustrated in Fig. 3.7 and Fig. 3.8 for MAT5 and MAT6. In this figure pores are shown with blue and gray parts of the cube represent the matrix.

This numerical result is a morphological model of cement paste with $W/C = 0.8$ in left and $W/C = 0.5$ in right. It is worth recalling that despite most of the suggested models in literature [8, 54, 56], this one is constructed without any assumption on the pore shapes. In what follows, the quality of the numerical model must be verified. This verification could be done considering different criteria using morpho-mathematical operations.

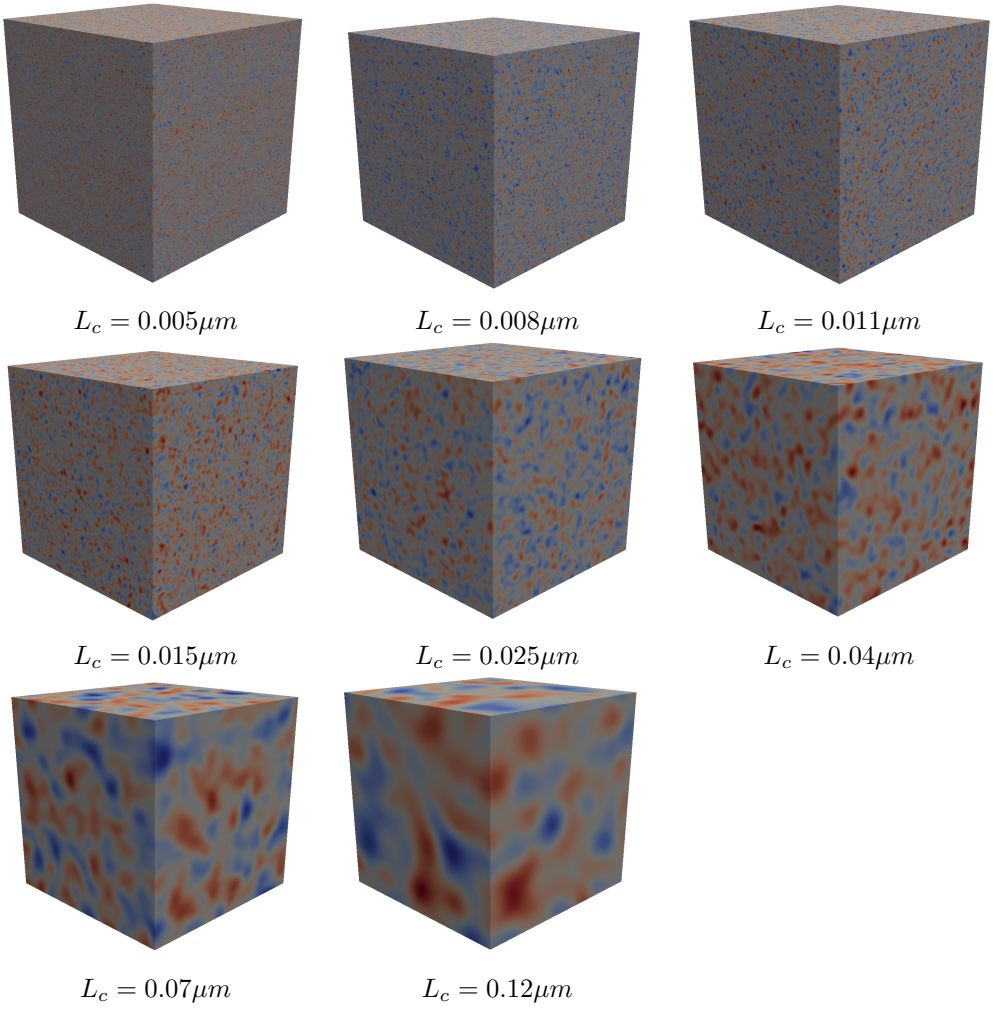

FIGURE 3.6: Random Fields with different L_c

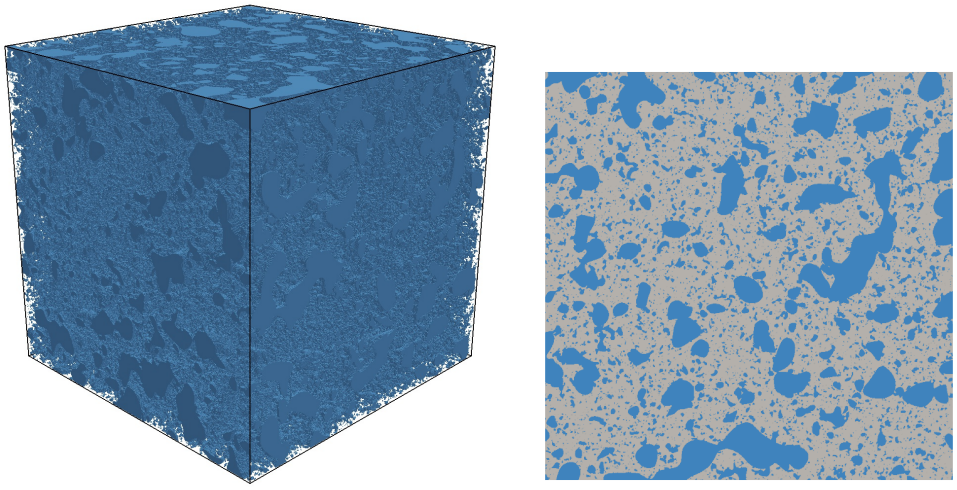

FIGURE 3.7: Morphological modelling of cement paste with $W/C = 0.8$ (MAT5)

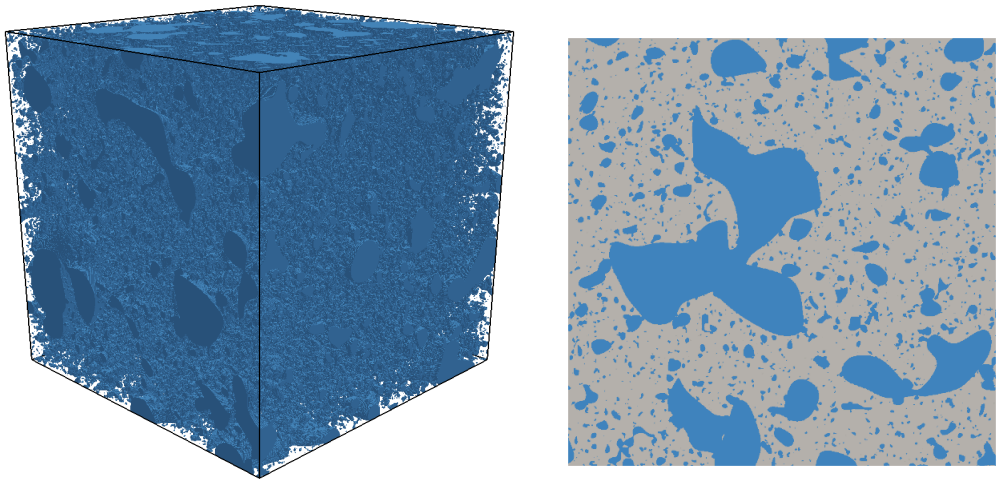

FIGURE 3.8: Morphological modelling of cement paste with $W/C = 0.5$ (MAT6)

3.3.1 Verification of the numerical model

In the previous sections, a morphological model of cement paste based on excursion of Random Fields was presented. Here, some criteria are mentioned to verify the validation of the obtained models.

The first parameter which should be compared between numerical model and the real material is its porosity. In the mercury intrusion test, 32% was obtained for the porosity of cement paste with $W/C = 0.8$. It should be noted that this porosity corresponds to the connected porosity outwards. For the morphological model the connected porosity could be found applying geodesic reconstruction and the obtained value for MAT5 is 35% which is a little more than experimental value but it is nevertheless acceptable. For cement paste with $W/C = 0.5$, the the calculated porosity for MAT6 is 25% which is exactly equal to experimental value.

3.3.1.1 Open porosity and closed porosity

Environmental changes like the variations of relative humidity could influence the behaviour of cement-based materials. Fluid transfer in materials is one of the most important imposed effects of environmental conditions. Hence, the connectivity of pores in a porous network could be a significant characteristic and enough connectivity of pores in numerical models must be confirmed. In porous materials, the porosity is divided in two parts, open and closed porosity. The open porosity refers to the fraction of total pores volume in which fluid flow is taking place, in other words, these types of pores are connected outwards. On the contrary, the closed porosity refers to the fraction of pores volume in which fluids or air are present but fluid flow can not effectively take place. Another definition of this type of porosity is occluded pores which are not connected outwards. Accordingly the porosity is divides in two parts: open porosity and closed porosity, and the volume fraction of open porosity confirms the connectivity of the porous network.

Being aware that open porosity consists of pores connected outwards, geodesic reconstruction is an appropriate operation to detect these pores. The principles of geodesic reconstruction were detailed in section 2.3.2.3. In order to perform this morpho-mathematical operation, the marker and mask should be defined. It was discussed that the choice of mask and marker have an important influence on the result, and different examples of marker and mask were mentioned. It was indicated that by choosing the domain boundary as marker, the connected objects outwards are obtained. Fig. 3.9 shows different steps of applying geodesic reconstruction considering boundary as marker. At the first step the intersection of boundary and mask is obtained and it is called connected part. In the next step, dilation should be applied on connected parts and the intersection with mask should be obtained again. Dilation and intersection operations should be consecutively applied. At the end of each step, the obtained network should be compared with the result of the previous step. When the obtained network at two consecutive steps are identical, the iteration stops and the result of final step represents connected pores outwards.

The two components of total porosity, namely open and closed porosity are illustrated in Fig. 3.10 for MAT5 (porous network representing cement paste with $W/C = 0.8$) and in Fig. 3.11 for MAT6 (porous network representing cement paste with $W/C = 0.5$).

Looking at these numerical images, it could be deduced that the pores are homogeneously distributed in all the cubic domain and there is an acceptable mixture of small pores and large pores.

3.3.1.2 Tortuosity of numerical porous network

In section 2.3.2.4, it was noted that another criterion to validate the morphological modelling is the tortuosity of connected pores in the porous network. For this purpose, the value of maximum geodesic distance should be obtained. The value of geodesic distance represents the number of geodesic reconstruction steps which should be performed to achieve all the outwards connected pores. Fig. 3.12 illustrates the geodesic distance of connected pores outwards for 3D model of cement paste with W/C ratio of 0.8 (MAT5). In this porous network, 643 iterations should be performed in geodesic reconstruction operation to obtain outwards connected pores. Regarding the grid size and the dimension of cube, maximum geodesic distance is equivalent to $1.2\mu m$. It could be compared with the direct path to pass from boundary to the center of domain, $0.5\mu m$ and it gives a value of 2.4 as tortuosity which is a acceptable value. Fig. 3.13 shows the same criterion for the porous network of cement paste with $W/C = 0.5$ (MAT6). In this morphological modelling, geodesic reconstruction operation has 927 steps, thus, the maximum geodesic distance is $1.74\mu m$ and the tortuosity of porous network is 3.5.

3.3.1.3 Numerical pore distribution

Pore distribution is another important criterion that could be useful to validate the morphological model. Experimental pore distribution obtained in mercury intrusion test was used as the input data to introduce the numerical models. In the continue, the pore distribution of

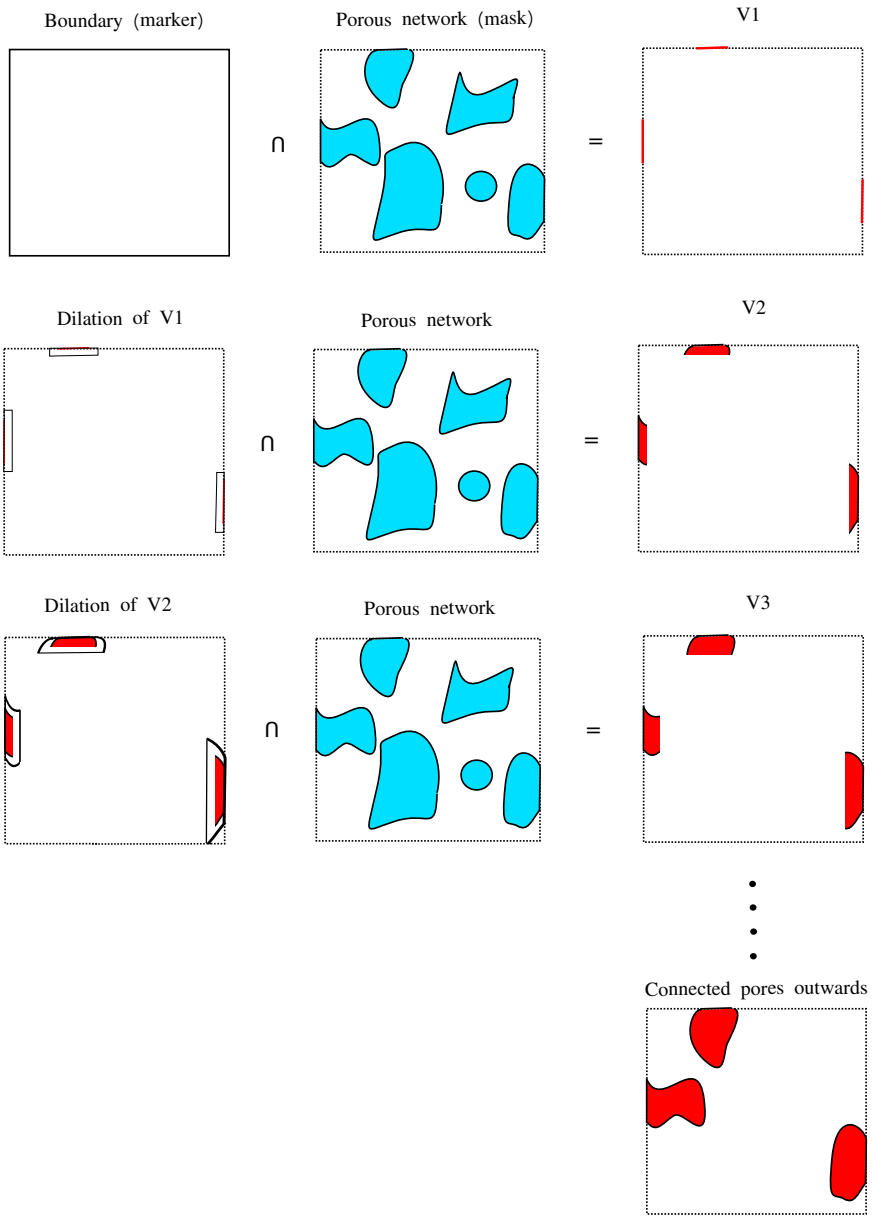

FIGURE 3.9: Steps of geodesic reconstruction considering boundary as marker

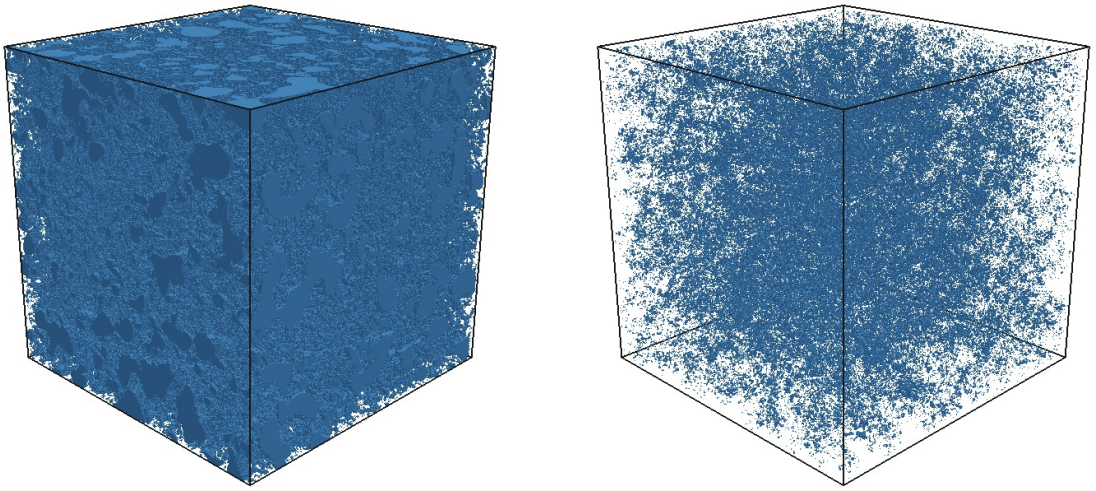

FIGURE 3.10: Open porosity and closed porosity of MAT5 (morphological model representing cement paste with $W/C = 0.8$)

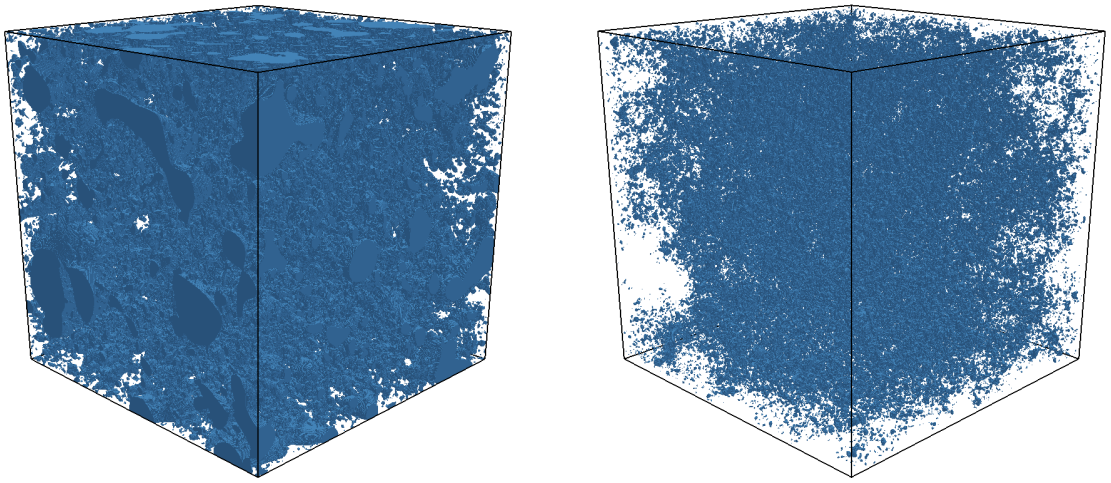

FIGURE 3.11: Open porosity and closed porosity of MAT6 (the morphological model representing cement paste with $W/C = 0.5$)

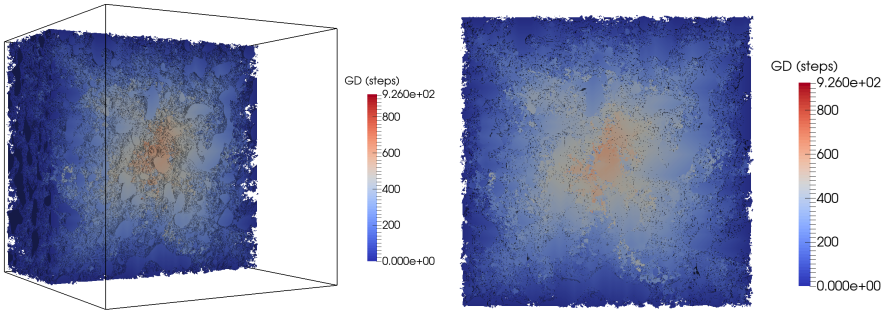

FIGURE 3.12: Geodesic distance of the morphological model representing cement paste with $W/C = 0.8$ (MAT5)

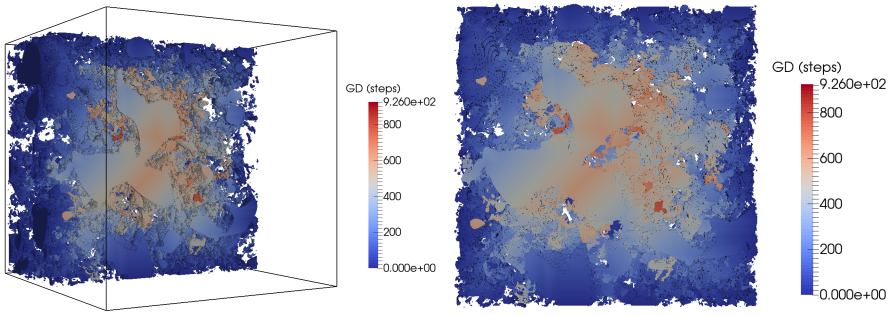

FIGURE 3.13: Geodesic distance of the morphological model representing cement paste with $W/C = 0.5$ (MAT6)

morphological model should be derived to confirm its similarity with the real material. The morpho-mathematical operations are also needed to attain the numerical pore distribution.

Pore distribution is a curve representing the pores volume fraction in terms of its diameter. Put another way, the volume of each pores size in porous media is illustrated in this curve. In order to obtain this curve numerically, a mathematical tool must be specified to filter pores of a particular size. Once pores with a defined diameter are filtered, it is possible to calculate their volume. As indicated in the experimental protocol, the pore distribution curve could be obtained from the results of mercury intrusion. The numerical model is represented by a binary image, therefore, the morpho-mathematical operations are practical means to analyse the introduced model. Previously, the morpho-mathematical operations were defined. Opening could be an appropriate operation to filter the porous network based on pores size.

The morphological opening detects all pores larger than certain size, included open porosity and closed porosity. But the detected volume in experimental pore distribution curve is the accessible volume by mercury which could be described as connected outwards volume. Hence in a numerical point of view, Another morpho-mathematical operation (geodesic reconstruction) should be applied to identify connected volume outwards.

Fig. 3.14 and Fig. 3.15 show the experimental and numerical pore distributions. Numerical pore distributions were obtained once by applying morphological opening and the other time by applying both morphological opening and geodesic reconstruction. In numerical results, it is illustrated that the obtained curve by applying both geodesic reconstruction and morphological opening have trend toward smaller pores comparing to the ones obtained by applying only the morphological opening. This is due to the fact that, in the porous network there are large pores hiding behind small pores (ink-bottle pores), and these large pores could not access outwards simultaneously with pores of the same size. Thus, the volume of ink-bottle pores are accumulated to the volume of smaller pores which were placed on pathway. This results to a delay effect that induces the numerical curve to shift to the left.

Neither the result of morphological opening, nor the result of geodesic reconstruction are similar to the mercury intrusion result. This is due to the fact that, the morphological opening gives pore distribution without considering their accessibility. Moreover, the geodesic reconstruction gives pore distribution regarding their outwards connectivity. Although in the experimental curve filling arrangement of pores and their outward accessibility was taken into account, however due

to the changes of the porous network generated cracks, the same result of geodesic reconstruction could not be obtained. Consequently, the experimental curve is placed within these two perfect cases.

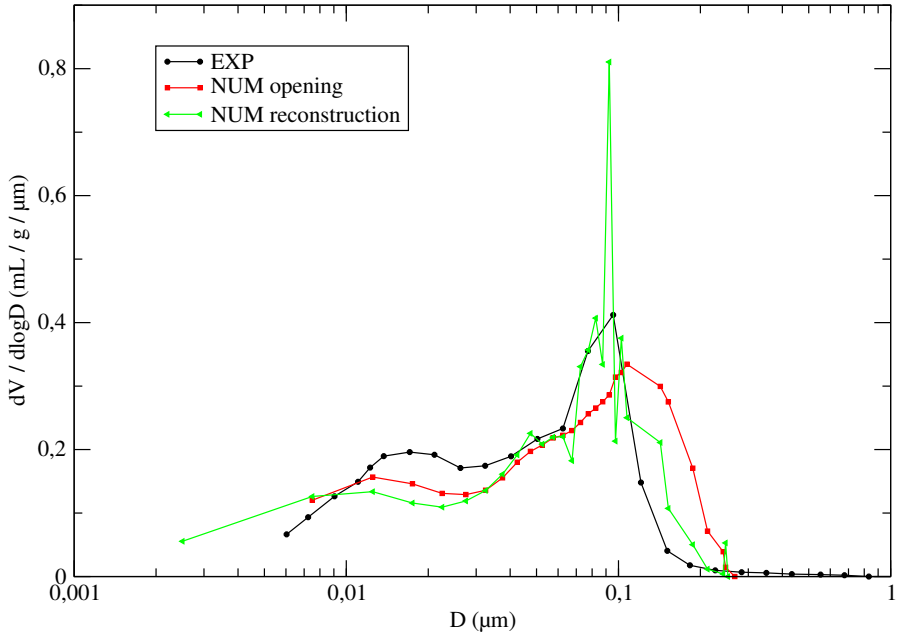

FIGURE 3.14: Numerical and experimental pore distribution of cement paste with $W/C = 0.8$ (MAT5)

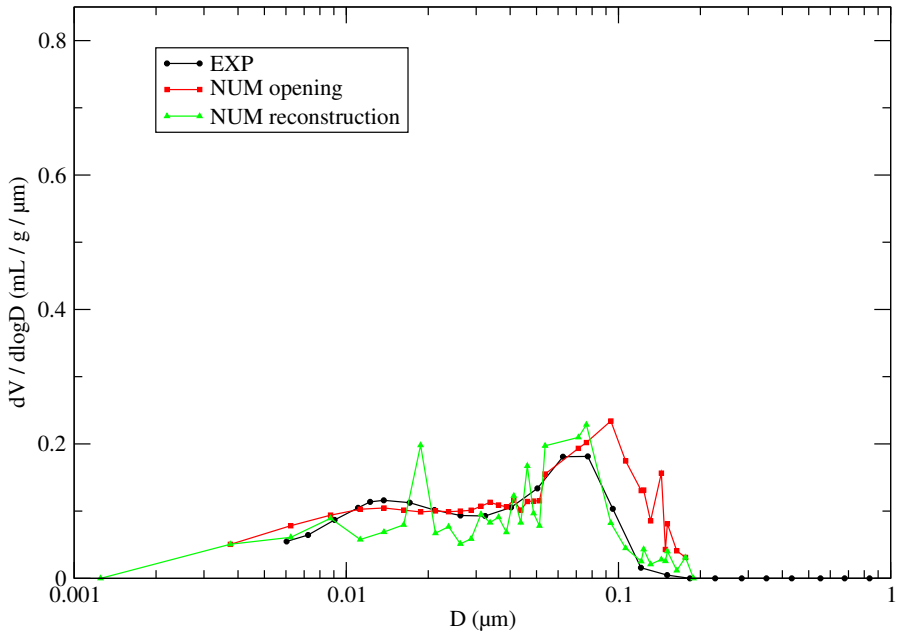

FIGURE 3.15: Numerical and experimental pore distribution of cement paste with $W/C = 0.5$ (MAT6)

3.4 Conclusions

The proposed method in chapter 2 which is based on the excursion of Random Fields was also considered in this chapter and it could be concluded that:

- **The morphological model was extended to 3D and is applied to represent the real material same as cement paste.**
- The advantages of this method are:
  - The porous network of cement paste was well represented by applying morphological model, and pores were homogeneously distributed in the considered domain.
  - Performing geodesic reconstruction lets to separate pores in two types of connected outwards pores and isolated pores. Because in the simulation of hydric behaviour of cement paste, it is important to consider water transfer within connected outwards pores.
  - Tortousity of numerical porous network was verified by considering geodesic distance.
  - **The numerical pore distribution was obtained** once by applying morphological opening and the other time by applying morphological opening and geodesic reconstruction consecutively. Performing these two operations provided two extreme pore distribution curves which surrounded the experimental result. Because in the mercury intrusion test, filling arrangement of pores and generated cracks in porous network due to injection pressure does not allow to attain none of these two perfect pore distributions.
- The shortcoming of the morphological modelling in 3D is the inadequate accuracy due to grid size. In 3D porous network voxel size is $1.125nm$. Regarding this voxel size it is not possible to properly detect pores connections.

Chapter 4

Application to sorption-desorption isotherm

Contents

4.1 Introduction

Studying the behaviour of cement-based materials towards water is an essential point to understand the physical phenomena in this type of materials, in the context of assessing the durability of a structure. Indeed, water is mixed with the cement for the cement hydration process, and it is present in various forms in the hardened materials. This chapter is addressed to the hydric behaviour of porous materials due to the changes of relative humidity. After presenting different roles and states of water within these materials, an investigation of their structure is implemented at microscopic scale. In this chapter, the experimental protocols to obtain sorption-desorption isotherm are also discussed. The physical phenomena associated to drying and wetting process are expressed, and some techniques are proposed from a numerical point of view in order to simulate different porous materials states for diverse relative humidity levels. The numerical simulations are applied on the before mentioned morphological models in 2D and 3D. Finally, the sensitivity of different parameters on results are evaluated.

4.1.1 Cement paste characteristics

It is essential to know cement paste structure in order to understand cement-based materials behaviour and properties [1, 19, 20]. Cement paste is an important factor to supply adherence and cohesion between components gives stiffness and strength to the material. As mentioned in chapter 1 it consists of different chemical compounds, including CSH (calcium silicate hydrate), which are the source of this adhering property, and also pores at different scales, containing water and / or air. Water is an fundamental element which gives handling property and mechanical strength. However, water is also responsible of defect in cement-based materials by increasing its porosity [20]. Pores could be classified in different types regarding theirs scale. For example capillary porosity is in the range of $0.01 - 50\mu m$ and the porosity between the CSH layers which is much smaller is in the order of nanometer.

4.1.2 Water states present within cement-based materials

In chapter 1, it was shown that, water in cement-based materials exists in different types. Condensed water is located in capillary pores and is called capillary water. This water is present between grains of cement, and is progressively consumed to form hydrates. The volume of these pores decreases as hydration progresses [19, 20]. This water is considered free and evaporable by drying at $105°C$. Another type of water is the adsorbed water. This water is located in pores smaller than capillary pores. This is physically due to van der Waals forces and is considered as evaporable water drying at $105°C$ in the oven. And finally the last part of water is the chemically bounded water. This water is reproduced during hydration reactions of the hydrates and is considered as non-evaporable water [1]. In the following, only the capillary water and adsorbed water are taken into account and water vapour sorption experiments allows to highlight the porosity mainly related to the capillary water and adsorbed water.

The contained water in the forms mentioned above in materials is in equilibrium with the environmental conditions (pressure, relative humidity, temperature) in which the sample is placed. Water transfer can occur when these conditions change. In isothermal and isobaric condition, the relative humidity change is the key factor in order to dry a cement-based materials. According to relative humidity value, water transfer within specimen occurs due to different physical mechanisms, as shown by Baroghel-Bouny [19]. Capillarity, diffusion and permeation are some physical phenomena which cause water transfer in cement-based materials. In the following these mechanisms are detailed. One of the tools to express water state within the materials is sorption-desorption isotherm. This curve illustrates saturation degree in terms of relative humidity. Experimental protocols to obtain it are explained in the next section. For researchers [1, 54] modelling isotherm has a great importance to accelerate the cement-based materials behaviour studies, because experimental test are very time consuming, thus numerical simulations can help to save time.

4.1.3 Obtaining isotherm experimentally

The first way to study the hydric behaviour of cement-based materials is sorption-desorption isotherm. The objective of proposed experiments is to characterize the cement-based materials structure, especially towards water transfers. At constant temperature, sorption-desorption isotherm shows the relation between water saturation state of a porous material and relative humidity of the environment, which can be obtained by the experiments of desorption and sorption of water vapour (Fig. 4.1). The water content w at a given relative humidity is defined by equation (4.1).

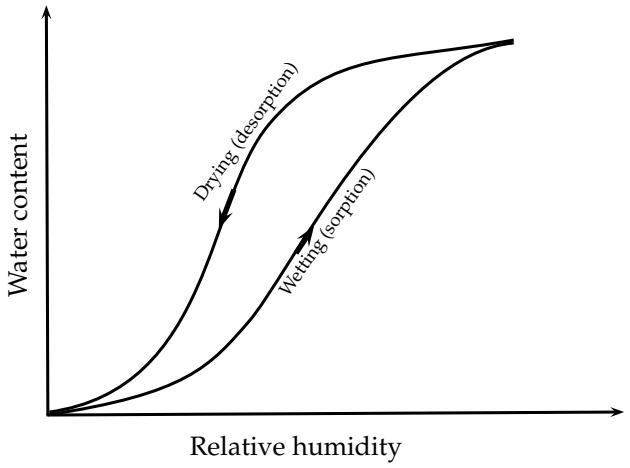

FIGURE 4.1: Sorption-desorption isotherm and the hysteresis between them

$$w = \frac{m_{RH} - m_{dry}}{m_{dry}} \tag{4.1}$$

Where m_{RH} is the stabilized mass of specimen when it is subjected to certain relative humidity and m_{dry} is the mass of dried sample (drying in oven at $90°C$ to reach constant mass). Test

sample is placed at a particular relative humidity and its mass is measured several times in various time intervals to reach constant mass. Then the water content corresponding to this relative humidity level is obtained using equation (4.1). This procedure is repeated for different relative humidities. In desorption test relative humidity decreases to dry the material and in sorption test relative humidity increases to saturate the material. Consequently, sorption-desorption isotherm is drawn applying measured values.

For low relative humidities, adsorbed water on cement paste surface, and for high relative humidities, the capillary water could exist in the considered porous network which depends on the distribution of the pores size. Desorption is then used to characterize the interactions between cement paste and water in liquid or vapour form. A classification has been proposed taking into account the shape of isotherms. Fig. 4.2 shows a classification presented by the International Union of Pure and Applied Chemistry, where isotherms are classified in six major types (IUPAC 1985).

Type I includes the microporous solids (activated carbon, ...) where only a monomolecular adsorption is possible. The more the material is saturated, the more the porous network can easily fill up, it explains the materials behaviour at high relative humidities. Type II corresponds to macroporous materials, where mono and multilayer adsorption are not restricted. Type III represents little adsorbent materials. Various levels in type VI curve illustrate a new layer adsorption on the surface of the material. Cement-based materials usually belong to type IV which corresponds to a solid whose porosity varies from a few nanometers (nm) to few micrometer (microns) in diameter. This figure illustrates a hysteresis between desorption and sorption curves due to the complexity of the porous network.

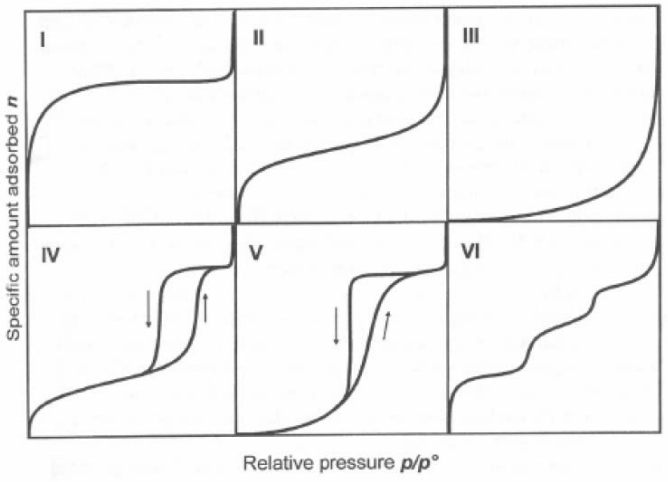

FIGURE 4.2: Isotherm classification by type (IUPAC 1985)

Regarding to the low permeability and diffusivity of cement-based materials, obtaining an hydric equilibrium at each relative humidity level, is relatively long. In the desorption test, it takes 130 days for the maturation of materials and more than 500 days for drying the specimen at different relative humidity levels [1]. Therefore, it is better to perform tests on small specimen in order to decrease test duration.

In the work of Wu [2] an accelerated experimental protocol is developed to obtain cement-based materials isotherm faster. This method is performed on the following thickness samples $1mm$, $2mm$ and $3mm$. In this study, in order to validate the numerical simulations, the obtained values are compared to experimental results of accelerated method.

4.1.3.1 Accelerated experimental protocol

The sorption-desorption isotherm provides an evaluation of pore structure characteristics, such as porosity, pore distribution and transport properties (diffusion and permeability coefficients) [1, 2]. Cement-based materials show very large complexities and macroscopically variabilities due to their different sizes, orientations and forms of their components. The best method to obtain sorption-desorption isotherms is to follow the same sample along the entire test process in order to limit the effect of the significant variability between different samples.

In this technique, samples are initially fully saturated with water and they are then submitted to predetermined relative humidities. When the experiment is performed with large samples, the required time to reach solid-liquid-gas equilibrium is very long. Many researchers [11, 78–80] have chosen to follow different samples for different relative humidities in order to reduce the time of experience. Another solution is to use small samples. In the work of Wu [2] samples with the form of thin disks were used.

In this method cylindrical specimens of studying material were obtained from the core of the beams using a core tube of $37.5mm$ in diameter. Cylindrical specimens were cut with a wire saw in the form of thin disc of thickness $1mm$, $2mm$ and $3mm$ as shown in Fig. 4.3.

FIGURE 4.3: Disc samples used in accelerated method [2]

It is possible to cut discs with the thickness of less than 1 mm but they seemed too fragile. This sample allows a one-dimensional transfer of moisture which is carried towards the two surfaces. They were stored in a climatic chamber in order to regulate temperature and relative humidity. Sample's weight should be measured frequently to get a complete kinetic. The selected relative humidity levels were 95%, 90%, 80%, 65%, 50%, 30% and 12%, in order to cover high, intermediate and low relative humidities at $20°C$. Since three consecutive weight measurements (one week between measurements) do not vary 0.02% of the initial weight, next relative humidity

could be imposed. It is important to know water content to determine the saturation degree. The dry mass is obtained by drying in the oven at $60°C$ and then the temperature increases up to $105°C$. Samples should keep in the oven until the disk mass remains constant. Drying at $60°C$ allows the drainage of the CSH pores, while at $105°C$, it leads to a more complete drainage [81, 82]. Here, the re-saturation of discs was performed to analyse the mass changes. In this experiment, desaturated discs were kept in a desiccator with different relative humidities at $20°C$, after mass stabilization, water content could be calculated for each situation. Fig. 4.4 and Fig. 4.5 illustrate the obtained sorption-desorption isotherms for cement paste with $W/C = 0.5$ and $W/C = 0.8$ in two cycles.

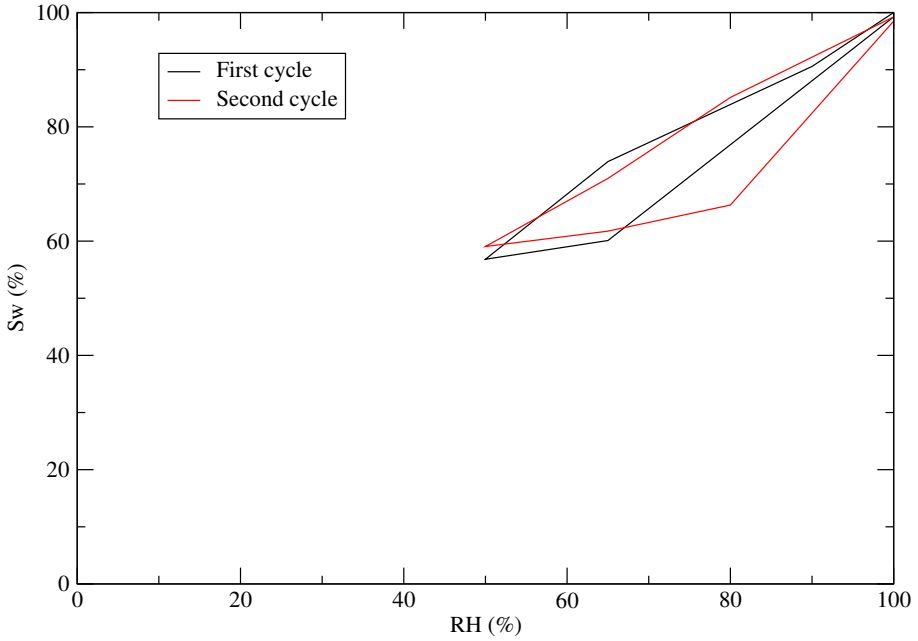

FIGURE 4.4: Sorption desorption isotherm for cement paste with $W/C = 0.5$ [2]

It should be mentioned that in order to study cycles in sorption-desorption isotherms, the relative humidity was only reduced to 50% due to time constraints.

4.1.4 Physical mechanisms influencing isotherm

Cement-based materials consist a solid phase, water as a liquid phase and a gas phase including water vapour and dry air. When the material is in equilibrium with the outside, the interfaces between different phases can be characterized by the capillary pressure and disjoining pressure. Water contained in the material is in equilibrium with the external environment.

As mentioned above, a thermodynamic change such as temperature or relative humidity variation, can imbalance the system and cause water transfer in the porous network to find a new equilibrium in liquid and/or vapour form. Cement-based materials drying can be the result of several processes: gas phase diffusion, transfer of adsorbed water molecules and liquid phase flow. Fig. 4.6 shows the four different types of moisture transfer which is possible in a cylindrical pore, according to different relative humidities [19]. For a fixed temperature, when relative

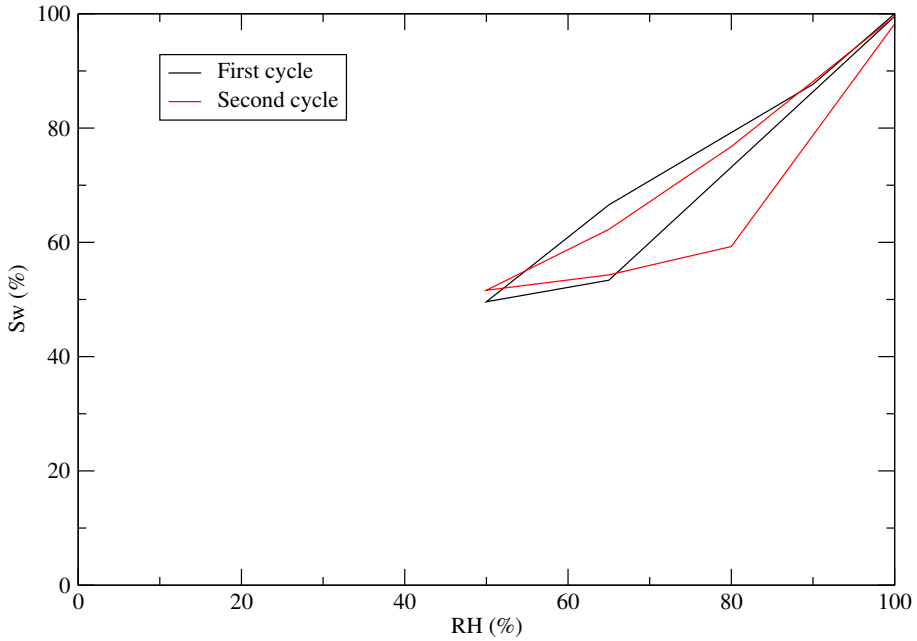

FIGURE 4.5: Sorption-desorption isotherm for cement paste with $W/C = 0.8$ [2]

humidity decreases, cement-based materials dry progressively. Three physical mechanisms can be distinguished according to the relative humidity range.

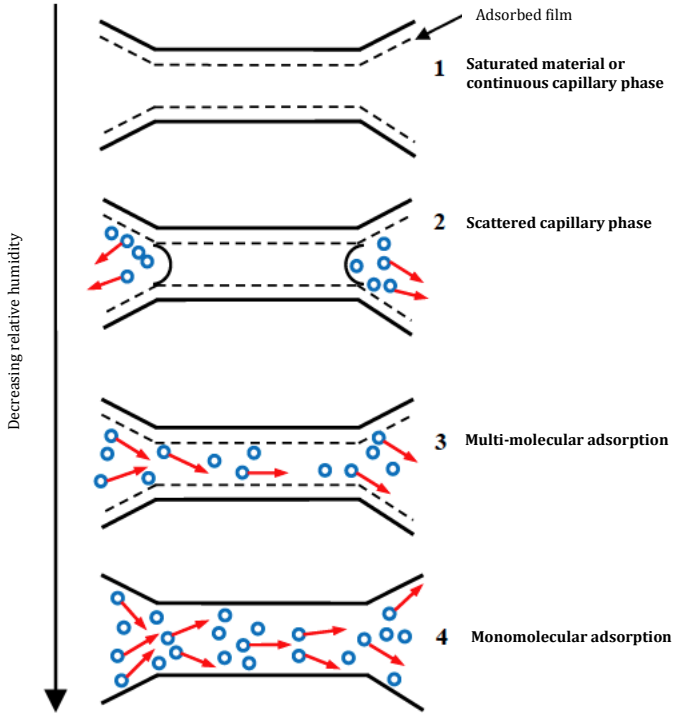

FIGURE 4.6: Four possible types of moisture transfer in a cylindrical pore [19]

Starting from a saturated state of the cement-based materials, drying at high relative humidity

causes a 'capillary' flow to the outside of the porous network. Capillary liquid is present continuously within the solid matrix, therefore water movement is governed by the capillary pressure. Darcy's Law can describe the moisture transport in liquid form.

At intermediate relative humidities, pores are drained and the continuity of the liquid phase within the porous network is not ensured, only small diameter pores contain capillary water. At these relative humidities, the water is present in liquid and gaseous form within the porous network, and it is therefore subjected to evaporation-condensation process which ensure diffusive transport of water to the outside. In this case, the concentration gradient is the driving force of the flow.

At lower relative humidities, only the water vapour and adsorbed water at the surface of pores are still present. In this condition, surface and gas diffusions are causing water transfers. If relative humidity is further reduced, the adsorbed water disappears and only the gas diffusion persists. It should be noted that these changes in relative humidity lead to dimensional variations of the cement-based material, by balancing forces within the material. They are addressed in chapter 5.

4.2 Desorption

4.2.1 Physical definition

In previous sections, the physical phenomena which cause water transfer within materials at different relative humidity levels were described. In the following of this study, among discussed physical phenomena, influence of capillarity is only considered. It should also be mentioned that numerical simulations are based on the geometrical modelling of the porous network. Thus, it is essential to study porous network condition during relative humidity decrease or increase. Lets say, it should be detected that which pores are drained or filled of water at each relative humidity level. Drainage arrangement of pores (pore draining order) could be determined considering pores geometry with taking into account accessibility of different pore sizes.

The pores distribution and connectivity of different pore sizes could affect pores draining order and thus change the isotherm. For the studied materials here, at low relative humidities there is condensate adsorbed water on the surface of cement paste and at higher relative humidities, capillary water is present within material. At different saturation levels, different pore sizes are accessible. At 100% relative humidity, there is a continue flow in all pores. When relative humidity decreases, capillary depression is created in pores. Regarding the difference between pores internal pressure and environmental pressure, a meniscus is produced in the interface of water and air. The large pores are drained earlier because of this depression. Draining smaller pores requires higher depression. The depression increases by decreasing relative humidity and consequently the small pores start drainage. Thus, when relative humidity decreases, more smaller pores become emptied of water. Drained pore size at each relative humidity level could be determined regarding Kelvin-Laplace law. This law is detailed in section 4.2.2.

There is an interesting point in this procedure. Pores draining order depends not only to the size of pores, but also it depends to their arrangement. Because there exists large pores which are connected outwards through smaller pores, and these type of pores are not drained at the same relative humidity with the pores of the same size. They are forced to wait for small pores blocking their way out to dry first. Hence, there is a delay effect here that is compensated at lower relative humidities.

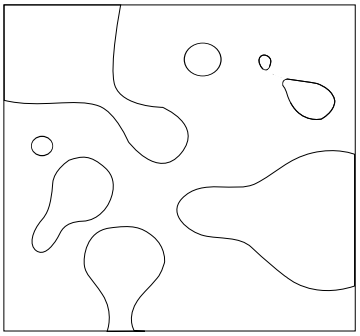

FIGURE 4.7: Two dimensional sketch of a porous network

Fig. 4.7 illustrates a two dimensional sketch of a porous network which is called **A** and Fig. 4.8 shows drainage arrangement of pores by decreasing relative humidity. In this sketch, pores which are marked with characters A1 and A2 have the same size, but they could not be drained at same relative humidity. Pore A1 is connected outwards through a bigger pore, hence it is normally drained according to pore draining arrangement, by contrast to that, pore labelled A2 is connected outwards through a smaller pore B, and it is drained at lower relative humidity along with pore B.

These type of the pores have influence on isotherm form and should be taken into account in numerical modelling.

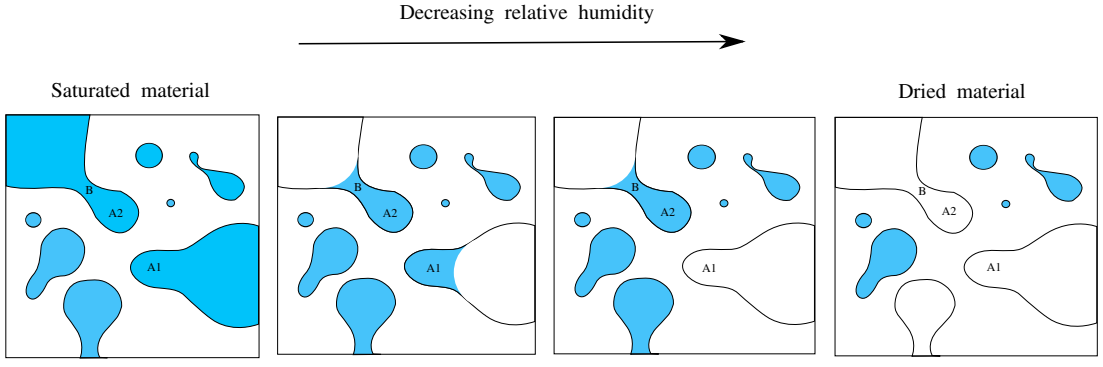

FIGURE 4.8: Desorption in 2D sketch of porous network

As illustrated in the Fig. 4.8 there are occluded pores in the porous network which are not connected outwards. These pores are full of water in saturated condition, and they remain saturated even at low relative humidities when the material dried. However, in cracked material when pore structure changes, these type of pores may be able to connect outwards by the presence

of cracks and they would also drain. These cracks may result from high capillary pressure induced on material structure during desiccation.

A low saturated porous network facilitates gases transfer by permeation. In this condition, most of the pores were drained and accordingly pores are drained easier. But as indicated above, in this study, capillarity is considered as the dominating phenomenon and influence of other physical phenomena would be ignored.

4.2.2 Kelvin-Laplace law

In physical definition of desorption, it is expressed that the porous network is dried over time by incrementally reducing the relative humidity. At each relative humidity level, pores with certain size are drained. The relation between relative humidity and pores size would be explained by Kelvin-Laplace law. This equation is used to estimate the equilibrium location of capillary-condensate water at a fixed relative humidity. Obtaining Kelvin-Laplace equation requires several assumptions [43]. Some of them are mentioned below:

- Capillary water forms a continuous medium.
- Water vapour is a perfect gas.
- Capillary water is homogeneous and incompressible.
- Velocity of each point is zero.
- Capillary water is not subjected to any external force such as gravity, van der Waals force, electric force due to ions.
- Gas (dry air + water vapour) pressure P_g is equal to atmospheric pressure P_{atm}
- Water is in equilibrium with the environment (no evaporation, condensation or drainage).

The porous network of material is assumed to be a network of cylindrical capillary pores equally accessible. Then Kelvin-Laplace law is valid for water in the pores, and can calculate the diameter of the smallest pores desaturated at Relative Humidity (RH) by equation (4.2):

$$d = -\frac{4\gamma.M}{R.T.\rho.ln(RH)} \tag{4.2}$$

Where γ is the surface tension of water, M is the molar mass of water, R the perfect gas constant, T the temperature and ρ the density of water.

Furthermore, the thickness of adsorbed water layers on solid surfaces, which varies according to the imposed relative humidity is not taken into account here. It is discussed as an effect of adsorption layer in section 4.7.

TABLE 4.1: r_c correspond to different relative humidities according Kelvin-Laplace law for water at $20°C$

r_c (μ m)	Relative humidity (%)
Fully saturated	100
0.01005548	90
0.00474785	80
0.00297035	70
0.002074	60
0.00152846	50
0.00115624	40
0.00087996	30
0.00065827	20
0.00046011	10

Table 4.1 illustrates the radius of pore (r_c) called the capillary radius which corresponds to different relative humidity levels according to Kelvin-Laplace equation for water at $T = 20°C$. During desorption, at each relative humidity level, pores with radius smaller than r_c are saturated and pores with radius bigger than r_c regarding their connection path through outwards are drained.

4.2.3 Numerical point of view

In section 4.2.1, the physical procedure which takes place in the porous network during desorption was explained. In this section, a simulation of this physical process considering morphological modelling of porous network is performed by applying morpho-mathematical operations. Finally the representing curve of saturation degree in terms of relative humidity, called isotherm, could be obtained throughout this numerical procedure.

The starting point is the saturated material at 100% relative humidity. When relative humidity decreases, capillary pores can empty only when their size equal or exceeds the Kelvin-Laplace radius as shown in Table 4.1 and when it is connected to the exterior of the sample by a pathway consisting exclusively of the same size or larger than empty pores. At each relative humidity level isotherm could be obtained by computing the drained volume up to that level (Fig. 4.12).

For this calculation, two procedures are needed. At first, pores bigger than the capillary radius should be determined, then connectivity of these pores through outside must be assessed.

For a better explanation, former demonstrated 2D sketch of the porous network in Fig. 4.7 is considered hereafter to illustrate different steps of numerical operations in a more understandable way. In this sketch there are several types of pores with different sizes, like isolated pores, connected pores to the exterior through smaller or bigger pathways. It should be noted that cement paste porous network is represented as a binary image, with 1 labelled cells for pores and 0 labelled cells for matrix. Porous network state during desorption was also illustrated in Fig. 4.8.

In the first step of numerical calculation, a filtering must be performed on the porous network to detect pores bigger than a certain radius. In section 2.3.2.2 morphological opening was cited as

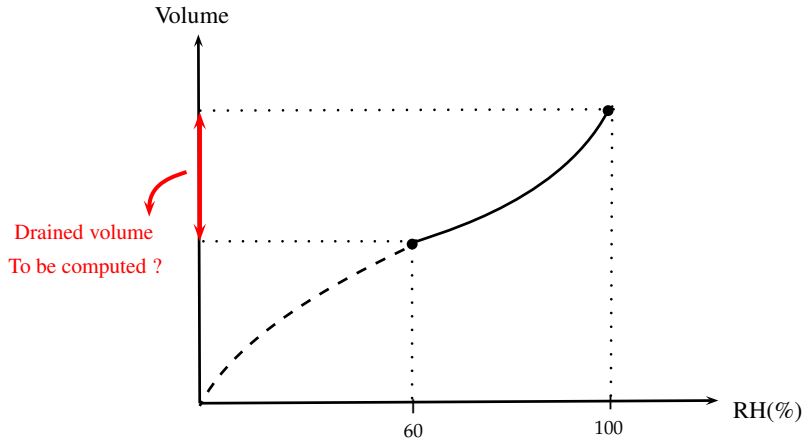

FIGURE 4.9: Numerically simulation of desorption isotherm

an operation allowing to filter a binary image. To apply this morpho-mathematical operation, a structuring element with a defined size is required. Then opening operation is performed on the porous network and pores smaller than the structuring element vanish. If the structuring element size is determined regarding to capillary radius calculated by Kelvin-Laplace law for a certain relative humidity, then the result of opening operation gives pores bigger than capillary radius. Higher relative humidity correspond to bigger capillary radius. When relative humidity decreases, the capillary radius also decreases. Hence, in consideration of smaller capillary radius, structuring element size also decreases and bigger volume could be detected as a result of opening. Fig. 4.10 illustrates the result of opening operation applied on a reference image considering structuring elements with different sizes.

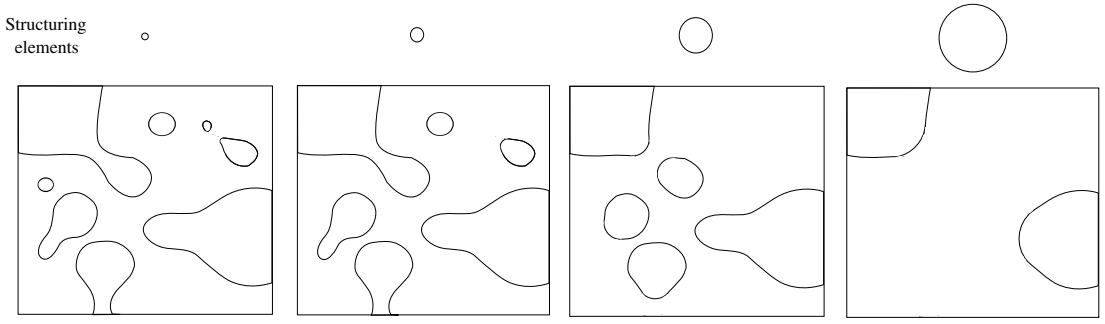

FIGURE 4.10: Opening operation with application of structuring element of different sizes

Detected pores in opening operation, are the ones which could be drained up to a considered relative humidity provided that they would be connected outwards. For assessing the connectivity of these pores to exterior, another morpho-mathematical operation called geodesic reconstruction must be applied. In section 2.3.2.3, for the description of geodesic reconstruction it has been mentioned that if the set boundary is considered as the marker, this morpho-mathematical operation represents the connected outwards parts of the interest set. Consequently to find the drained volume in each step of desorption process, geodesic reconstruction should be applied on the obtained porous network after opening. It should be noted that hereafter in order to investigate outward connected pores, geodesic reconstruction is always performed considering

smallest structuring element of opening. Fig. 4.11 shows the geodesic reconstruction results applied on Fig. 4.10.

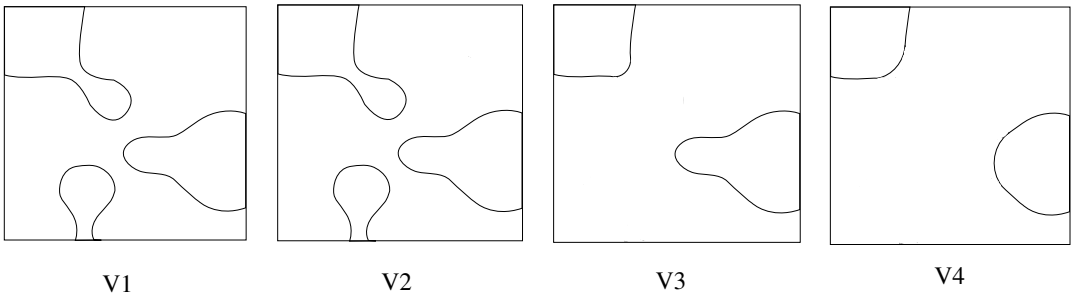

FIGURE 4.11: Geodesic reconstruction application on opening results

Equation (4.3) is also expressed the proposed technique to obtain drained volume during drying ($\mathbf{V}_i^d$) at each relative humidity level (i).

$$\mathbf{V}_i^d = R_3(\mathbf{A} \bullet E_i) \tag{4.3}$$

Comparing Fig. 4.8 and Fig. 4.11 illustrates that the result of geodesic reconstruction of each step, gives exactly drained pores volume for each relative humidity level during desorption. With the efficiency of this technique, the pore drainage arrangement is well regarded by applying opening and geodesic reconstruction operations consecutively. If a big pore is connected to exterior through a smaller pore, in opening procedure the smaller pore is vanished and then, by performing geodesic reconstruction it is detected as non-connected outwards pore and it is not considered as drained pore at this relative humidity. In real porous network, these type of pores should wait smaller pores to drain at lower relative humidities.

After applying these morpho-mathematical operations with different sizes of the structuring element, and obtaining drained volume at each relative humidity level, numerical desorption isotherm could be displayed. Fig. 4.12 illustrates a schematic desorption isotherm with considering volume V1, V2, V3 and V4 as drained volumes up to the considered relative humidity.

4.3 Wetting

4.3.1 Physical definition

In desorption process, relative humidity and along with that the structuring element size decreases until reaching smallest structuring element possible which correspond to the dried material. Then the material must be re-saturated to cover one cycle of isotherm. When relative humidity increases, adsorbed water layers are placed on the solid surface. In the continue of wetting process, the thickness of adsorbed layer increases and consequently small pores are saturated first. By increasing relative humidity step by step, larger pores are also filled.

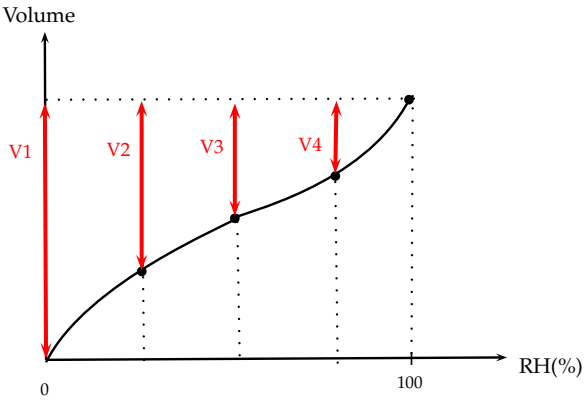

FIGURE 4.12: Schematic desorption isotherm obtained from numerical simulations

Fig. 4.13 shows the reference 2D porous network at different relative humidity levels during sorption.

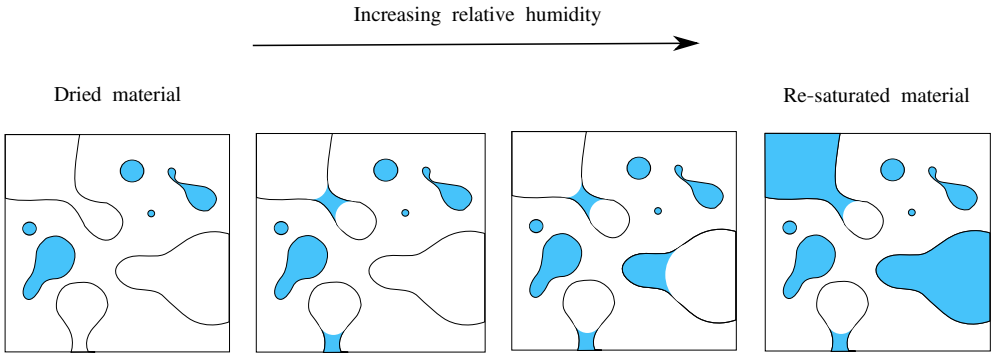

FIGURE 4.13: Illustration of sorption in 2D schema of the porous network

It should be noted that in dried material, closed pores are considered full of water. Because decreasing relative humidity in desorption process was progressively applied and the porous network is supposed to be intact. Hence, the isolated pores which could be drained due to the presence of cracks, are still saturated.

The important point in re-saturation is that pores are not filled in the same order that they drained. Because of large pores which are placed behind small pores. As mentioned above, in wetting process small pores are filled first, because fewer adsorbed layer is required to fill small pores. Then despite the increase of relative humidity, the path is blocked for water to enter large pores and be adsorbed on the solid surface. This phenomenon is called the ink-bottle effect and its details are discussed in section 4.4. However, in long terms, due to some physical phenomena such as diffusion and permeation a part of these pores are filled. In this section, influence of these phenomena are ignored and large pores behind small pores are considered empty even in re-saturated state.

As a consequence of the ink-bottle effect, air can be trapped in the porous medium and leads to a lower saturation degree than the initial state before drainage. For reaching the same saturation level, the material behaviour should be studied in long term.

4.3.2 Numerical point of view

In the proposed numerical method, the size of the smallest structuring element which could be applied in opening and geodesic reconstruction operations is equal to three voxels. By knowing the size of domain and the mesh resolution, the voxel and size of structuring element could be obtained. The accuracy of this method to detect connected pores in the porous network also depends on these values. However, the porous network detected by the smallest structuring element is considered as all accessible pores in studied media. In desorption process relative humidity and along with that the size of structuring element decreases up to the smallest structuring element and the result of morpho-mathematical operations in the last step, represents dried material. In wetting process, relative humidity increases progressively throughout several steps, and the filled volume in each step should be computed in order to simulate wetting isotherm.

The defined morpho-mathematical operations such as opening and geodesic reconstruction are also used in this calculation. The morphological opening is performed by increasing the structuring element size while the relative humidity increases. Then the geodesic reconstruction is applied on the result of opening considering the smallest structuring element, to detect connected pores outwards. In the modelling of wetting isotherm, the method illustrated in Fig. 4.14 is applied to find filled volume by taking into account the ink-bottle effect. In the proposed technique, for each relative humidity level, a subtraction is done to determine the filled volume during two consecutive levels. Equation (4.4) is also shown the proposed technique to obtain filled volume during wetting ($\mathbf{V}_i^f$) at each relative humidity level (i).

$$\mathbf{V}_i^f = R_3(\mathbf{A} \bullet E_i) - (\mathbf{A} \bullet E_{i+1}) \tag{4.4}$$

Fig. 4.14 illustrates that the porous media obtained in opening should be taken away from the result of the former step reconstruction. And Fig. 4.15 presents the wetting isotherm demonstration knowing filled volume of each step.

4.4 Ink-bottle pores and hysteresis

Desorption isotherm presents the drying process of the porous network from saturated state at 100% relative humidity to dried material at 0%. Sorption isotherm shows saturation degree progression in terms of relative humidity in wetting process. Based on experimental results there is a hysteresis between sorption and desorption curves. All mechanisms leading to and having impact on the sorption-desorption hysteresis are still not completely understood, but explanations of the hysteresis phenomenon are presented [83, 84]. This phenomenon is linked to the structure of the porous network and its complexity [85, 86], because all pores of certain diameter are not equally accessible. If a pore is connected to the external vapour phase via a smaller pore, in many cases the smaller pore acts as a neck (often referred to as an 'ink-bottle' pore). Nowadays, this phenomenon is referred to as pore-blocking or 'ink-bottle' effect.

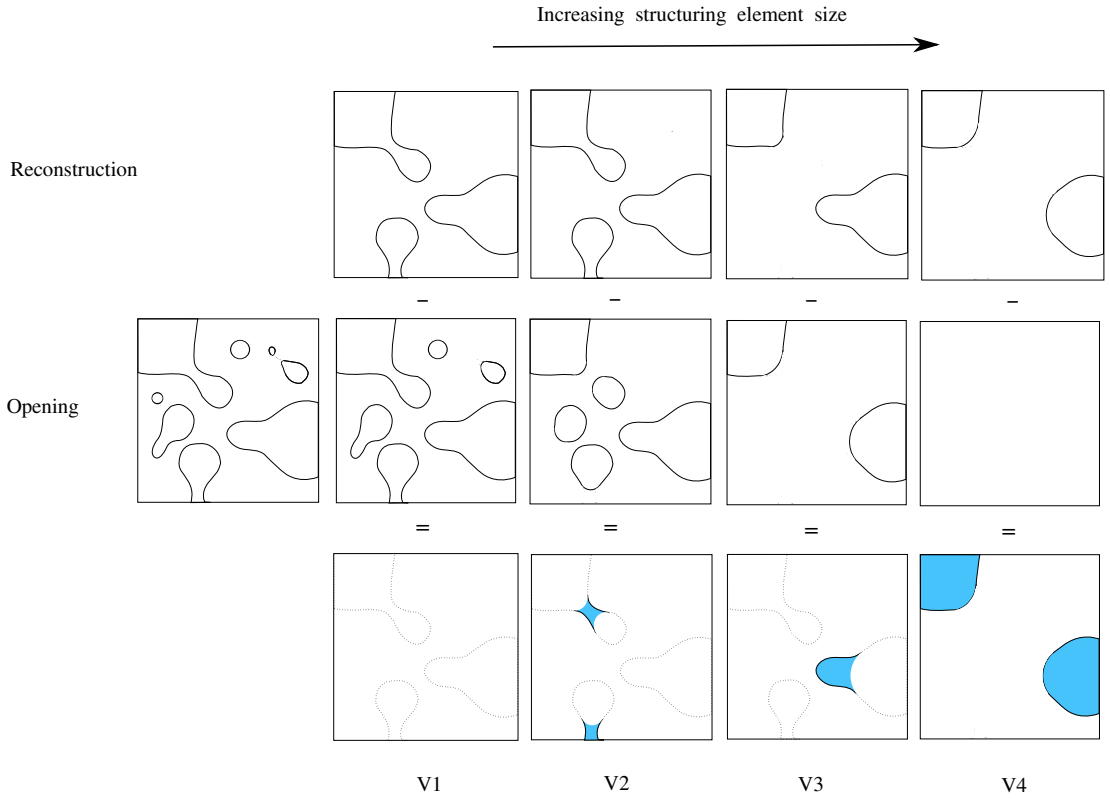

FIGURE 4.14: Proposed technique to find filled volume during sorption

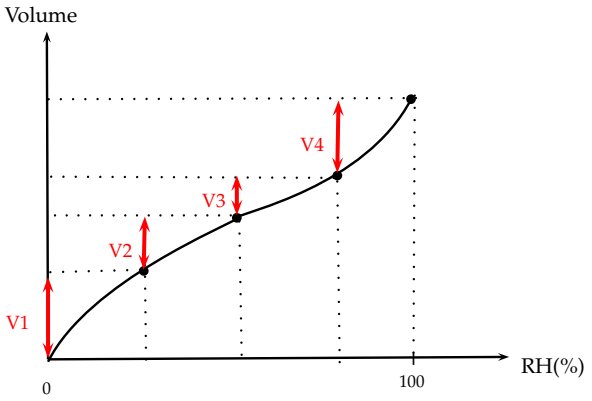

FIGURE 4.15: Schematic wetting isotherm obtained from numerical simulations

It is assumed that during wetting pores are filled by the liquid in the order of increasing pore radius (as predicted by the Kelvin-Laplace equation (4.2)), while on desorption the dimension of the pore necks (narrowest parts of the pore structure) controls the drying of pores. This phenomenon has been a subject of intense research [83, 84] and it was shown that it strongly depends on particular details of the pore geometry.

Baroghel Bouny [19, 87] explains that hysteresis is present between 3% and 100% relative humidity on various kind of cement-based materials and depends to the difference between the mechanism of condensation and evaporation which is related to the shape of pores in the liquid-vapour interface.

A simple figure representing different forms of pores is shown in order to detail the ink-bottle effect. Fig. 4.16 shows different arrangements of pores in porous media. A few pores may look like Fig. 4.16 (a) which has a uniform cross section and therefore fills or empties at a definite relative humidity according as the pressure is increased or decreased. Others may be more like Fig. 4.16 (b) or (c) in which the openings to the vapour phase are of different dimensions and initial and completed filling correspond to different relative humidities.

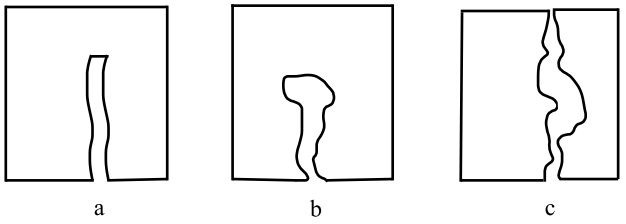

FIGURE 4.16: Different pore forms in a porous media

In general, pores may be represented as Fig. 4.16 (c), where the essential feature is that larger cavities are accessible only through smaller channels or orifices. In this kind of pore types as the relative humidity of a vapour is gradually increased, condensation of liquid begins at the narrowest cross section and extends to wider cross sections only as the relative humidity is increased, until when the vapour is sufficiently nearly saturated and the pore is completely filled. In general, with subsequent diminution of relative humidity, no evaporation occurs from a particular pore until the relative humidity has fallen to the value corresponding to the largest orifice or passage leading to the larger enclosed cavities. Since the size of the largest orifice leading to any particular cavity is randomly determined and since this principle holds for every enlargement in each of the numerous pores, the curve representing the amount of liquid retained during desorption lies above that for progressive sorption and this hysteresis is due to the mechanism here detailed.

In experimental sorption isotherm, at 100% relative humidity, the porous network conditions return to the initial conditions, while in numerical simulation even at 100% relative humidity the porous network are not fully saturated. Because the numerical modelling simulate the porous network state instantly after the relative humidity changes. Although the experimental isotherm usually depicts the long term state of materials. If the influence of long term phenomena like diffusion adds to numerical simulation, completely saturated material is attained at 100% relative humidity.

Numerical isotherms presented in this study are instantly sorption-desorption isotherms. From the before mentioned affiliated phenomenon to the difference between the pathway of these two curves, one can deduce that the difference between them at 100% relative humidity corresponds to ink-bottle pores.

4.4.1 Diffusion

As mentioned earlier, there is indication that some pores surrounded by the cement paste are ink-bottle pores. These pores are connected outwards through a narrower neck. When the materials behaviour is simulated in short term and only the instantly phenomena are considered

during wetting process, ink-bottle pores remain empty at 100% relative humidity. However, experimental results are always obtained after achieving equilibrium in long term. Thus, the long term phenomena could be added to the numerical simulations in order to have more similar numerical results to experimental ones. Diffusion is one of the long term phenomena and it is a key parameter controlling the progress of saturation occurring in porous materials.

During wetting process the water molecules are adsorbed on pores wall and consequently the small pores are firstly filled. The presence of water in the neck of pores causes the diffusion of water molecules into the ink-bottle pores, so that they can be filled over time. The pathway pores are connected outwards and they could be fed by the ambient relative humidity.

The required time for achieving certain relative humidity in a pore with length L could be obtained by equation (4.6), where D is diffusion coefficient of water in air which is considered $2 \times 10^{-10} m^2/s$ in the calculation. As shown in Fig. 4.17, in this equation the ink-bottle pore has the same diameter all long and is supposed equal to the gate pore diameter. It should be mentioned that this technique is only valid for high saturation degrees.

$$\frac{P_v}{P_{vsat}} = RH \approx 1 - \frac{4}{\pi} sin\left(\frac{\pi}{2}\frac{x}{L}\right) exp\left(-\frac{\pi^2}{4}\frac{Dt}{L^2}\right) \qquad (t \to +\infty) \tag{4.5}$$

$$x = L \quad RH \approx 1 - \frac{4}{\pi} exp\left(-\frac{\pi^2}{4}\frac{Dt}{L^2}\right) \qquad (t \to +\infty) \tag{4.6}$$

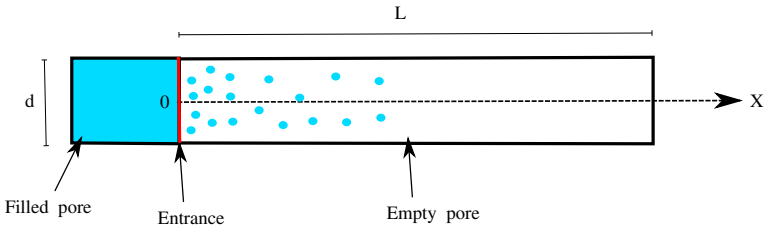

FIGURE 4.17: sketch of diffusion in a pore with diameter d and length L

In order to consider the diffusion phenomenon in ink-bottle pores where, the diameter of empty pore is bigger than the pathway (Fig. 4.18), it is supposed that the empty pore is replaced by several parallel pores with the same size of pathway and the diffusion time is multiplied to the number of parallel pores. Regarding all these simplifications, the obtained results by this technique gives an approximation of real values.

This technique is applied on the generated porous network to have the saturation degree over the time and to estimate required time to have fully saturated material in wetting process. The obtained results are illustrated in section 4.5.1.

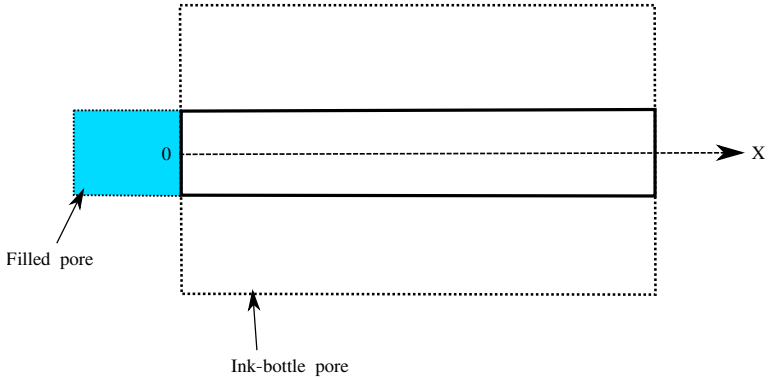

FIGURE 4.18: sketch of diffusion in ink-bottle pore

4.5 Numerical examples

4.5.1 Numerical isotherm for 2D porous network

In section 2.3.1 several morphological models of the porous network (MAT1, MAT2, MAT3 and MAT4) were presented in 2D, and in section 2.3.2.2 their pore distribution were shown. In section 4.2 and 4.3, procedures to simulate sorption and desorption isotherm were expressed. Afterwards, these morpho-mathematical operations and all numerical procedures were applied on morphological models.

In order to simulate desorption isotherm, drained volumes at each relative humidity level were calculated. Then during wetting, filled volume up to each relative humidity were determined and finally the variation of water saturation degree in terms of relative humidity was evaluated for different morphological models. Fig. 4.19 illustrates the numerically obtained isotherm for MAT1. The first curve in black presents the desorption process of the porous network from saturated state at 100% relative humidity to dried material at 0%. The other curve in red shows saturation degree progression in terms of relative humidity in wetting. The hysteresis between these two curves is significant.

The hysteresis between sorption and desorption isotherm depicts that ink-bottle pores have been simulated in the morphological model. This considerable difference could be justified by the fact that the only considered factor acting on sorption-desorption isotherm was capillarity which is instantly acting on the numerically created porous network.

To confirm this idea, another morphological modelling (MAT2) was considered which consists of two Random Fields in a domain of $1\mu m$. The first Random Field was generated with a small correlation length ($0.003\mu m$) and the second one with a big correlation length ($0.05\mu m$). Their volume fractions were equal and union of these two excursion sets was obtained regarding equations in section 2.2.5. Fig. 4.20 illustrates the porous network. In this figure the blue parts represent pores and the gray parts represent matrix. Fig. 4.21 shows the pore distribution and cumulative pore volume curves.

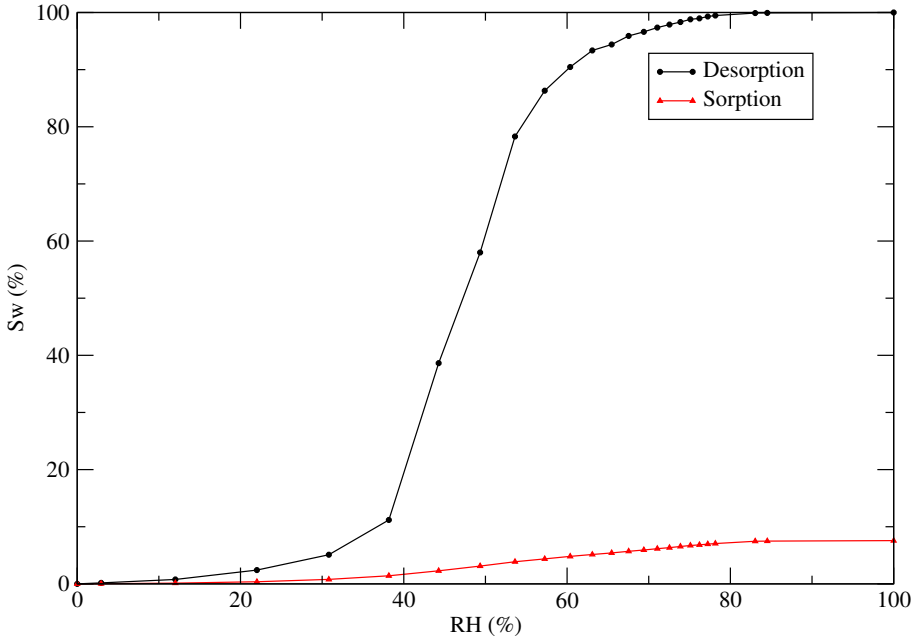

FIGURE 4.19: Sorption-desorption isotherm correspond to 2D porous network (MAT1)

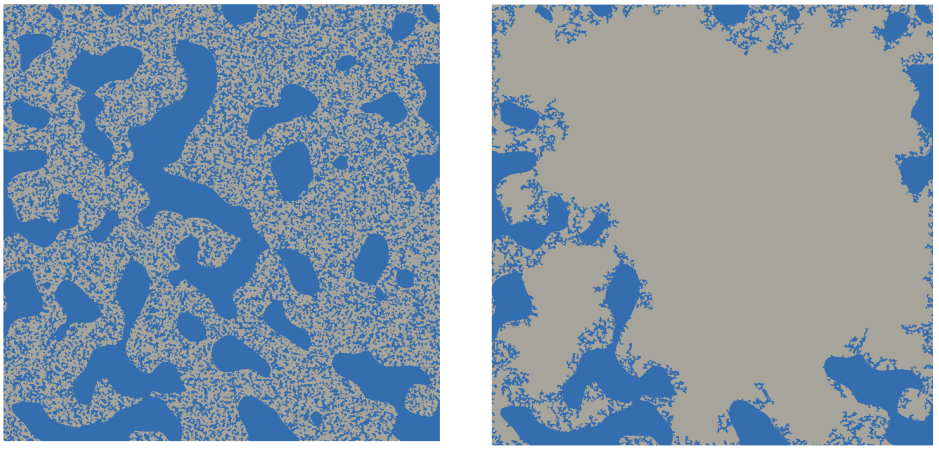

FIGURE 4.20: Porous network (MAT2) in left and connected pores outwards in right

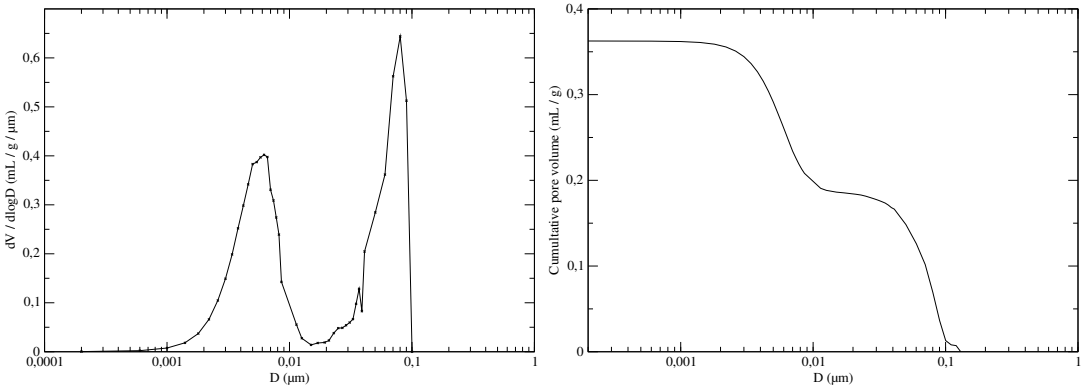

FIGURE 4.21: Pore distribution and cumulative pore volume curve of a 2D porous network (MAT2)

Looking at cumulative pore volume curve, it is observed that the volume of large pores is less than $0.2mL/g$. In the next step, morpho-mathematical operations must be applied on the numerical porous network to obtain sorption-desorption isotherm. Fig. 4.22 and Fig. 4.23 represent porous network at different relative humidities during drying and wetting. Black parts denote the matrix and blue parts are pores filled with water and gray parts indicate empty pores. Fig. 4.24 shows the obtained isotherm, and the volume of ink-bottle pores is $0.06mL/g$ based on the numerical isotherm. This value is less than the volume of large pores in the network, thus it can be validated that the difference between two curves in isotherm corresponds to ink-bottle pores.

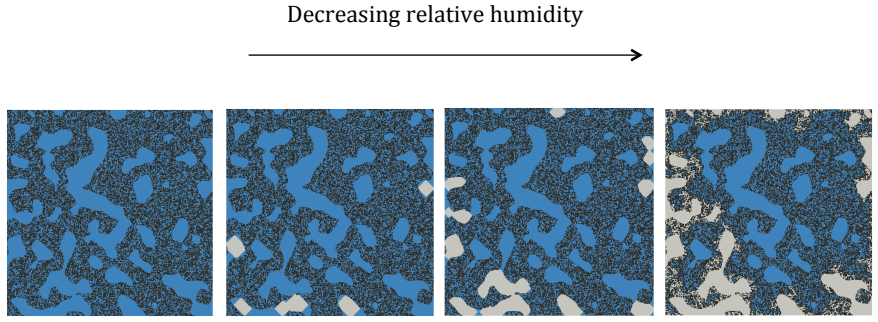

FIGURE 4.22: Drained volume during desorption in a 2D porous network (MAT2)

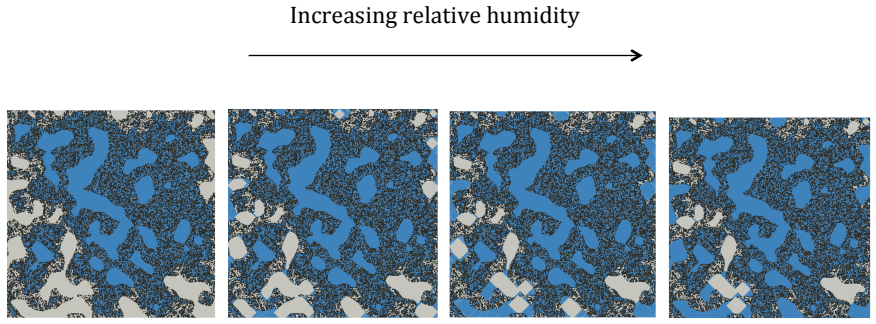

FIGURE 4.23: Filled volume during sorption in a 2D porous network (MAT2)

In the following, the numerical simulations are performed for MAT3 and MAT4 which are the morphological models of porous network consists of several Random Fields. In MAT3 the same volume fraction is considered for pores of different sizes. Fig. 4.25 and Fig. 4.26 respectively illustrate drained volume during desorption and filled volume during wetting for MAT3. Black, blue and gray parts represent respectively the matrix, filled pores and drained pores. In Fig. 4.26, the ink-bottle pores which remain empty at totally dried state, are obvious. The numerical isotherm is also shown in Fig. 4.27. Contrary to another cases, the obtained hysteresis (Fig. 4.28) for this morphological model is not considerable. In this porous network (MAT3) the volume fraction of pores with different average sizes was considered equal, and it avoids creating large pores behind small pores, consequently the isotherm hysteresis becomes less pronounced.

The numerical simulation was also performed on another 2D morphological model (MAT4). In this porous network pore distribution was inspired from cement paste, but the porosity was increased in order to have a connected morphology. The porous network at different relative

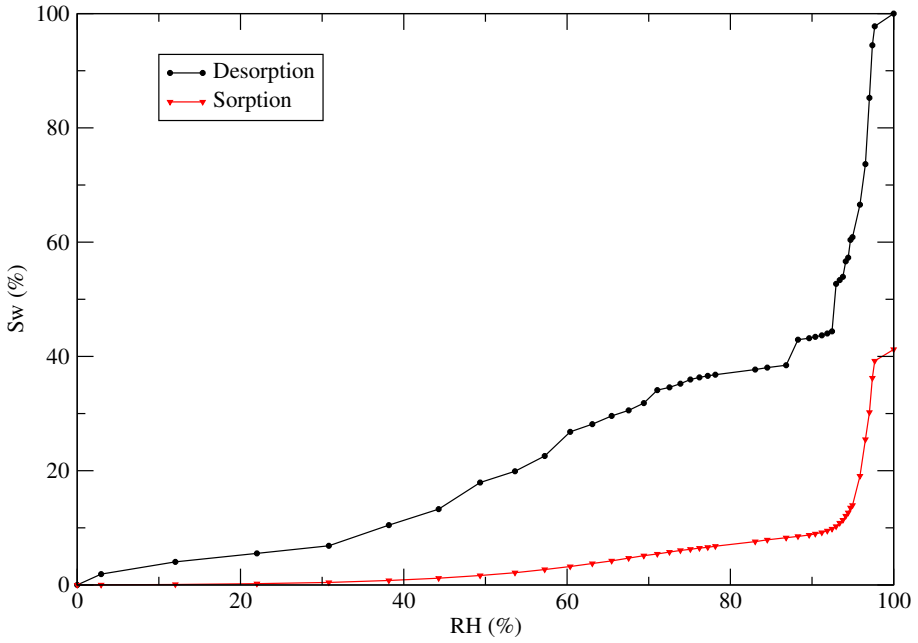

FIGURE 4.24: Numerical isotherm corresponding to a 2D porous network (MAT2)

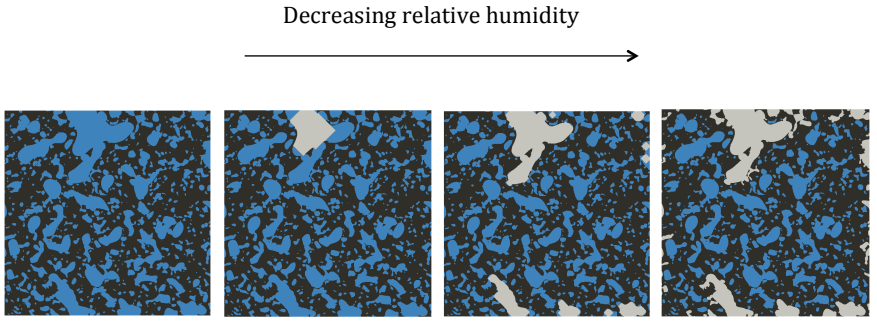

FIGURE 4.25: Drained volume during desorption in a 2D porous network (MAT3)

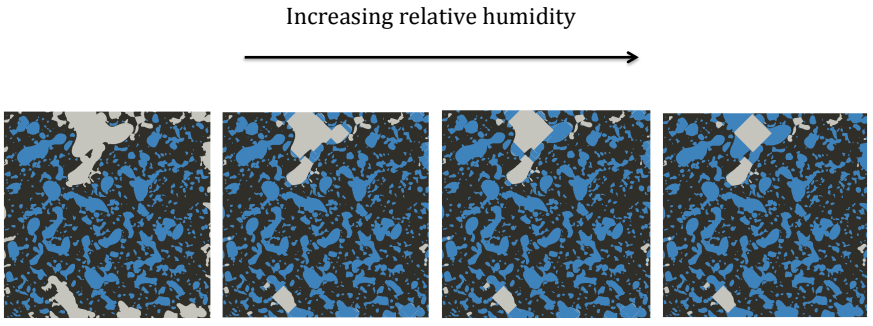

FIGURE 4.26: Filled volume during sorption in a 2D porous network (MAT3)

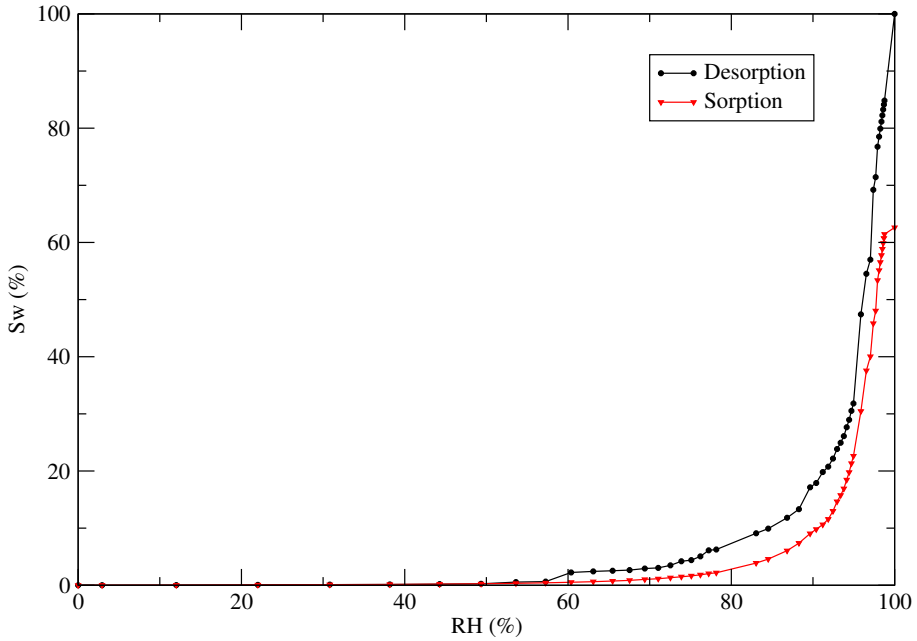

FIGURE 4.27: Sorption-desorption isotherm correspond to 2D porous network (MAT3)

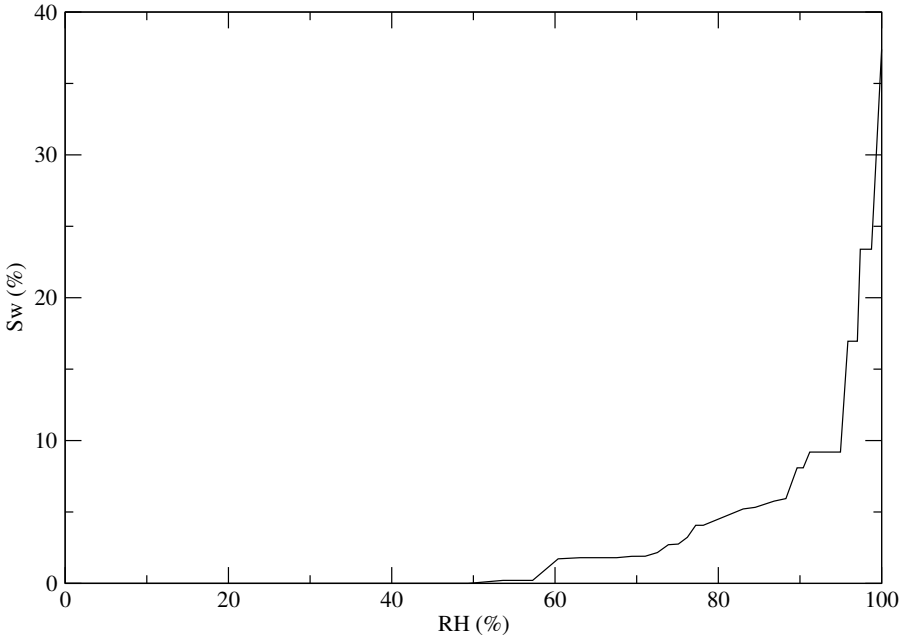

FIGURE 4.28: Hysteresis correspond to 2D porous network (MAT3)

humidities during desorption and sorption, and finally the numerical isotherm are respectively illustrated in Fig. 4.29, Fig. 4.30 and Fig. 4.31.

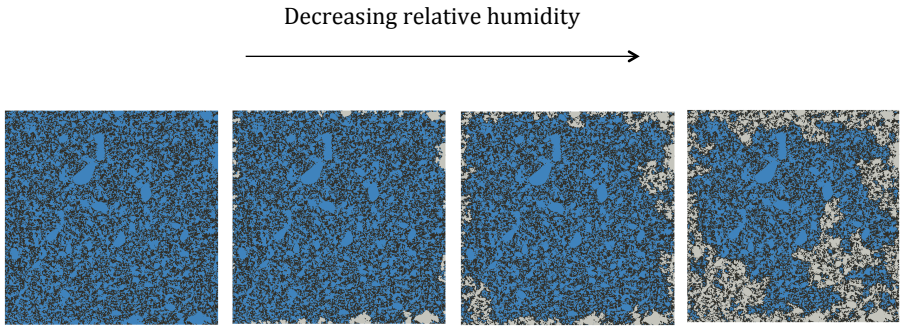

FIGURE 4.29: Drained volume during desorption in a 2D porous network (MAT4)

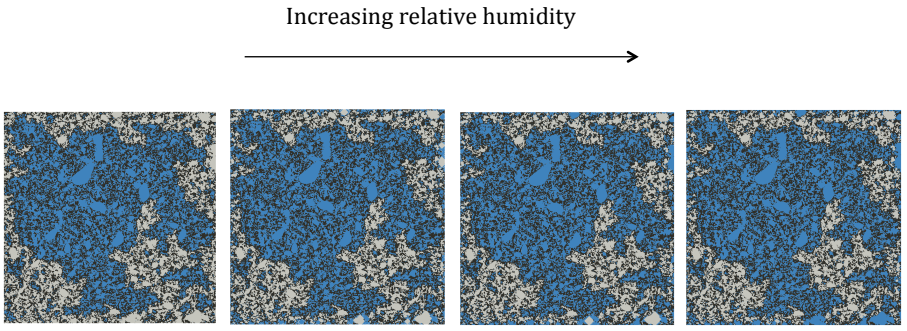

FIGURE 4.30: Filled volume during sorption in a 2D porous network (MAT4)

It was mentioned previously that, this numerical method simulates hydric behaviour of cement paste due to relative humidity changes by taking into account the capillarity. Consequently, all the ink-bottle pores remain drained and an important hysteresis was obtained in numerical simulations. Comparing the volume of ink-bottle pores at the totally dried state which is illustrated in Fig. 4.23, Fig. 4.26, Fig. 4.30 for different morphological models, justifies the variety of numerical hysteresis in different isotherms. However, if other physical phenomena such as diffusion and permeation were considered, the sorption isotherm would be moved upward and it would present less hysteresis effect.

The mentioned technique in section 4.4.1 in order to simulate diffusion in ink-bottle pores was applied on the porous network of MAT4. The average volume and average size of ink-bottle pores at 100% relative humidity was calculated. All ink-bottle pores were replaced by a single pore same as the sketch shown in Fig. 4.18. The volume and size of this single pore is equal to the average volume and the average size of ink-bottle pores. The required time to attain different saturation degrees were obtained and the results are illustrated in Fig. 4.32. It should be noted that, the considered technique is only valid for high saturation degrees, thus, the diffusion phenomenon was studied in the saturation degree range of 80% to 95%. Regarding the simplifying hypothesis in this technique, the obtained results are approximative values.

In order to have complete sorption isotherm considering diffusion, the volume of ink-bottle pores and the evaluation of saturation degree at different relative humidities should be studied.

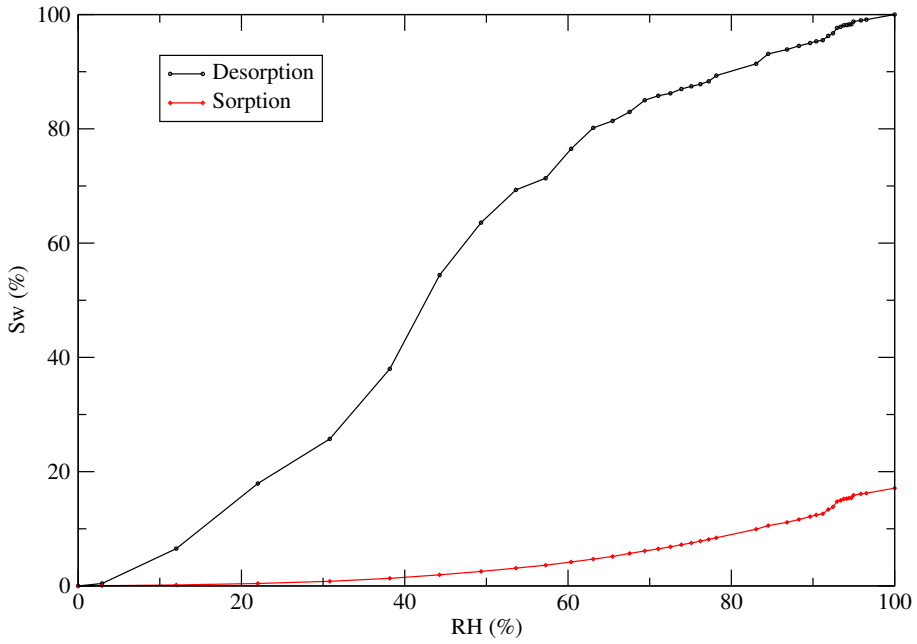

FIGURE 4.31: Sorption-desorption isotherm correspond to 2D porous network (MAT4)

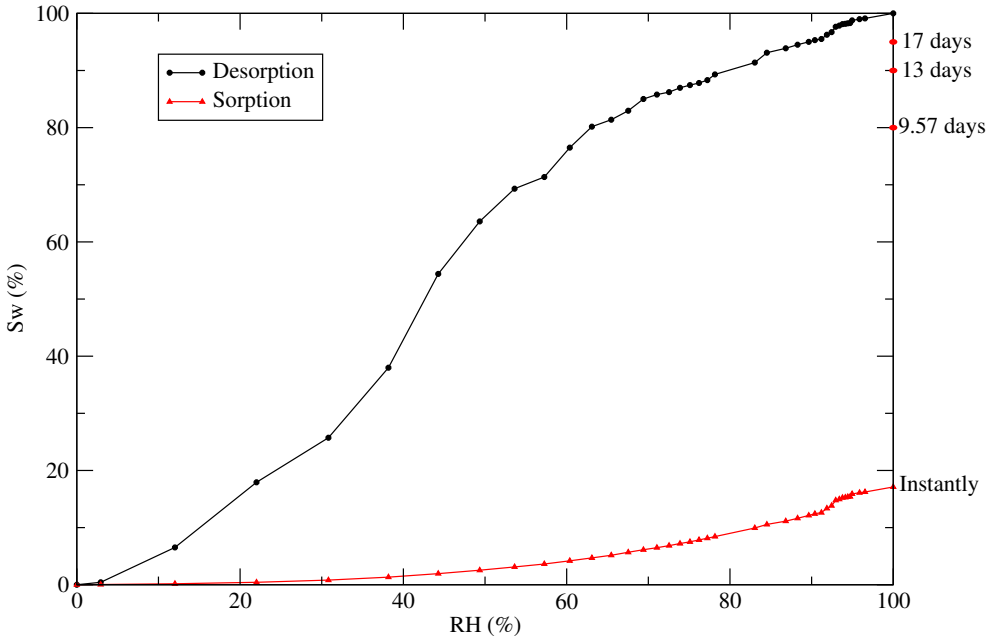

FIGURE 4.32: Diffusion effect on isotherm correspond to 2D porous network (MAT4)

4.5.2 Numerical isotherm of cement paste (3D porous network)

The proposed technique to simulate sorption-desorption isotherm could also be applied on the 3D generated porous networks of section 3.3 (MAT5 and MAT6). Drained or filled volume of Morphological models representing cement paste was obtained and afterwards the saturation degrees were calculated at different relative humidity levels. Fig. 4.33 was obtained as the numerical sorption-desorption isotherm of MAT6. This time the hysteresis between the two curves is well described. This hysteresis clarifies that ink-bottle pores were also well modelled in the 3D morphology.

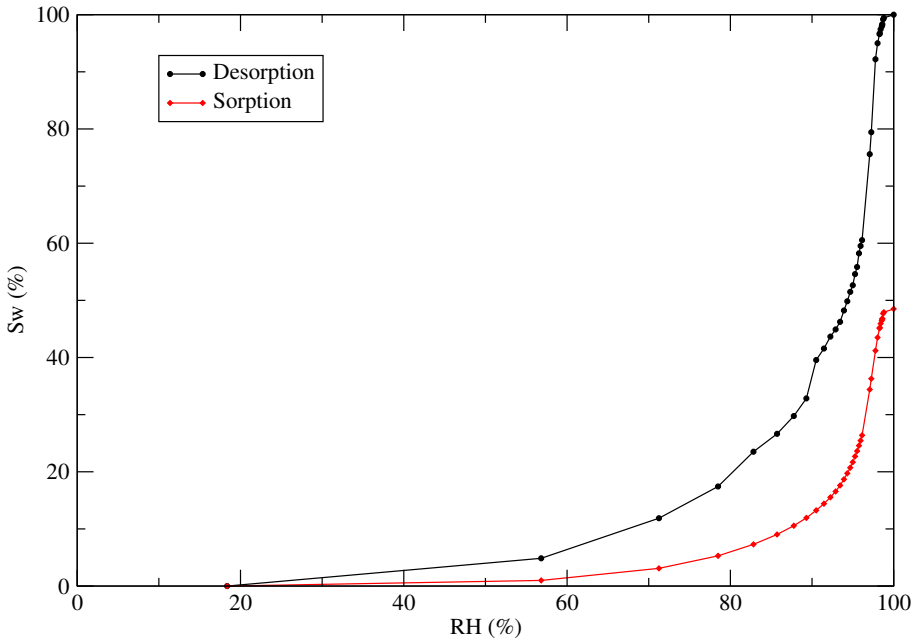

FIGURE 4.33: Numerical sorption-desorption isotherm for morphological model of cement paste with $W/C = 0.5$ (MAT6)

The 3D morphological models of cement paste were previously validated by comparing the experimental and numerical pore distributions. Now for the validations, it is time to compare the simulated sorption-desorption isotherm with the experimental one. Fig. 4.34 and Fig. 4.35 illustrate this comparison for both MAT5 and MAT6.

The numerical isotherms, in contrast to experimental ones, show a considerable shoot at high relative humidities. This shoot depicts that there are a lot of large pores in the morphology which are drained immediately at high relative humidities. Since the pores distributions of the numerical porous networks were already compared with the experimental ones and enough similarity was validated, the difference between the numerical and experimental isotherms could come from the accuracy of morpho-mathematical operations and especially geodesic reconstruction in 3D due to mesh finesse.

In the 2D isotherm of MAT4 (Fig. 4.31) there is not a significant shoot at high relative humidities and pores are drained and filled progressively. This is while in 2D mesh there are 5000 point on each side of the square with the size of $1\mu m$ and it gives $0.0002\mu m$ as the voxel size. Hence, in geodesic reconstruction, two pores are considered connected to each other when the distance

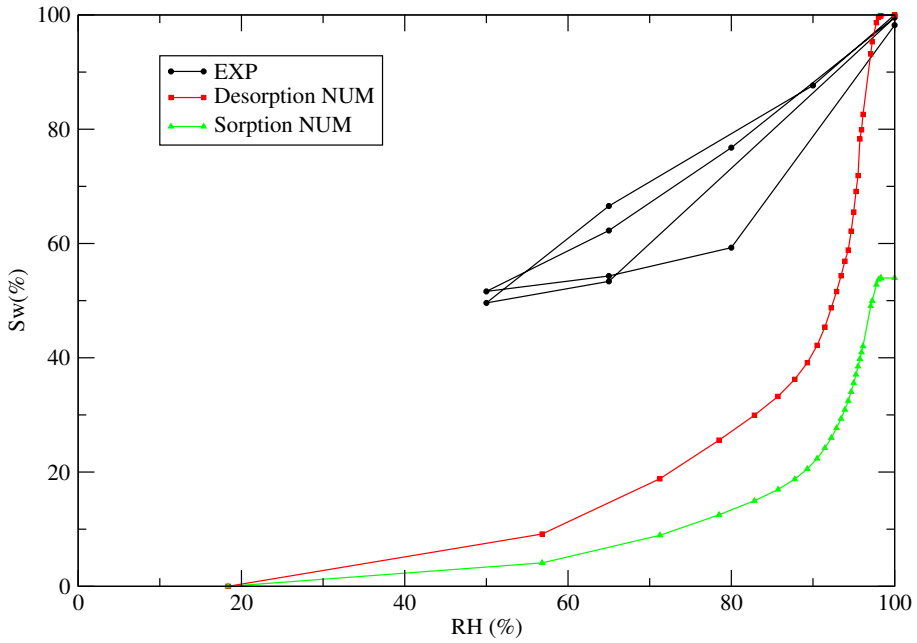

FIGURE 4.34: Numerical and experimental sorption-desorption isotherm for cement paste with $W/C = 0.8$ (MAT5)

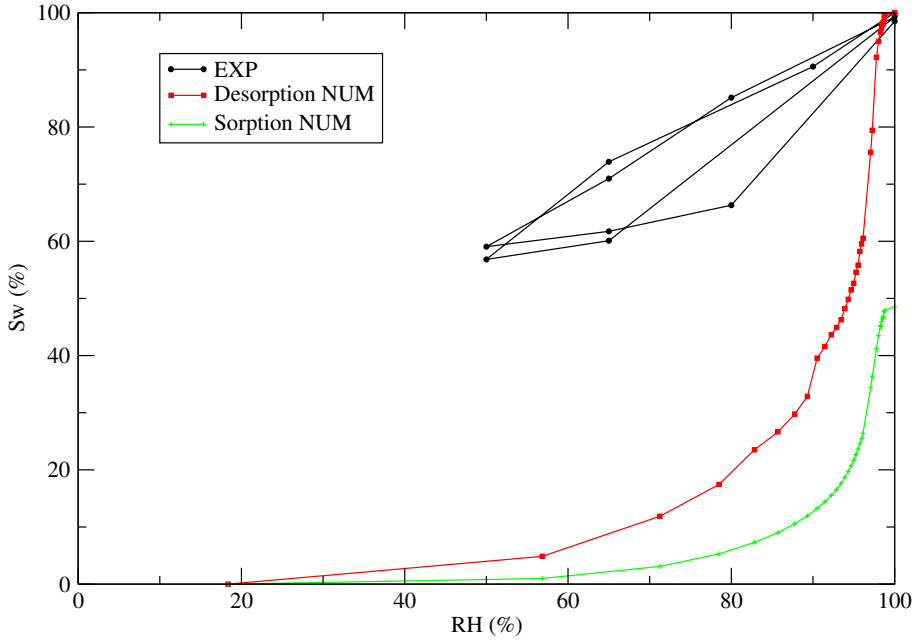

FIGURE 4.35: Numerical and experimental sorption-desorption isotherm for cement paste with $W/C = 0.5$ (MAT6)

between them is less than $0.0002\mu m$. In 3D mesh, because of numerical limitations, 800 points are considered on each side of the cube with the size of $1\mu m$. Accordingly the voxel size is $0.00125\mu m$ and it results in considering two pores connected to each other if their distance is less than $0.00125\mu m$. Hence, the accuracy to detect connected pores in 2D simulation is about 6 times larger than the accuracy in 3D simulation. In other words, in 3D simulation it is possible to consider two pores connected to each other while they are not really connected, just their distance is less than $0.00125\mu m$. For the moment, with the available tools, it is not possible to have a finer mesh in 3D. But regarding the 2D results, in the future, where more powerful tools are upcoming, the simulated isotherm in 3D will get closer to the experimental one.

Regardless to the lack of accuracy in 3D simulation, it was tried to attain more similar numerical isotherms to experimental ones by applying some modifications on morphological model. As mentioned before, in the obtained desorption isotherm the saturation degree substantially decreases at high relative humidities which is due to the presence of large pores connected outwards. Thus, the morphological model could be modified by limiting volume fraction of large pores. For this purpose, Random Fields with large correlation lengths ($L_c = 0.12$ and $0.07\mu m$) were excluded from morphological model and network 2 was generated. Moreover, network 3 was also created adding another Random Field with small correlation length ($L_c = 0.003\mu m$) to network 2. By adding small pores to porous network, the outwards connection path of large pores passes through small pores and as a result a part of large pores becomes ink-bottle pores. Consequently, large pores could not be drained immediately at high relative humidities and the desorption isotherm decreases gradually. Fig. 4.36 illustrates the comparison between numerical desorption isotherms for network 1 (MAT6) , network 2 consists of six Random Fields ($L_c = 0.005$, 0.008, 0.011, 0.02, 0.03, $0.05\mu m$) and network 3 consists of seven Random Fields ($L_c = 0.003$, 0.005, 0.008, 0.011, 0.02, 0.03, $0.05\mu m$).

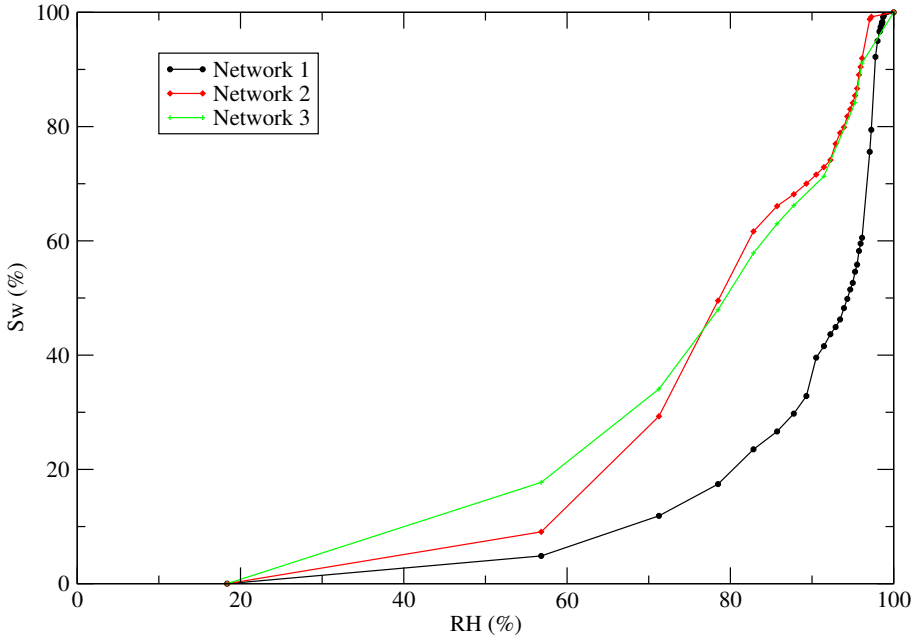

FIGURE 4.36: Numerical desorption isotherm for cement paste with $W/C = 0.5$ (MAT6) by modifying morphological model

According to desorption isotherms obtained for modified porous networks, it could be deduced that numerical results are very sensitive to changes in morphological model. Modifying geometrical parameters of morphological model is one of the key factors to control the obtained results and leads to more realistic results.

4.6 Adsorption layer

In a hydrating water/cement system, water can be classified into three different forms, chemically bound water, physically bound water and capillary water which were detailed in section 1.2.3 [20]. Capillary water is mainly found in capillary pores. There is no attraction force between the solid surface and this form of water. Physically bound water is adsorbed on the pores walls and its amount depends on the relative humidity of the porous system.

The thickness of the adsorption layer goes from 1 monomolecular water layer (about 2.76$\mathring{A}$) at 20% relative humidity to about 5 monomolecular layers at 100% relative humidity as shown in Fig. 4.37.

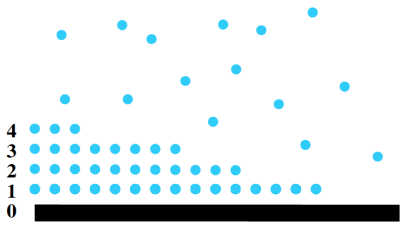

FIGURE 4.37: Water adsorption layers at different relative humidities

Since relative humidity increases, the thickness of adsorption water also increases until it reaches about 13$\mathring{A}$ in saturated state. Fig. 4.38 illustrates the value of adsorption thickness in terms of relative humidity.

Adsorbed water can make a significant contribution to the saturation for micropores. Hence, the adsorption must be taken into account for the small pores in the range of nanometer. When the capillary pores are drained gradually, an adsorbed water layer remains on the surface of pore walls under the action of the bonding forces. Equation (4.7) could be used to find the thickness of adsorbed water layer (δ) at different relative humidities [89–91]. For the relative humidity values between 0 and 1, the thickness of adsorbed water layer in nm becomes δ.

$$\delta = 0.395 - 0.189ln(-ln(RH)) \tag{4.7}$$

Hence, in the presented numerical model, the thickness of adsorbed water layer and accordingly the volume of adsorbed water could be determined for different relative humidities.

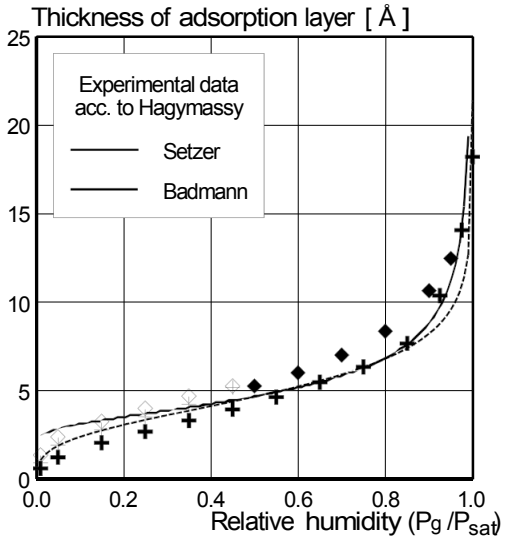

FIGURE 4.38: Thickness of adsorption layer as a function of relative humidity [88]

When the relative humidity decreases, pores are drained gradually from the largest to smallest. At the same time, the adsorbed water layer gradually decreases. On the contrary, when relative humidity increases in wetting, the adsorbed water layer thickness increases.

Fig. 4.39 and Fig. 4.40 illustrate the porous network states respectively in desorption and wetting considering adsorption effect.

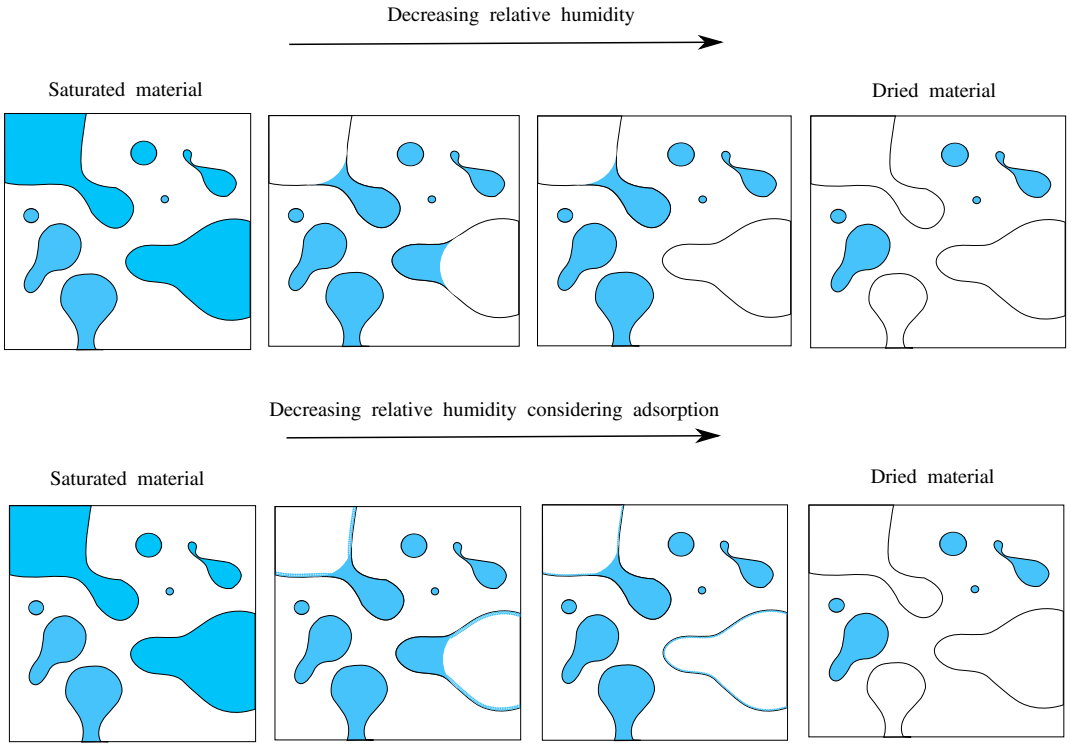

FIGURE 4.39: Adsorption effect on porous network state in desorption

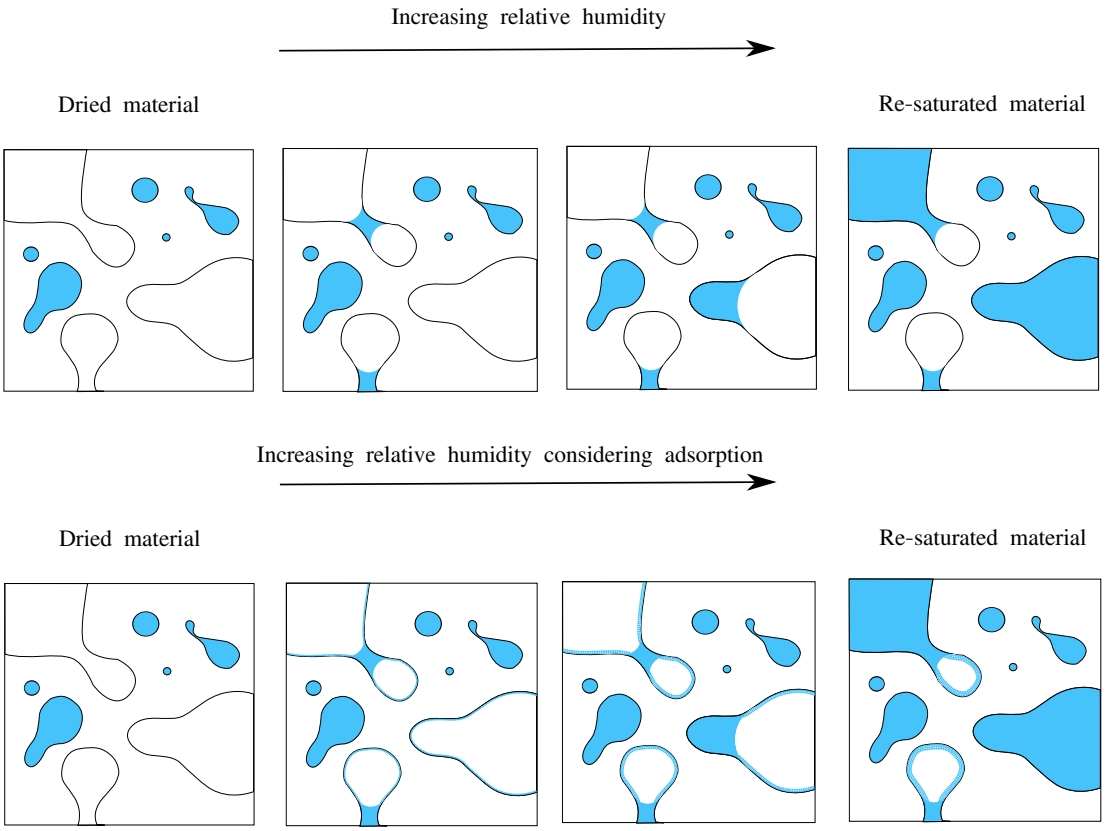

FIGURE 4.40: Adsorption layer effect on porous network state in sorption

The formerly presented sorption-desorption isotherms were drawn without considering adsorption layer effect. Since the volume of adsorbed water on the pores walls could affect the water contents, Fig. 4.41 illustrates the sorption-desorption isotherm considering adsorption layer effect for MAT4.

As depicted in Fig. 4.41, by considering adsorbed layer volume, the water content is generally increased in sorption and desorption isotherm. But in some cases, it has the converse influence as indicated in the sorption isotherm for high relative humidities. This anomaly occurs because the connectivity of pores is influenced by considering adsorption layer. For example adsorbed layer on the small pores walls could block the access to larger back pores. Consequently, more ink-bottle pores are appeared and water content decreases.

4.7 Sensitivity evolution of sorption-desorption isotherm

The sorption-desorption isotherms illustrated in previous section were obtained by applying morpho-mathematical operations on a generated morphology. The result of morpho-mathematical operations and consequently the form of sorption-desorption isotherm depends on the morphology itself and parameters which could affect it. Two groups of parameters could have influence on obtained isotherm. The first group is the geometrical parameters, which have

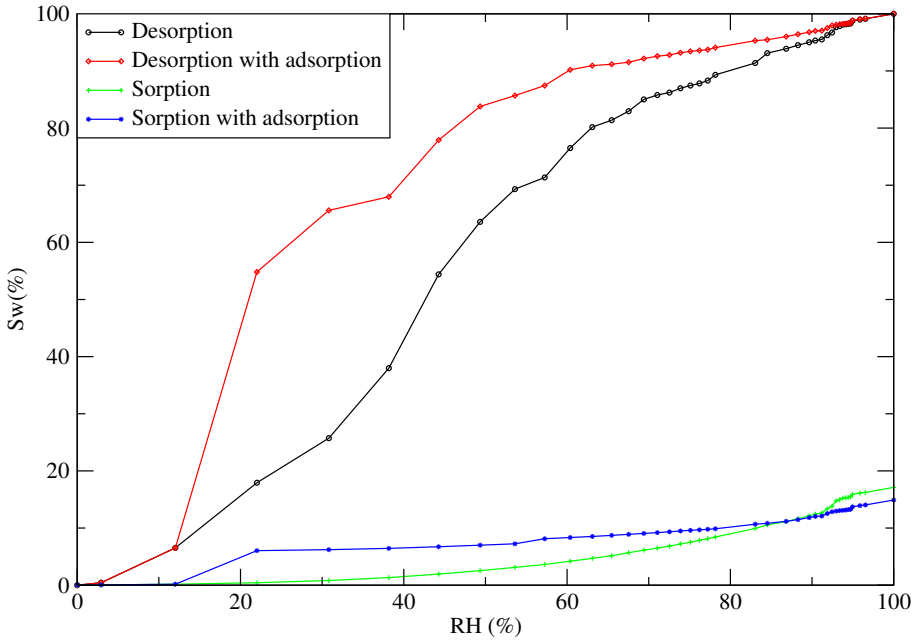

FIGURE 4.41: Sorption-desorption isotherm considering adsorption layer effect for MAT4

effect on the morphological model and therefore on obtained isotherm. The other type is the physical parameters like temperature which have influence on calculated isotherm without having effect on morphological model. In the following, sensitivity of sorption-desorption isotherm is evaluated to the both of these parameters.

4.7.1 Sensitivity evolution of isotherm to geometrical parameters

One of the geometrical parameters which could have influence on obtained isotherm is the correlation length. In section 2.4 the sensitivity of pore distributions to the correlation length was studied in the content of a 2D generated porous network (MAT4). In this section the sensitivity of sorption-desorption isotherm to this parameter is assessed. For this purpose the numerical sorption-desorption isotherm of MAT4 is re-calculated by removing excursion sets with different correlation lengths in the union of Random Fields.

Fig. 4.42 shows the calculated sorption-desorption isotherm corresponding to different morphologies and represents the important influence of correlation lengths value on the form of curves and the hysteresis between them. For example when the excursion set with the smallest correlation length $L_c = 0.003\mu m$ was removed, the hysteresis between the two curves obviously becomes less important. Therefore, it could be concluded that due to the existence of small pores, the number of ink-bottle pores increases.

The advantage of knowing role of geometrical parameters like correlation lengths, and their influence on porous network and isotherm is that they could be used in order to achieve more realistic porous networks. Therefore, more similar numerical results can be attained compared to experimental ones.

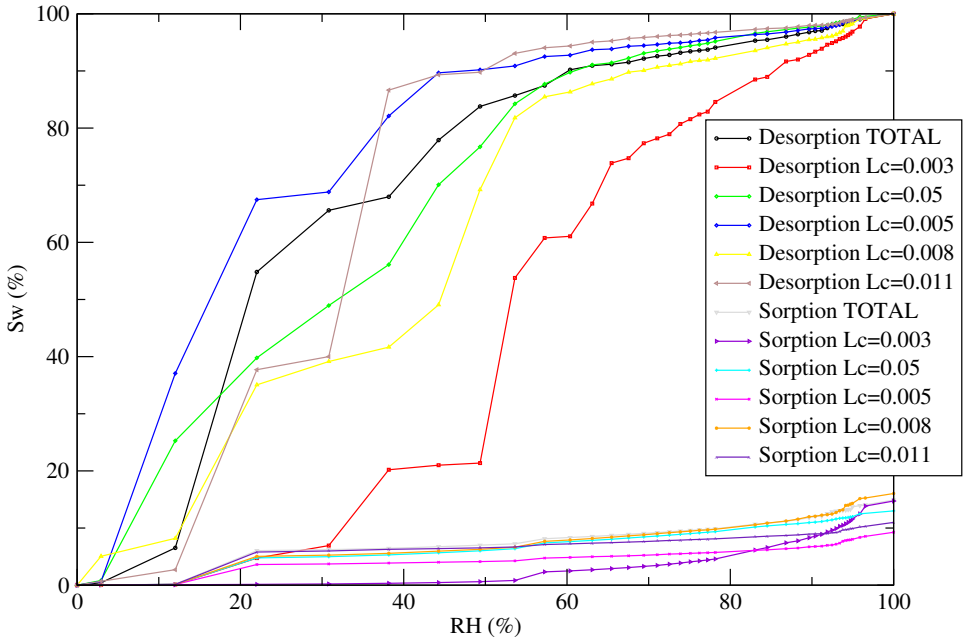

FIGURE 4.42: Influence of elimination of some Random Fields on sorption-desorption isotherm of MAT4

4.7.2 Sensitivity evolution of isotherm to physical parameters

The sensitivity of numerical isotherm could also be studied due to effective parameters on the physical phenomena. As mentioned in section 4.2.2, in order to find saturated or drained pores at each relative humidity, capillary radius should be calculated based on Kelvin-Laplace law (esuation 4.2). One of the parameters which could have influence on the obtained capillary pore radius for each relative humidity is the temperature. For example during drying, at a certain relative humidity, when temperature increases, smaller pores are drained. Fig. 4.43 shows the obtained sorption-desorption isotherm for MAT4 at $20°C, 50°C$ and $80°C$. The influence of temperature on isotherm was experimentally studied in the thesis of Brue [18] and the results were illustrated in section 1.4.1 (Fig. 1.11).

Once again the numerical results could not be compared with experimental ones, because the experimental curves correspond to material state in long term but in numerical simulations the porous network was studied at each state using instantly acting phenomenon. However, both of numerical and experimental results show the same changing behaviour by increasing temperature.

In the simulation of long term phenomenon like diffusion, diffusion coefficient of water vapour in air also depends on temperature and as it was illustrated in equation (4.6), when diffusion coefficient varies, the required time to achieve a certain relative humidity also changes. Therefore, it could be deduced that the experimental result express the sum of these effects.

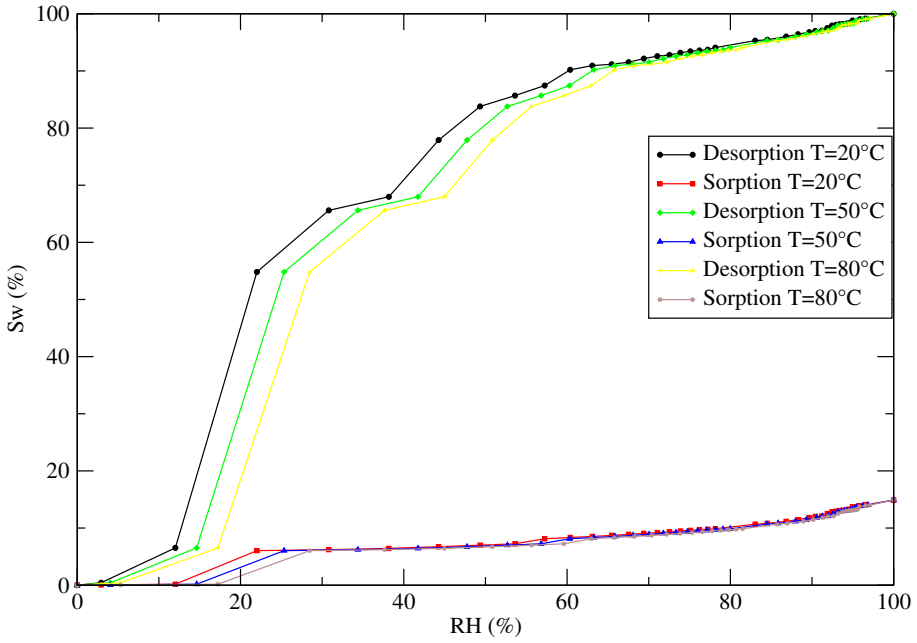

FIGURE 4.43: Influence of Temperature on sorption-desorption isotherm of MAT4

4.8 Conclusions

Studying the hydric behaviour of cement paste and simulation of sorption-desorption isotherm was mentioned in this chapter and the following conclusions are made:

- **It is possible to simulate hydric behaviour of cement paste applying an image filtering associated with physical phenomena on the morphological model.** For this purpose Kelvin-Laplace law and the adsorption layer could be linked to structuring element size and the connectivity of pores to outwards by performing geodesic reconstruction.
- An image filtering associated to physical phenomena was applied on the numerical models on 2D and 3D .
- **In drying process, the advantage is that the physical phenomenon was well presented by image filtering and it is illustrated that the desorption isotherm is sensitive to morphological model.**
- The shortcomings of drying process are that:
  - There is not an accurate link between parameters and results and it is not possible to completely control the system.
  - There is an obvious difference between experimental and numerical results. Because the mercury intrusion test has some limitations to detect small pores. Thus, the morphological model lacks of small pores which have a major role in the drying and wetting process. Moreover, in the 3D simulation, smaller grid size is required.

- In wetting process, a considerable hysteresis is induced due to the considered physical phenomenon and the presence of ink-bottle pores. It could be observed that the obtained isotherm is more related to mercury intrusion than water sorption.
- **In order to simulate materials behaviour facing water, another physical phenomenon such as diffusion of water in air must be taken into account.**
- It was attempted to take into account a simplified diffusion of water into ink-bottle pores.
- The positive points of the proposed simulation are:
  - The simple physical phenomenon were considered and despite ignoring fluid transfer equations, the obtained results well represented hydric behaviour of nanoporous materials.
  - The influence of simple physical parameters such as temperature were taken into account.
  - The morphological modelling and isotherm are numerically linked together.
- However, there are some negative points in the proposed method such as:
  - It is complicated to control the numerical link between morphological modelling and isotherm.
  - All the associated phenomena were not taken into account in numerical simulations, and the considered phenomena were too much simplified.

Chapter 5

Dimensional variations due to hydro-mechanical coupling

Contents

5.1 Introduction

One of the most important issues to study the durability of cement-based structures is the prediction of their deformation. Indeed, they can be responsible of cracking, re-distribution of stresses and in extreme cases even cause the destruction of structures. The objective of this work is to develop numerical tools able to predict the mechanical behaviour of cement-based structures. Therefore, a hydro-mechanical model is developed by integrating the description of the drying phenomena and shrinkage.

In the past chapters, the structure of the porous network and effects of hydrical stress were studied and an application to cement paste was evaluated. The physical phenomena have been determined at the scale of a microstructure. The approach proposed in this chapter focuses on the hydro-mechanical coupling.

Water is present in various forms in the cement-based material within the porous network and it is in equilibrium with the solid matrix. Modifications due to drying or saturation of the specimen lead to dimensional variations in order to maintain the overall balance of the system. The shrinkage occurs during water exchange between the material and the environment. At different relative humidities, water flows outward from pores in order to be in equilibrium with the environmental conditions. Therefore, some parts of capillary network are not saturated with water, and a gaseous phase consisting of water vapour and air is placed there. The internal relative humidity (equilibrium between liquid and gas phase) decreases and meniscus is formed in contact surface of these two phases. Consequently it leads to capillary depressions and shrinkage of the materials.

In the continue, by decreasing relative humidity, the curvature radius of the meniscus decreases and adsorbed water on the pores wall drains. Therefore, different dimensional variation mechanisms may play an important role at a considered relative humidity [92].

In this chapter a numerical strategy, based on the spatial representation of the unsaturated state of materials at each relative humidity is proposed in order to estimate drying shrinkage. Of course, a complete framework to that aim would require a numerical simulation process. Here, we overcome this issue by using a very simple energy balance principle between micro and macroscale.

Various mechanisms related to dimensional variations, as well as shrinkage are shown in the following.

5.1.1 Dimensional variation mechanisms

The drying shrinkage depends on the liaison of water and solid in the materials. Therefore, water/solid interaction must be evaluated in order to study drying shrinkage mechanisms. Drainage of the free water contained in pores does not cause dimensional changes. Three main mechanisms are generally considered to explain the relationship between the saturation of the materials and the deformations observed in the absence of any other loading [43, 92, 93]. These mechanisms correspond to:

- Capillary pores water
- Adsorbed water
- Micropores water

The corresponding mechanisms are respectively:

- Shrinkage due to variation of capillary depression
- Shrinkage due to variation of surface energy
- Shrinkage due to variation of disjoining pressure

5.1.1.1 Shrinkage due to variation of capillary depression

The first mechanism involves the depression applied by the liquid phase within the materials. It can be generated by the capillary pressure. This phenomenon follows the Kelvin-Laplace law in which the value of capillary depression is related to relative humidity and the radius of cylindrical capillary pores. Equation and details were already discussed in chapter 4. This mechanism is considered active when the capillary water is continuous, usually for relative humidities higher than 40% [48]. When the material dries progressively, meniscus are created in capillary pores. By decreasing relative humidity, the meniscus radius of curvature decreases in order to maintain the balance between liquid water and gaseous phase. A decrease of the curvature radius and a capillary depression are created in the fluid as a consequence of water evaporation, and they cause a contraction in materials.

5.1.1.2 Shrinkage due to variation of surface energy

The second mechanism is based on surface tension (or surface energy), which may vary with gas adsorption. Increasing the value of this energy leads to a contraction of the material, explaining the observed shrinkage. This phenomenon occurs if the amount of absorbed water varies, and is therefore operative to relative humidities lower that 40% [49]. The solid phase of cement paste has a large surface area. Thus, a significant amount of adsorbed water is in interaction with solid surface. The surface energy of the system formed by the cement paste solid surface varies with the variation in the thickness of the adsorbed water which depends on relative humidity. When the relative humidity is less than 40%, the thickness of adsorbed water decreases, and accordingly surface tension between CSHs and the rest of adsorbed water molecules increases. Thus, the solid matrix contracts locally to compensate the variation of surface energy, and consequently it induces a shrinkage at the macroscopic scale. It is possible to define the linear swelling $\Delta l/l$ produced by adsorption of water on the solid surface by Bangham [49, 94, 95] equation (5.1):

$$\Delta l/l = A(\gamma_0 - \gamma) \tag{5.1}$$

Where γ_0 is the surface energy of the solid without adsorbed water, γ is surface energy of the solid with adsorbed water and A is a constant corresponding the material and its structure.

5.1.1.3 Shrinkage due to variation of disjoining pressure

On a flat surface five water molecules could be adsorbed at 100% relative humidity. The water molecule has a diameter of about 2.6$\mathring{A}$ which gives 13$\mathring{A}$ for the thickness of the adsorbed layers in saturated state. The pore diameter should then be greater than 26$\mathring{A}$ so that adsorption can freely occur. The free adsorption can not take place, when the adsorbent surfaces are too close. It is then called prevented adsorption zone. Fig. 5.1 shows adsorption in different parts of a pore with different diameters.

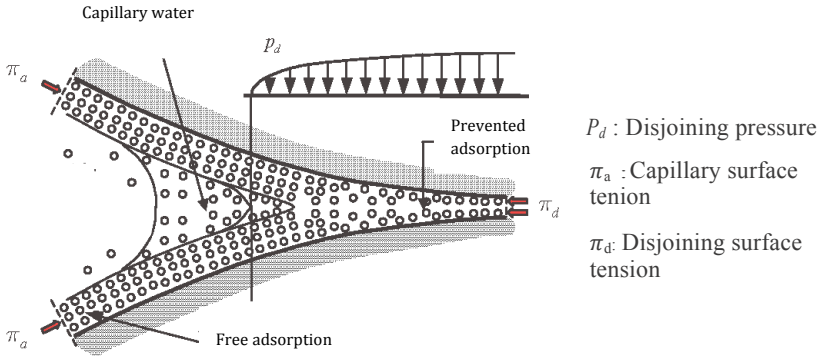

FIGURE 5.1: Disjoining pressure in prevented adsorption zone [96]

In these areas, water is strongly adsorbed under a pressure which is called disjunction pressure [96]. This pressure is opposed to the attractive forces between the particles of CSH which maintain the solid structure.

The third mechanism of drying shrinkage is linked to disjoining pressures. The water intrusion in inter-sheets zones creates repulsive forces among the layers of CSH, and attractive forces (van der Waals) between solid surfaces are reduced. The sum of these two effects is referred to disjoining pressure, which is resulted the dimensional variations in equilibrium of the system. The validity of this pressure as the origin of shrinkage, and the relative humidity range in which this mechanism should be considered active, is controversial. The disjoining pressure varies with relative humidity changes and accordingly the distance between solid surfaces changes. Thus the dimensional variation in terms of relative humidity could be obtained.

Different authors consider different operational relative humidity ranges for each mechanism. Table 5.2 shows different mechanisms according by authors.

5.2 Experimental protocol

Usually the value of shrinkage in experimental protocols is measured by generating a considerable hydraulic gradients within the material [17, 98]. In these techniques the value of

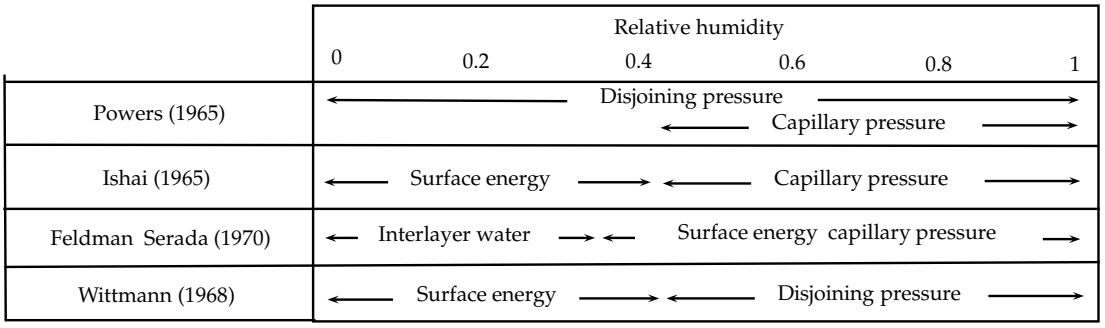

FIGURE 5.2: Different mechanisms of shrinkage [97]

shrinkage depends not only on the material behaviour but also on specimen geometry. Rougelot [1] proposed to perform drainage with low relative humidity intervals to limit structural effects, and therefore obtain results closer to the material behaviour. This technique has been used to desorption isotherm and is completed by shrinkage measurement.

The saturated state was provided by curing specimens under water. Relative humidity levels were imposed by placing the samples in climatic chamber. Their weight was regularly checked until reaching stable weight for a given relative humidity level. Two brass sheets were placed on two opposite surfaces of sample. The deformation measurement was then effected by measuring the length between these two sheets using a comparator with the resolution of 0.001 mm.

The reference length of the sample was the length L_0 measured in saturated state, and L_{RH} is the measured length at each relative humidity. The deformation at each relative humidity level, $\epsilon(RH)$ was determined by (5.2):

$$\epsilon(RH) = \frac{L_{RH} - L_0}{L_0} \tag{5.2}$$

At each relative humidity level, when the specimen is in equilibrium state, because of the homogeneity of drying, measured deformation in one direction is similar to the two other directions. Thus the volume deformation $\epsilon_v(RH)$ at each relative humidity level can be calculated by (5.3):

$$\epsilon_v(RH) = 3\epsilon(RH) \tag{5.3}$$

Fig. 5.3 shows the curve of deformation in terms of relative humidity for the studied material by Rougelot [1].

Three phases are generally observed in experimental curves. Despite the weight loss, deformations remain low in the first phase. This phase corresponds to drainage of water which is on the surface of specimen. Then a second phase, which includes a big part of the curve shows the evolution of shrinkage mainly due to capillary pressure variations induced by drying. A final phase where deformations are again low as the weight loss continues. Many effects are

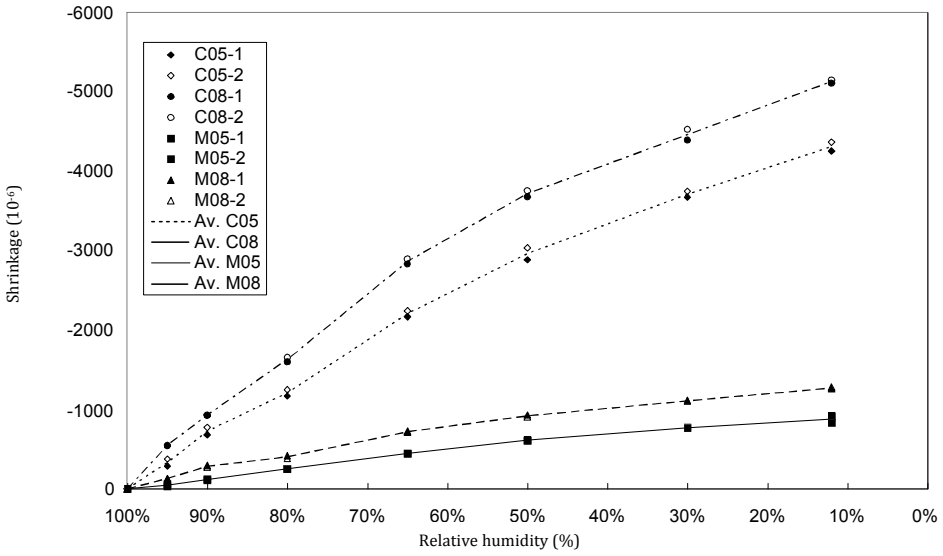

FIGURE 5.3: Measured deformation in terms of relative humidity ('M' for mortar, 'C' for cement paste, '05' for $W/C = 0.5$ and '08' for $W/C = 0.8$ [1]

proposed to explain this phenomenon, such as a non-linear behaviour under hydric stress [92] or an appearance of cracking which becomes dominant.

For $50\% - 100\%$ relative humidity, the linear relation between deformation and relative humidity was verified. However, by studying the curve more precisely, the deformation increases less rapidly at lower relative humidities. This effect can be attributed to the fact that, by decreasing relative humidity, the value of capillary depression increases but its application point decreases. This hypothesis could be verified using the numerical model of porous network that is discussed in section 5.3. The decrease of slope for the relative humidity below 50% could be due to micro cracking in the materials that is generated because of relatively high values of capillary pressures applied within the porous network.

5.3 Numerical modelling

Obtaining deformation curve as a function of relative humidity allows a better understanding of cement-based materials behaviour, and provides essential information in the study of durability. Experimental protocol is very time consuming, numerical models is therefore an important aspect in the prediction of shrinkage. In this section, the previously proposed models of porous network are used to simulate the mechanical behaviour of cement-based materials and to obtain the value of shrinkage for different relative humidities.

Numerical modelling of shrinkage is based on the capillary pressure and disjoining pressure mechanisms, which appear predominantly at the relative humidity range $50\% - 100\%$ (Table 5.2). The surface energy effects are neglected in this study. It is assumed that under the effect of capillary pressure and the disjoining pressure change (induced by drying), the solid skeleton

TABLE 5.1: Capillary pressure for different relative humidities for water at $T = 20°C$

RH (%)	12	22	38.16	57.2	60.38	71.05	83	90.4	93.39	100
$P_c(MPa)$	288.1	205.8	130.9	75.92	68.57	46.45	25.32	13.72	9.29	0

elastically deforms. Thus, the numerical value of deformation is obtained by elastic strain energy calculation at microscopic scale applying efforts on solid skeleton due to capillary pressure and variation of disjoining pressure. First of all the value of these efforts and their application points should be determined at different relative humidities.

5.3.1 Shrinkage due to capillary pressure

The drying shrinkage mechanism by capillary pressure can be explained using Kelvin-Laplace equation. Its details and necessary assumptions were discussed in section 4.2.2. The Kelvin equation expresses the balance between the liquid phase and gas phase. By choosing a particular reference state [43], capillary pressure is obtained by equation ((5.4)):

$$P_c = \frac{\rho_l RT}{M_l} ln(RH) \tag{5.4}$$

Where P_c is capillary pressure, ρ_l is density of water, T is temperature, R is perfect gas constant, RH is relative humidity and M_l is molar mass of water. Table 5.1 shows the capillary pressure for water at different relative humidities and $T = 20°C$.

In the porous network, capillary pressure is applied on pore walls where there is an interface between liquid and gas phases (water vapour or dry air). Because of the difference between liquid pressure and gas pressure, meniscus are created in pores which are called capillary pores. Fig. 5.4 shows a sketch representing capillary pore. The size of these capillary pores also depends on relative humidity and could be obtained by Kelvin-Laplace equation (5.5):

$$r_c = \frac{-2\gamma M_l}{\rho_l RT ln(RH)} \tag{5.5}$$

Where r_c is the capillary pore radius, and γ is the surface tension of water.

If we return to sketch representing the simplified porous network, which was considered in chapter 4 to illustrate the material state during drying, Fig. 5.5 shows the created meniscus in red at each relative humidity level.

The proposed morpho-mathematical operations could be used to identify meniscus places in the generated porous network. Fig. 5.6 and equation (5.6) illustrate the set of morpho-mathematical operations in order to obtain the meniscus place at different relative humidity levels. In this technique V1 and V2 are the geodesic reconstruction results, and V3 is obtained as the results of the subtraction of these two networks. Then, parts connected outwards of V3 should be

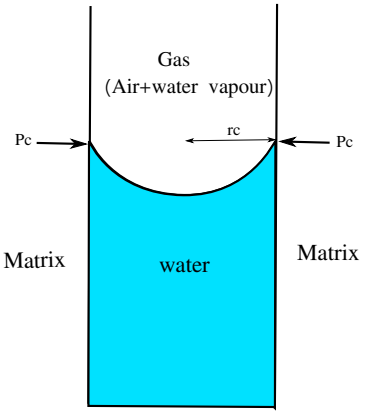

FIGURE 5.4: Sketch representing capillary pore

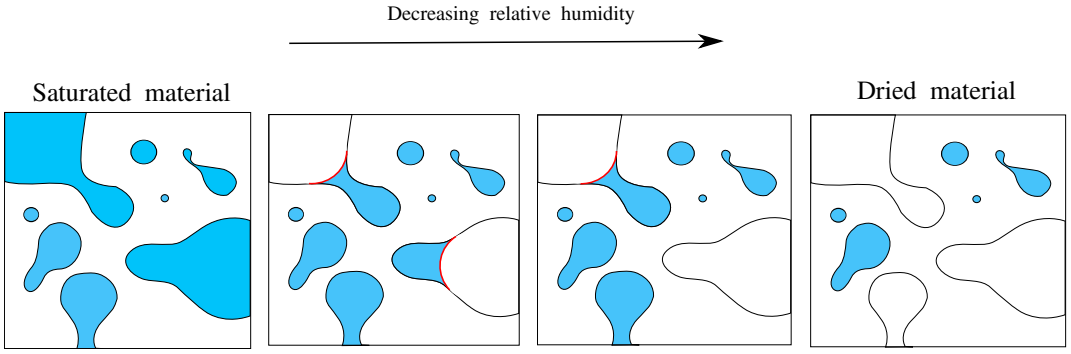

FIGURE 5.5: Sketch representing created meniscus in porous network by decreasing relative humidity

eliminated. For this purpose the geodesic reconstruction should be performed on V3 and finally after subtraction of reconstruction V3 from V3, V4 is obtained which gives volume of pores behind meniscus. In the next step, by applying the intersection between V4 and V2, the meniscus place is achieved. Fig. 5.7 also presents the same technique to distinguish the meniscus place at lower relative humidity.

$$\mathbf{M}_i = \big[(R_3(\mathbf{A} \bullet E_i) - R_3(\mathbf{A} \bullet E_{i+1})) - R_3\big(R(\mathbf{A} \bullet E_i) - R_3(\mathbf{A} \bullet E_{i+1})\big)\big] \cap R_3(\mathbf{A} \bullet E_{i+1}) \quad (5.6)$$

Where $\mathbf{A}$ is the morphological model, R_3 represents geodesic reconstruction with structuring element of size three voxels, $\mathbf{M}_i$ is a set representing meniscus places at relative humidity level i. It should be noted that each relative humidity level corresponds to a certain structuring element size (E_i).

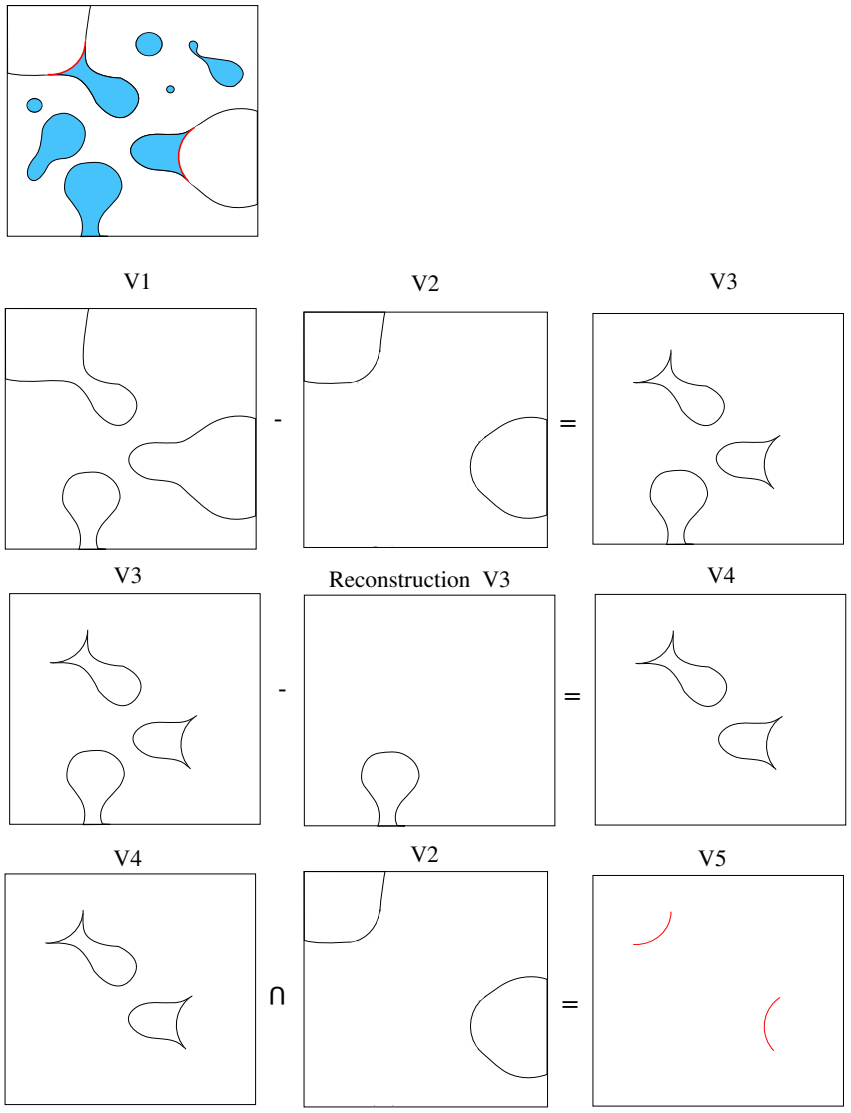

FIGURE 5.6: Filtering strategy to find the meniscus place (1)

By decreasing relative humidity, the value of capillary pressure increases. The volume of its application point initially increases and then decreases. Because in drying process at high relative humidity levels, volume of drained pores increases progressively and the volume where the meniscus are generated gradually increases. But at lower relative humidities, few parts of pores remain saturated, and there are few pores in which there is an interface between liquid and gas, thus, the volume where capillary pressure should be applied decreases.

5.3.2 Shrinkage due to disjoining pressure

Another applied pressure on solid surface which is considered in this study is disjoining pressure. It results from prevented adsorption in nanopores. Consequently, It should be applied in pores where their radius is smaller than adsorbed layer thickness (equation (5.7)) which has been discussed in section 4.7.

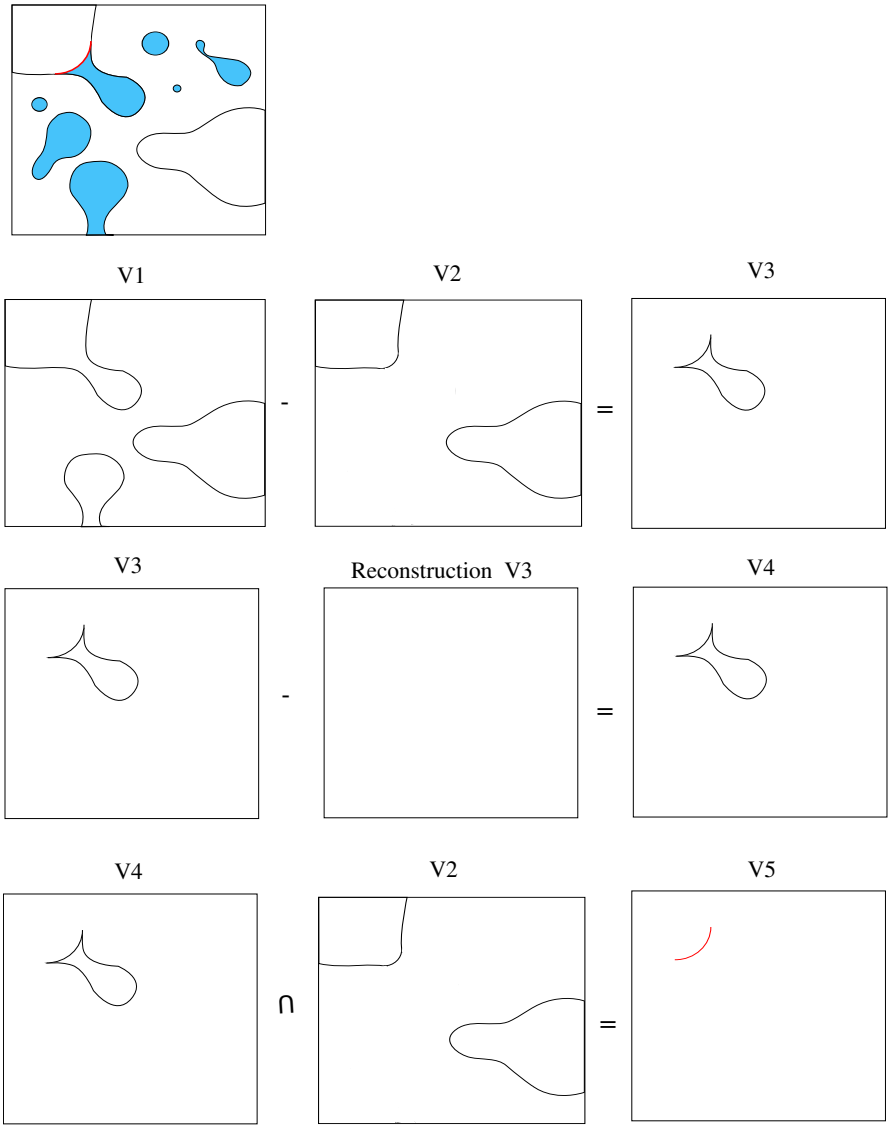

FIGURE 5.7: Filtering strategy to find the meniscus place (2)

$$\delta = 0.395 - 0.189ln(-ln(RH)) \tag{5.7}$$

At 100% relative humidity, this pressure has it maximal value. Then it gradually decreases as the relative humidity decreases, because the number of adsorbed water layer, corresponding to the free adsorption also decreases. The variation of disjoining pressure produces strain in the porous network. The expression for the variation of disjoining pressure Δp_d is similar to that of capillary pressure [96] ((5.9)).

$$\Delta P_d = \frac{\rho_a RT}{M_a} ln(RH) \tag{5.8}$$

TABLE 5.2: Disjoining pressure of water for different relative humidities at $T = 20°C$

RH (%)	ΔP_d	P_d
100	0	288.18
93.39	9.29	278.89
90.4	13.72	274.64
83	25.32	262.86
71.05	46.45	241.73
60.38	68.57	219.61
57.2	75.92	212.26
38.16	130.94	157.24
22	205.8	82.38
12	288.18	0

Where ρ_a is the density of adsorbed water and M_a is the molar mass of adsorbed water.

Table 5.2 shows the variation of disjoining pressure for water which should be applied in a porous network at $T = 20°C$ by decreasing relative humidity. In order to find the strain for each relative humidity level, the existing pressure in the porous network should be determined. If we suppose that at lowest relative humidity ($RH = 12\%$ in this case) all pores were drained and the disjoining pressure is zero, thus the maximum value of ΔP_d is equal to initial disjoining pressure at 100% relative humidity. This initial disjoining pressure is applied in pores smaller than 10 water molecules, because at $RH = 100\%$, 10 water molecules could be adsorbed on pores wall. Consequently, Table 5.2 shows the active disjoining pressure in porous network for each relative humidity level.

It should be noted that the disjoining pressure not only depends on relative humidity but also depends on the pores diameter [99]. At considered relative humidity level, by decreasing the pores diameter, the variation of disjoining pressure increases. It is related to the fact that by decreasing pore diameter, water molecules are subjected to more pressure and they impose more repulsive force on the pores wall to be adsorbed. Consequently, another term is added in order to consider the influence of pore diameter. The value of modified disjoining pressure considering pore size is obtained by equation (5.9).

$$P'_d = P_d(1 - \frac{d}{2\delta}) \tag{5.9}$$

Where d is the pores diameter and δ is the adsorbed layer thickness.

Fig. 5.8 shows the disjoining pressure distribution in different size of pores. In this table, the pore sizes which are labelled with (Dis) are pores with the diameter equal to 2δ obtained for each relative humidity. Disjoining pressure values in pores with different diameters were obtained using equation (5.9). It should be noted that the pores diameter are presented in voxels.

Once the active disjoining pressure distribution was determined in the porous network, the pores volume with same diameter should be obtained in order to recognize the accurate application point of each disjoining pressure value. Fig. 5.9 and equation (5.10) show the technique to find

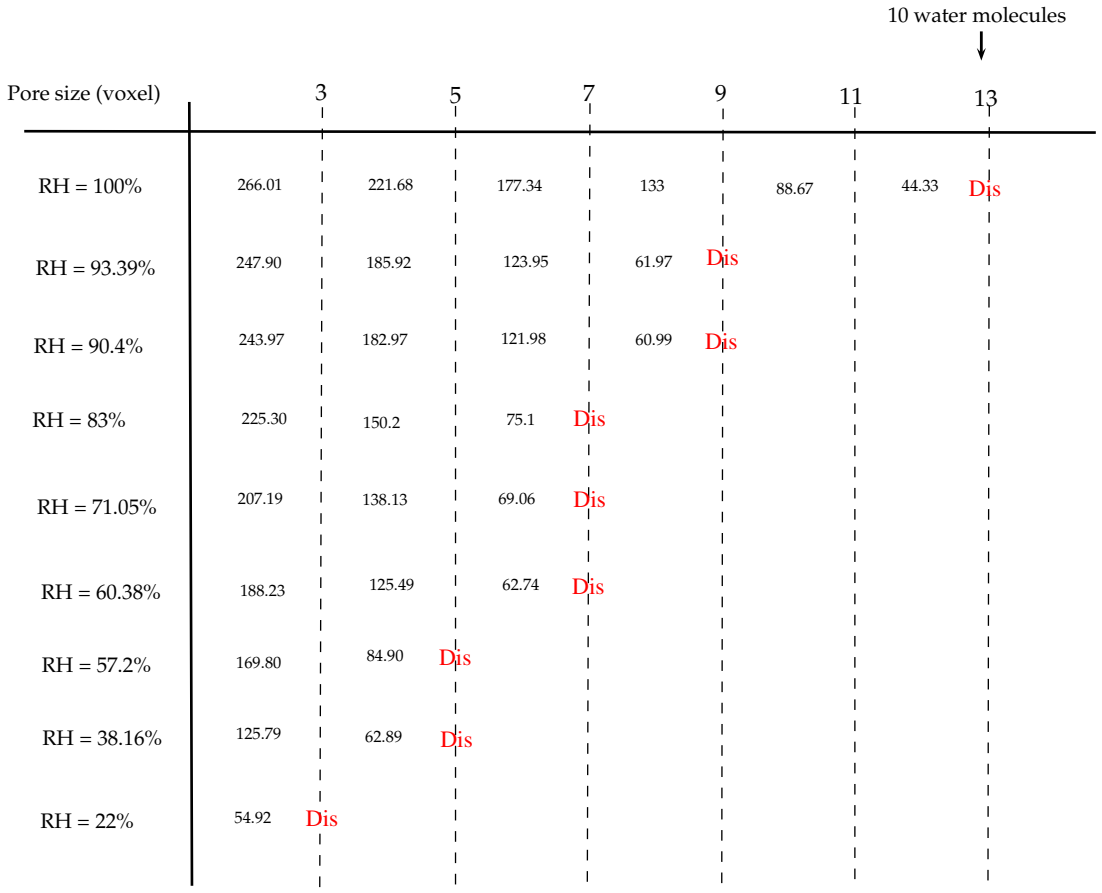

FIGURE 5.8: Disjoining pressure distribution (P'_d in MPa) in the porous network for different relative humidity levels

the volume of pores with same diameter in porous network. In this technique a subtraction is applied on the result of morphological opening with different structuring element sizes and the isolated pores.

$$\mathbf{V}_i = (\mathbf{A} \bullet E_i) - (\mathbf{A} \bullet E_{i+1}) - \big(\mathbf{A} - R_3(\mathbf{A})\big) \tag{5.10}$$

Where $\mathbf{V}_i$ is a set representing volume of pores with size i in a morphological model of $\mathbf{A}$.

As illustrated in Fig. 5.8, by decreasing relative humidity, the value of disjoining pressure decreases and should be applied to smaller volumes. Because during the drying process, pores volume with radius smaller than the adsorbed layer thickness (which is the application point of disjoining pressure) decreases.

5.3.3 Drying shrinkage estimation

In order to estimate the shrinkage induced due to drying, disjoining pressure and capillary pressure are considered as operative mechanisms in the porous network. Fig. 5.10 shows the

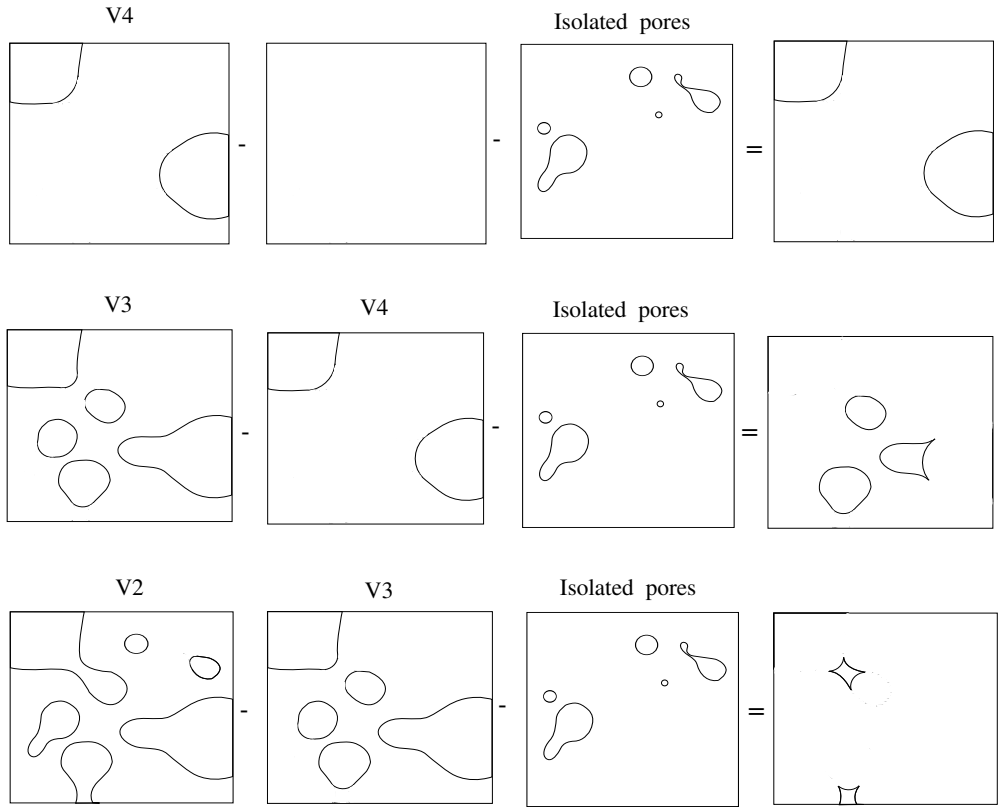

FIGURE 5.9: Filtering strategy to find pores with the same size in porous network

applied effort in a pore with a variable diameter at different relative humidities during drying process.

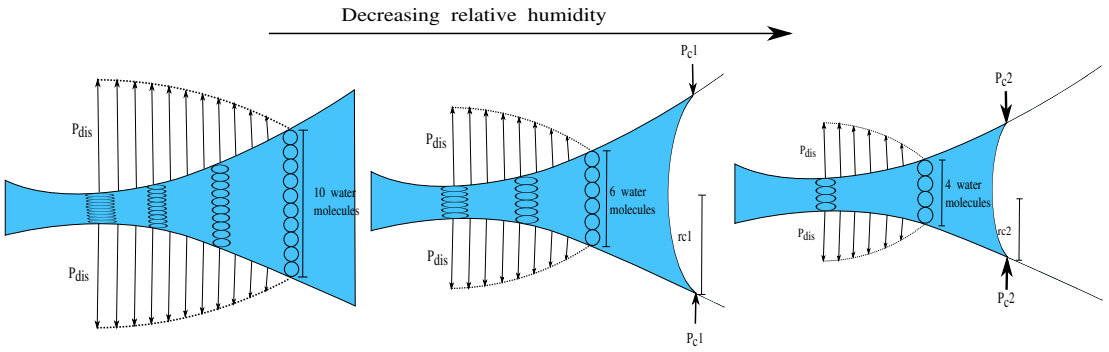

FIGURE 5.10: Sketch representing efforts induced due to drying

The value of disjoining pressure and capillary pressure could be determine at each relative humidity using before mentioned equations. The volume of pores with capillary meniscus and the volume of pores smaller than the adsorbed layer thickness could be obtained in numerical porous network using morpho-mathematical operations and then the value of elastic strain energy should be studied. Fig. 5.11 shows the distribution of hydro-mechanical efforts in different pore sizes by decreasing relative humidity in a porous network considering $T = 20°C$.

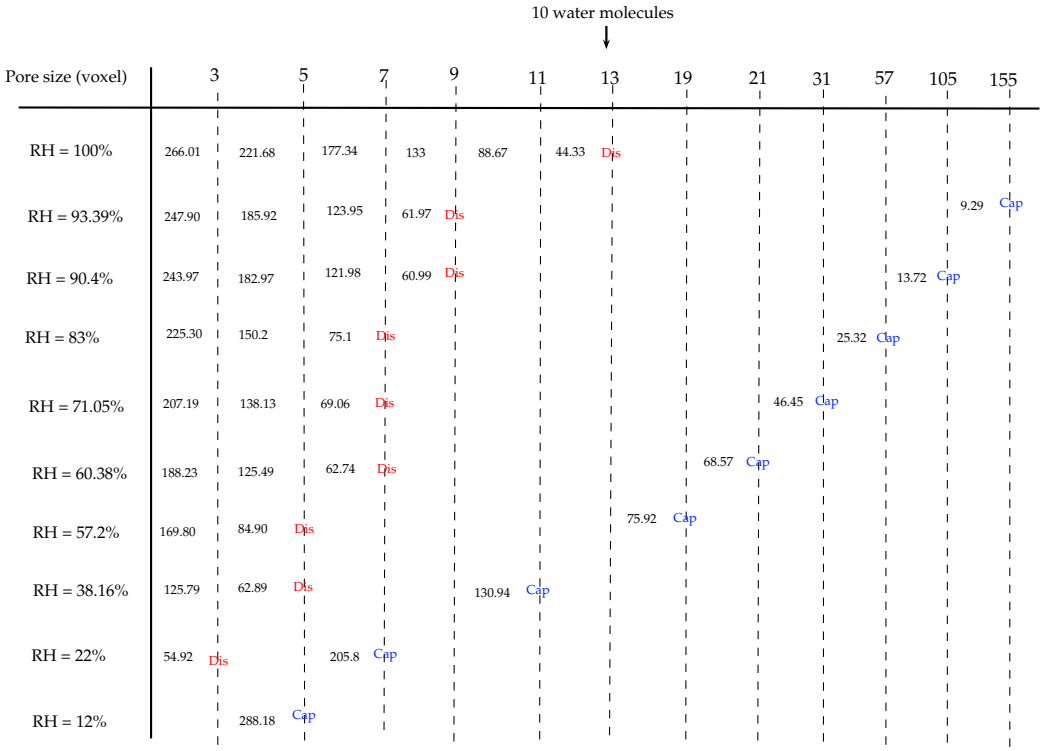

FIGURE 5.11: Distribution of hydro-mechanical forces (in MPa)

At each relative humidity level, knowing applied forces and the volume of fluid in which hydro-mechanical forces should be applied, elastic strain energy in fluid at microscopic scale could be estimated by equation (5.11).

$$E_e = \frac{1}{2} P V_p \tag{5.11}$$

Where P is applied pressure and V_p is the pore volume in which pressure is applied.

On the other hand, at the macroscopic scale the elastic strain energy is defined by equation (5.13).

$$E_e = \frac{1}{2} V \sigma \epsilon \tag{5.12}$$

$$= \frac{V}{2} \underline{\underline{\epsilon}} : \underline{\underline{\underline{\underline{C}}}} : \underline{\underline{\epsilon}} \tag{5.13}$$

Where V is the domain volume.

In isotropic states:

$$E_e = \epsilon_{rd}^2 \frac{V}{2} \underline{\underline{1}} : \underline{\underline{\underline{\underline{C}}}} : \underline{\underline{1}} \tag{5.14}$$

$$= \epsilon_{rd}^2 \frac{V}{2} (9\lambda + 6\mu) \tag{5.15}$$

By equality of elastic strain energy at microscopic and macroscopic scales, the evaluation of strain in terms of relative humidity could be estimated.

$$\frac{1}{2} V \epsilon_{rd}^2 (9\lambda + 6\mu) = \frac{1}{2} V_p P \tag{5.16}$$

When cement paste with $E = 10GPa$ and $\nu = 0.3$ is represented in a 2D porous network with the size of $1\mu m$ on each side, the strain due to drying could be calculated using equation (5.17):

$$\epsilon_{rd} = \sqrt{1.3 \times 10^{-5} P V_p} \tag{5.17}$$

Where P is pressure, and V_p is the pores volume in which the considered pressure is applied. By considering different values of P and V_p for different relative humidities, evaluation of strain during drying could be depicted.

Fig. 5.12 shows the obtained curve for one of the two dimensional numerical porous networks discussed in previous chapters, called MAT4 considering capillary pressure, Fig. 5.13 shows shrinkage considering disjoining pressure and Fig. 5.14 illustrates evaluation of strain considering the influence of both capillary pressure and disjoining pressure.

The variation of estimated shrinkage during drying is similar to experimental values. At relative humidity ranges between $40\% - 100\%$, the capillary pressure and disjoining pressure are the dominant phenomena and an increase of strain is obtained by decreasing relative humidity. But for the relative humidity levels lower than 40%, the dominant phenomenon is the surface energy. It was noted that in this study the influence of surface energy was neglected, thus, the numerical and experimental results do not match for relative humidities lower than 40%.

5.4 Sensitivity evaluation of shrinkage

In section 5.3, the procedure to estimate drying shrinkage considering the capillary pressure and disjoining pressure effects was discussed. In this method the hydro-mechanical efforts and their application points in the porous network are determined at microscopic scale. Regarding the proposed equations, the value of capillary pressure depends on both ambient temperature and relative humidity, but the variation of disjoining pressure and the volume of pores in which capillary pressure and disjoining pressure should be applied depends on the numerical porous

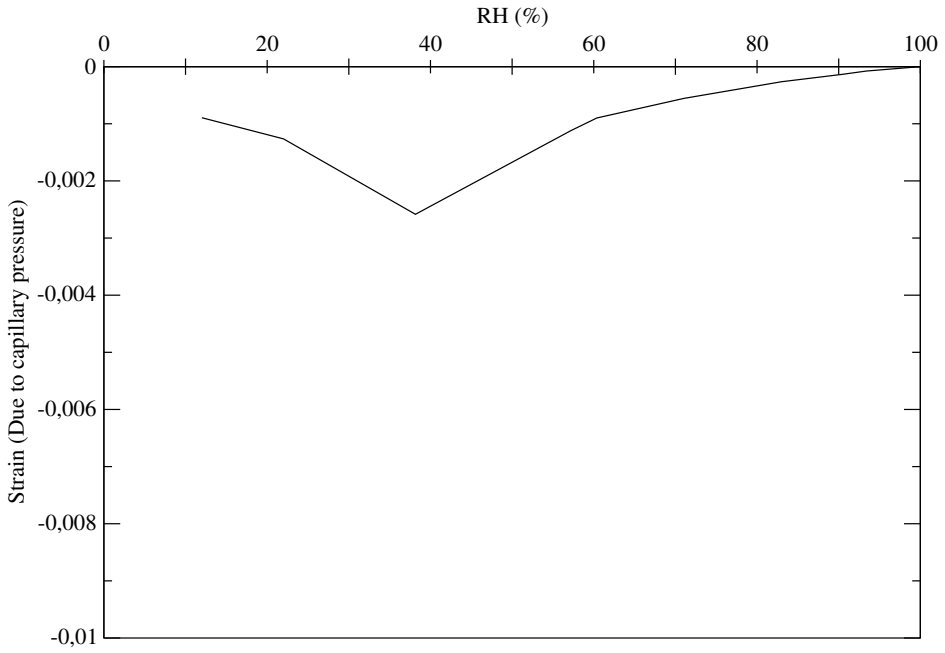

FIGURE 5.12: Estimated shrinkage due to capillary pressure in terms of relative humidity for 2D numerical porous network

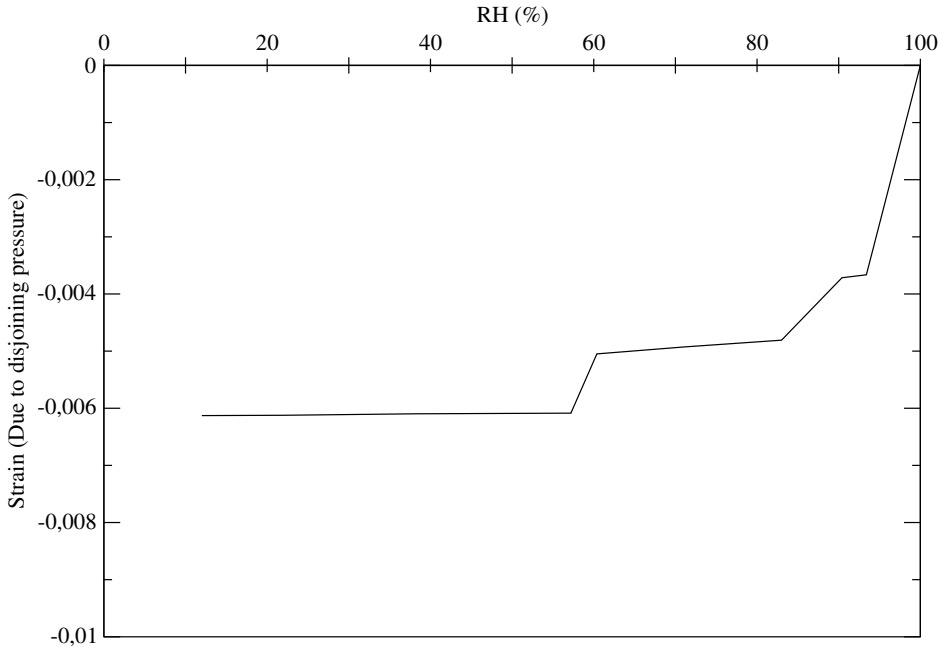

FIGURE 5.13: Estimated shrinkage due to disjoining pressure in terms of relative humidity for 2D numerical porous network

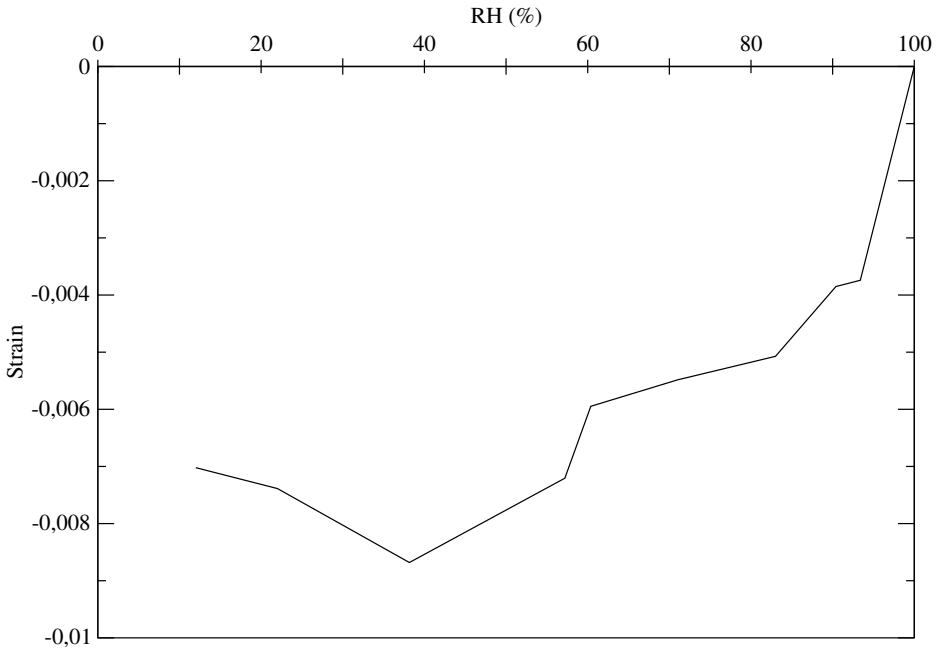

FIGURE 5.14: Estimated shrinkage in terms of relative humidity for 2D numerical porous network

network. The presented results in Fig. 5.12, Fig. 5.13 and Fig. 5.14 correspond to the porous network MAT4. In this section, in order to evaluate the sensitivity of estimated shrinkage, new porous networks are generated using the same Random Fields but in each case, one excursion set was eliminated. It should be noted that the value of porosity remains the same in all porous networks. Fig. 5.15, Fig. 5.16 and Fig. 5.17 illustrate the evaluation of drying shrinkage considering capillary pressure, disjoining pressure and both of them, respectively.

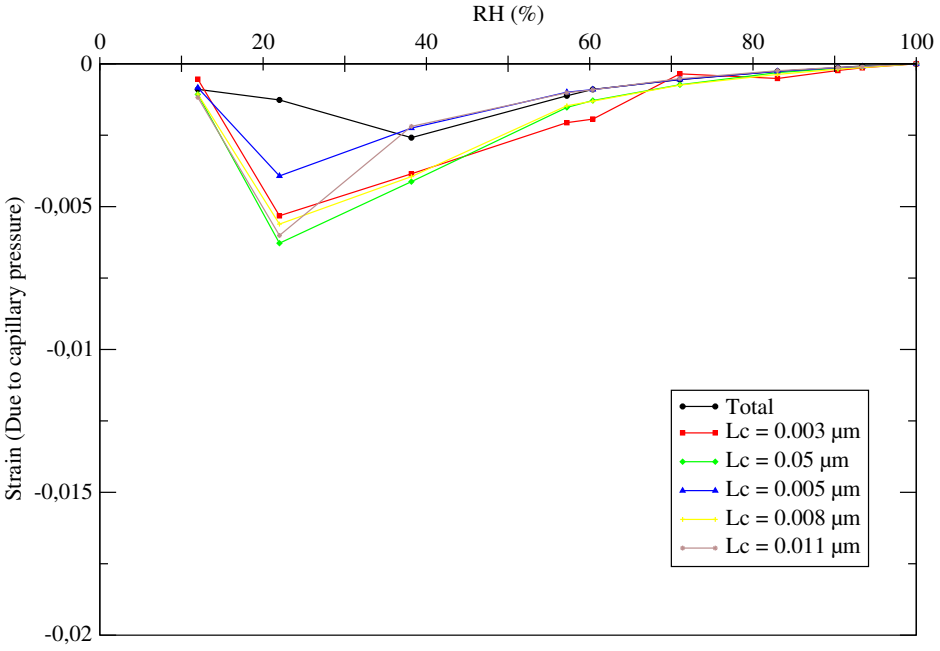

FIGURE 5.15: Influence of elimination of some Random Fields on shrinkage due to capillary pressure

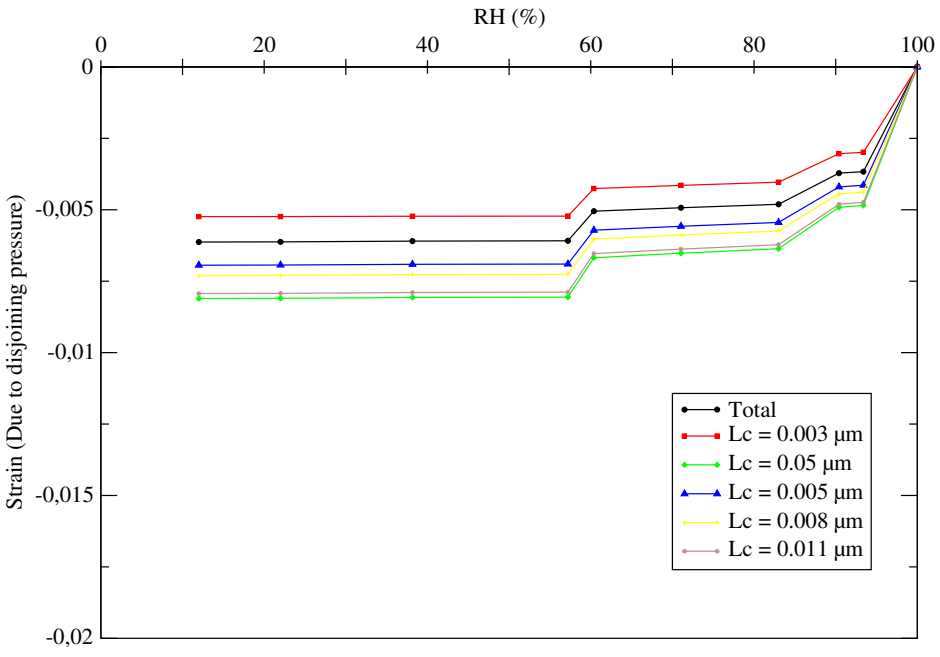

FIGURE 5.16: Influence of elimination of some Random Fields on shrinkage due to disjoining pressure

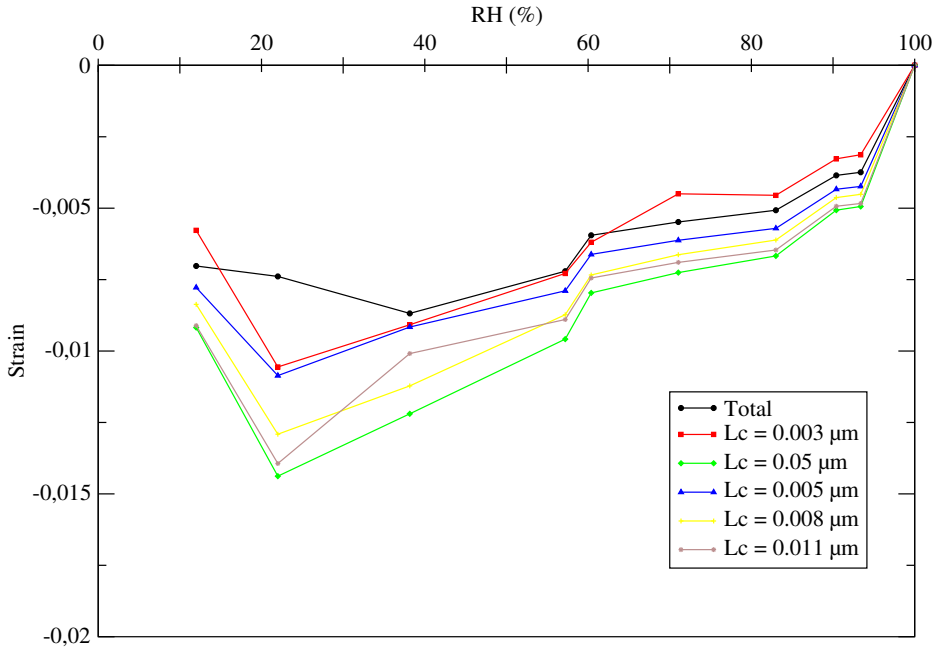

FIGURE 5.17: Influence of elimination of some Random Fields on estimated shrinkage

As previously discussed, changing the porous network directly influences the volume where the hydro-mechanical efforts should be applied. The application point of disjoining pressure is pores with radius smaller than the adsorbed layer thickness and at 100% relative humidity, 10 water molecules could be adsorbed by pores walls. By considering a water molecule diameter equal to be $2.6\mathring{A}$ thus the application point of disjoining pressure is always pores with diameter smaller than $26\mathring{A}$. In porous network generation, when Random Fields with small correlation lengths were eliminated, a noticeable parts of small pores were excluded in the obtained porous network. That is why, the strain due to disjoining pressure in Fig. 5.16 and consequently the total strain in Fig. 5.17 show a considerable decrease by elimination of Random Field with $L_c = 0.003\mu m$. Moreover, when the Random Field with large correlation length was eliminated (for example $L_c = 0.05\mu m$), the volume fraction of smaller pores increased in order to maintain the same porosity. In this case, the volume of small pores where disjoining pressure applies increases and consequently the obtained strain increases.

5.5 Conclusions

In the continue of hydric behaviour simulations of cement-based materials, the hydro-mechanical behaviour was discussed in this chapter and the following conclusions are reported:

- **Regarding the obtained results in chapter 4, the non-saturated porous network at each relative humidity was presented by a numerical image.**
- These images could be used in order to obtain dimensional variations due to drying.
- At this moment, it is not possible to apply finite element methods.
- Thus it is attempted to simulate dimensional variations based on the elastic analysis.
- The numerical simulations were performed considering capillary pressure and the variation of disjoining pressure as the origin of drying shrinkage at high relative humidities.
- The influence of surface energy which is the dominant phenomenon at low relative humidities was ignored.

General conclusions and perspectives

This thesis has been mainly dedicated to the modelling of hydro-mechanical behaviour of cement-based materials, especially cement paste. This consists of morphological modelling, image filtering, simulation of sorption-desorption isotherm and dimensional variations.

Before starting to model the morphology itself, we have to know the structure of cement-based materials, in order to establish a realistic representation of the structure by the morphological modelling. This proves to be a hard task, because these materials porous network are very complex. The porous networks structure strongly depends on the formulation of material and also the environmental condition the material is facing. It also changes over time. The modifications begin from the hydration process and continue during curing time, and even more throughout its lifetime.

Cement paste is not neutral to its environment and is influenced by environmental conditions. Therefore, a review of the hydric behaviour of cement-based materials is presented in chapter 1. It clearly shows that the complexity of hydro-mechanical behaviour at marcosacle comes from the complexity of the porous network. Hence, the best solution to represent this complex porous structure remains in determination of the exact morphology using experimental techniques. Due to limitations of experimental techniques for the use of 3D imaging in nanoporous networks, numerical methods are being employed. Although various models have been proposed, they suffer from too much simplifications regarding the porous network. Therefore, the primary objective of this thesis has been dedicated to make a realistic model of nanoporous materials using the morphological modelling.

Chapter 2 focuses on the morphological modelling of heterogeneous materials by the use of excursion sets of Random Fields. This allowed us to construct a completely random porous network using only four parameters. These parameters are mean, variance, correlation length and threshold. The geometrical and topological properties of the generated model could also be controlled using this technique. Moreover, the union of several excursion sets with different correlation lengths was also feasible. So that, a wide range of pores size and distribution could be reproduced.

Nevertheless, there are some shortcomings in this method. Random Fields should be simulated by using a proper program such as 'R'. Hence we took advantage of 'R' program to generate a 2D porous network with 25×10^6 points in the domain with a grid size of $0.2nm$. Furthermore, in the proposed approach to create Random Fields, the covariance function is needed to be taken into consideration. However, in this thesis Gaussian covariance function was considered. **Still, a real image of the porous space using experimental techniques could help to choose a proper covariance function**[1]**.**

Morpho-mathematical operations such as opening and geodesic reconstruction for image filtering were launched to analyse the 2D generated morphological modelling. A 2D representation is not acceptable, because the percolation threshold in 2D is about 50%. Thus, in order to have a

[1] Perspectives are noted in bold.

connected porous network, the porosity should be increase up to 50% which is too much for cement paste.

Subsequently, in chapter 3, the morphological model was extended in 3D to represent the real material. This extension permitted to obtain a better pore distribution when compared to porosimetry results. However, the 3D morphological modelling proved to have inadequate accuracy due to the grid size. In 3D the porous network voxel size is $1.125nm$. This voxel size does not allow to properly detect pores connections, while in order to detect pores connectivity, geodesic reconstruction is applied considering structuring element of size three voxels.

After modelling the porous network and taking advantage of morpho-mathematical tools, it became possible to study the hydric behaviour of cement paste, and simulation of sorption-desorption isotherm were performed in chapter 4. To simulate the hydric behaviour of cement paste, an image filtering associated with the related physical phenomena was performed on the morphological model. To this aim, Kelvin-Laplace law and the adsorption layer were linked to a structuring element size. The pores outwards connectivity were checked by making use of the geodesic reconstruction.

In drying process, capillarity, which was chosen as the main physical phenomenon acting on the porous network, was well represented by the image filtering, and illustrated the sensitivity of the resulted isotherm to the changes of morphological model. However, there is a very complex and implicit link established between chosen parameters and the obtained results, making it difficult to properly control the system. There is also a difference between the numerical results when compared to experimental ones. This is due to the limitations of mercury intrusion test in detecting small pores. Thus, the morphological model which was created from the information of porosimetry test, lacks of small pores, which have an undeniable role in the drying and wetting process. Although we managed to add these omitted pores, however, there is no guaranty that it fulfils the real volume fraction these pores occupy. **Moreover, smaller grid size are required in case of 3D simulations. Therefore, in order to obtain more comparable numerical results, the morphological models should be generated by smaller voxel size.** This would increase the accuracy of morpho-mathematical operations and leads to more appropriate results.

In the wetting process a considerable hysteresis was observed. In one hand, it approves the existence of ink-bottle pores, however, on the other hand, it showed that the modelled isotherm is more related to mercury intrusion results than water sorption. To simulate wetting process, apart from capillarity, diffusion has to be taken into account as a key phenomenon. Some tests have been accomplished adding a simplified diffusion of water into ink-bottle pores. Although simulations were not directly compared with experimentations, however, the results showed a good trend with them. **In future works it would be more appropriate to consider a more realistic representation of diffusion process.**

In general, numerical simulations are convincing and encouraging. They show a good agreement between the delicacy of geometry and simplicity of physical phenomena, despite ignoring transient fluid transfer equations. The influence of physical parameters (such as temperature) were taken into account naturally. The morphological model and the isotherm were numerically

linked together. However, it is complicated to control the link between them, once again this link is complicated to control. **In future works, this could be attempted to be controlled through new introduced parameters.** It should be underlined that one of the outlines of this thesis was to put the emphasise on the real structure of the material without any assumption on pores shape. Now that this has been accomplished, **a further step in to use of more realistic presentation of the associated physical phenomena.**

In chapter 5, hydro-mechanical behaviour of cement-based materials is examined. Regarding the obtained results in chapter 4, the non-saturated porous network at each relative humidity was presented by a numerical image. Obviously these images could be used in order to obtain drying shrinkage. **Finite Element method is a proper way to calculate the strain induced by mechanical drying forces applied on the material. However, this method has been put aside in this thesis, due to sharpness of the morphological grid, and should be considered in the future works.** Instead, the drying shrinkage was computed on a fully elastic analysis. The numerical simulations were performed considering capillary pressure and the variation of disjoining pressure as the origin of drying shrinkage at high relative humidities. **The influence of surface energy which is the dominant phenomenon at low relative humidities was neglected in this thesis, and should be considered in future works.**

From a general point of view, in this thesis a porous network has been modelled using morphological modelling, and hydro-mechanical behaviour of cement-based materials especially cement paste have been simulated making use of image filtering. Aside from the fact that still some improvements are needed in order to be fully able to compare results with experimentations, numerical results illustrate a good trend regarding simplifications done all along this thesis. This proves that the hypothesis made in this thesis about the fact that the complexity of behaviour comes from the complexity of the porous network is relevant.

Appendix A

'R' script

The following script was written in 'R' to generate a 3D Random Fields in a domain of $1\mu m$ considering zero for mean and $\sigma^2 = 1$, $L_c = 0.008\mu m$ in a mesh with 800 points on each side.

```
library('RandomFields')
size <- 1.0          →          Size of cube
steps <- 0.00125          →          Discretization
mean <- 0.0
variance <- 1.0
nugget <- 0
scale <- 0.008          →          Correlation length
method = 'TBM3'          →          Turning bands
model <- "stable"
alpha <- 2
param <- c(mean, variance, nugget, scale, alpha)
x <- seq(0, size, steps)
y <- seq(0, size, steps)
z <- seq(0, size, steps)
cat("GENERATING RANDOM FIELD... ")
f <- GaussRF(method=method, x=x, y=y, z=z, model=model, grid=TRUE, param=param)
cat("DONE.\n")
cat("GENERATING VTK FILE... ")
source("CreateVTKFile.R")
CreateVTKFile(f,size,3)
cat("DONE.\n")
cat("GENERATING DAT FILE... ")
source("CreateDATFile.R")
CreateDATFile(f,size)
cat("DONE.\n")
```

Bibliography

[1] T. Rougelot. *Etude expérimentale multi-échelles des couplages hydriques, mécaniques et chimiques dans les matériaux cimentaires.* PhD thesis, Lille 1, 2008.

[2] Q. Wu. *Isothermes de désorption de matériaux cimentaires : étude d'un protocole accéléré et estimation du VER.* PhD thesis, Lille 1, 2014.

[3] G. Matheron. L'émergence de la loi de darcy. in: Marsily, g. de "ecoulement dans les milieux poreux ou fissurés. *Annales des Mines*, pages 11–16, 1984.

[4] P. Lehmann A. Peters A. Kaestner M. Krafczyk W. Durner B. Ahrenholz, J. Tölke. Prediction of capillary hysteresis in a porous material using lattice-Boltzmann methods and comparison to experimental data and a morphological pore network model. *Advances in Water Resources*, 31:1151–1173, 2008.

[5] P.M. Adler. *Porous media: Geometry and transport.* butterworth-heinemann, 1992.

[6] D. Aubry M. Degrange E. Vennat, J.P. Attal. Three-dimensional pore-scale modelling of dentinal infiltration. *Computer Methods in Biomechanics and Biomedical Engineering*, 17 (6):632–642, 2014.

[7] M. Degrange E. Vennat, D. Aubry. Collagen fiber network infiltration : permeability and capillary infiltration. *Transport in Porous Media*, 84(3):717–733, 2010.

[8] J.J. Thomas J.E. Andrade J.J. Chen G.W. Scherer H.M. Jennings, J.W. Bullard. Characterization and Modeling of Pores and Surfaces in Cement Paste :Correlations to Processing and Properties::Correlations to Processing and Properties. *ACT*, 6(1):5–29, 2008.

[9] B. Bary. A polydispersed particle system representation of the porosity for non-saturated cementitious materials. *Cement and Concrete Research*, 36(11):2061–2073, 2006.

[10] C.T. Miller M. Hilpert. Pore-morphology-based simulation of drainage in totally wetting porous media. *Advances in Water Resources*, 24(3–4):243–255, 2001.

[11] A. Sellier X. Bourbon H. Ranaivomanana, J. Verdier. Toward a better comprehension and modeling of hysteresis cycles in the water sorption-desorption process for cement based materials. *Cement and Concrete Research*, 41:817–827, 2011.

[12] R.J. Adler. Some new random field tools for spatial analysis. *Stochastic Environmental Research and Risk Assessment*, 22:809–822, 2008.

[13] E. Roubin. *Modélisation EF et morphologique de milieux hétérogènes á l'échelle mésoscopique : applications aux matériaux á matrice cimentaire.* PhD thesis, Ecole Normale Supérieure de Cachan, 2013.

[14] M. Bogdan. *Modélisation morphologique multi-échelles des matériaux cimentaires : Application à la prédiction de propriétés effectives de diffusion.* PhD thesis, Ecole Normale Supérieure de Cachan, 2015.

[15] G. W. Horgan C. A. Glasbey. *Image Analysis for the Biological Sciences.* Wiley, 1995.

[16] M. Szczesniak. *Influence of aggregate diameter and various water saturation degrees on cement based composites behavior.* PhD thesis, Universite des Science et Technologies de Lille, 2009.

[17] F. Skoczylas I. Yurtdas, N. Burlion. Triaxial mechanical behaviour of mortar: Effects of drying. *Cement and Concrete Research*, 34:1131–1143, 2004.

[18] F. Brue. *Roles de la temerature et de la composition sur le couplage thermo-hydro-mecanique des betons.* PhD thesis, Lille 1, 2009.

[19] V. Baroghel-Bouny. *Caractérisation microstructurale et hydrique des pâtes de ciment et des bétons ordinaires et à très hautes performances.* PhD thesis, Ecole Nationale des Ponts et Chaussées, 1994.

[20] I. Yurtdas. *Couplage comportement mecanique et dessiccation des materiaux a matrice cimentaire: Etude experimentale sur mortiers.* PhD thesis, Lille 1, 2003.

[21] R. Sauterey J. Baron. *Le Béton hydraulique, connaissance et pratique.* Presses de l'E.N.P.C., 1982.

[22] P. Acker. *Retraits et fissurations du béton: Causes, mécanismes, modèles.* AFPC, 1991.

[23] R. Lanchon R. Dupain. *Granulats, sols, ciments et bétons: caractérisation des matériaux de génie civil par les essais de laboratoire.* Ed. Casteilla, 1995.

[24] A.M. Neville. *Propriétés des bétons.* Eyrolles, 2000.

[25] T. Kasai E.I. Tazawa, S. Miyazawa. Chemical shrinkage and autogenous shrinkage of hydrating cement paste. *Cement and Concrete Research*, 25:288–292, 1995.

[26] P.F. Hansen O.M. Jensen. Water-entrained cement-based materials: I. Principles and theoretical background. *Cement and Concrete Research*, 31:647–654, 2001.

[27] T.C. Hansen. Physical structure of hardened cement paste. A classical approach. *Materials and Structures*, 19:423–436, 1986.

[28] H.J.H. Brouwers. The work of Powers and Brownyard revisited: Part 1. *Cement and Concrete Research*, 34:1697–1716, 2004.

[29] H.F.W. Taylor. *Cement Chemistry.* Thomas Telford Publishing, 2 edition edition, 1997.

[30] T.L. Brownyard T.C. Powers. Studies of the Physical Properties of Hardened Portland Cement Paste. *Journal Proceedings*, 43(9):249–336, 1946.

[31] R.J. Kirkpatrick X. Cong. 17o MAS NMR Investigation of the Structure of Calcium Silicate Hydrate Gel. *Journal of the American Ceramic Society*, 79(6):1585–1592, 1996.

[32] R.J. Kirkpatrick X. Cong. 29si and 17o NMR investigation of the structure of some crystalline calcium silicate hydrates. *Advanced Cement Based Materials*, 3(3–4):133–143, 1996.

[33] I.G. Richardson G.W. Groves A.R. Brough, C.M. Dobson. Application of Selective 29si Isotopic Enrichment to Studies of the Structure of Calcium Silicate Hydrate (C-S-H) Gels. *Journal of the American Ceramic Society*, 77(2):593–596, 1994.

[34] P.L. Pratt H.M. Jennings, B.J. Dalgleish. Morphological Development of Hydrating Tricalcium Silicate as Examined by Electron Microscopy Techniques. *Journal of the American Ceramic Society*, 64(10):567–572, 1981.

[35] P. J. Sereda R. F. Feldman. A New Model for Hydrated Portland Cement and Its Practical Implications. *Eng. J.*, 53(8), 1970.

[36] F.H. Wittmann. The structure of hardened cement paste - a Basis for a better understanding of the materials properties. *Cement and Concrete Association*, 1976.

[37] H.F.W. Taylor. Proposed Structure for Calcium Silicate Hydrate Gel. *Journal of the American Ceramic Society*, 69(6):464–467, 1986.

[38] H.M. Jennings. Refinements to colloid model of C-S-H in cement: CM-II. *Cement and Concrete Research*, 38(3):275–289, 2008.

[39] R. Sierra. *Contribution à l'étude de l'hydratation des silicates calciques hydrauliques.* L.C.P.C., 1974.

[40] P.J. Sereda R.F. Feldman. A model for hydrated Portland cement paste as deduced from sorption-length change and mechanical properties. *Matériaux et Construction*, 1(6):509–520, 1968.

[41] L. Granger. *Comportement différé du béton dans les enceintes de centrales nucléaires : analyse et modélisation.* PhD thesis, Ecole Nationale des Ponts et Chaussées, 1995.

[42] M. Mainguy. *Modèles de diffusion non linéaire en milieux poreux. Applications a la dissolution et au séchage des matériaux cimentaires.* PhD thesis, Ecole Nationale des Ponts et Chaussées, 1999.

[43] J. Baron. *Le beton hydraulique - Connaissance et pratique - 6eme partie : Durabilite ; Chapitre 27 : Les retraits de la pate de ciment.* 1982.

[44] F.H. Wittmann Z.P. Bazant. *Creep and Shrinkage in Concrete Structures.* John Wiley and Sons, 1982.

[45] P. Acker. *Comportement mécanique du béton ; apports de l'approche physico-chimique.* 1988.

[46] J.F. Shao F. Bourgeois, N. Burlion. Modelling of elastoplastic damage in concrete due to desiccation shrinkage. *International Journal for Numerical and Analytical Methods in Geomechanics*, 26(8):759–774, 2002.

[47] Z.P. Bazant. *Mechanics of Geomaterials: Rocks, Concretes, Soils*. John Wiley & Sons Ltd, 1st ed. edition edition, 1985.

[48] T.C. Powers. The thermodynamics of volume change and creep. *Matériaux et Construction*, 1:487–507, 1968.

[49] F. Wittmann. Surface tension skrinkage and strength of hardened cement paste. *Matériaux et Constructions*, 1:547–552, 1968.

[50] J. Godin V. Baroghel-Bouny. *Experimental study on drying shrinkage of ordinary and high-performance cementitous materials*. 2000.

[51] J.G.M. Van Mier J. Bisschop, L. Pel. Effect of aggregate size and paste volume on drying shrinkage microcracking in cement-based composites. *in Creep, Shrinkage and Durability Mechanics of Concrete and other Quasi-Brittle Materials*, pages 75–80, 2001.

[52] A. Djerbi M. Kaczmarek Z. Lafhaj, M. Goueygou. Correlation between porosity, permeability and ultrasonic parameters of mortar with variable water/cement ratio and water content. *Cement and Concrete Research*, 36:625–633, 2006.

[53] S.T.A. Ödman. Effects of variations in volume, surface area exposed to drying, and composition of concrete on shrinkage. *RILEM/CEMBUREAU Int. Colloquium on the Shrinkage of Hydraulic Concretes*, 1968.

[54] H. Ranaivomanana. *Transferts dans les milieux poreux réactifs non saturés : application á la cicatrisation de fissure dans les matériaux cimentaires par carbonatation*. PhD thesis, Université de Toulouse, 2010.

[55] P.M. Adler C. Varloteaux, S. Békri. Pore network modelling to determine the transport properties in presence of a reactive fluid: From pore to reservoir scale. *Advances in Water Resources*, 53:87–100, 2013.

[56] Q.H. Do. *Modelling Properties of Cement Paste from Microstructure: Porosity, Mechanical Properties, Creep and Shrinkage*. PhD thesis, EPFL (Lausanne), 2013.

[57] A.P. Sheppard W.V. Pinczewski W.B. Lindquist A. Venkatarangan L. Paterson R.M. Sok, M.A. Knackstedt. Direct and stochastic generation of network models from tomographic images; effect of topology on residual saturations. *Transport in Porous Media*, 46:345–371, 2002.

[58] A. Venkatarangan W.B. Lindquist. Investigating 3d geometry of porous media from high resolution images. *Physics and Chemistry of the Earth, Part A: Solid Earth and Geodesy*, 24:593–599, 1999.

[59] H. Dong O. Gharbi S. Iglauer P. Mostaghimi A. Paluszny C. Pentland M.J. Blunt, B. Bijeljic. Pore-scale imaging and modelling. *Advances in Water Resources*, 51:197–216, 2013.

[60] E. Rosenberg S. Youssef. Quantative 3d characterisation of the pore space of real rocks: Improved µ-ct resolution and pore extraction methodology. *International Symposium of the Society of Core Analysts Calgary*, 2007.

[61] C.J. Jacquin W.B. Lindquist K.W. Jones P.M. Adler P. Spanne, J.F. Thovert. Synchrotron computed microtomography of porous media: Topology and transports. *Physical review letters*, 73:2001–2004, 1994.

[62] D. Stoyan A. Bezrukov, M. Bargieł. Statistical Analysis of Simulated Random Packings of Spheres. *Particle & Particle Systems Characterization*, 19(2):111–118, 2002.

[63] D. Stoyan A. Bezrukov. Simulation and Statistical Analysis of Random Packings of Ellipsoids. *Particle & Particle Systems Characterization*, 23(5):388–398, 2006.

[64] R.J. Adler. *The Geometry of Random Fields*. Society for Industrial and Applied Mathematics (SIAM), 1981.

[65] H. Federer. Curvature measures. *Transactions of the American Mathematical Society*, 93 (3):418–491, 1959.

[66] J.E. Taylor R.J. Adler. *Random Fields and Geometry*. Springer Monographs in Mathematics, 2007.

[67] P.J. Menck M. Schlather, A. Malinowski. Analysis simulation and prediction of multivariate random fields with package randomfields. *Journal of Statistical Software*, 63(8), 2015.

[68] C. Lantuéjoul. *Geostatistical Simulation*. Springer Berlin Heidelberg, 2002.

[69] J.E. Taylor and R.J. Adler. Gaussian processe, kinematic formulae and Poincaré's limit. *The annals of probability*, 37:1459–1482, 2009.

[70] K. Robinson. Morphological reconstruction: A downhill filter. 2007.

[71] C. Ronse. Reconstructing masks from markers in non-distributive lattices. *Applicable Algebra in Engineering, Communication and Computing (AAECC)*, 19:51–85, 2008.

[72] D. Jacob. *Caractérisation microstructurale des matériaux: vers une diffraction électronique quantitative*. PhD thesis, Lille 1, 2010.

[73] A.M. Minor C.A. Volkert. Focused ion beam microscopy and micromachining. *MRS Bulletin*, 32, 2007.

[74] Z.M. Wang. *FIB nanostructures*. Springer, 2013.

[75] T. Zhang. *Imagerie multi-résolution par tomographie aux rayons X : application à la tomographie locale en science des matériaux*. PhD thesis, Gronoble, 2006.

[76] C.J. Jacquin W.B. Lindquist K.W. Jones P.M. Adler P. Spanne, J.F. Thovert. Synchrotron computed microtomography of porous media: Topology and transports. *Physical Review Letters*, 73(14):2001–2004, 1994.

[77] N.S. Martys D.P. Bentz. Hydraulic radius and transport in reconstructed model three-dimensional porous media. *Transport in Porous Media*, 17:221–238, 1994.

[78] F. Brue F. Skoczylas C.A. Davy X. Bourbon J. Talandier W. Chen, J. Liu. Water retention and gas relative permeability of two industrial concretes. *Cement and Concrete Research*, 42:1001–1013, 2012.

[79] C. Wu Y. Feng Q. Meng C. Feng, H. Janssen. Validating various measures to accelerate the static gravimetric sorption isotherm determination. *Building and Environment*, 69:64–71, 2013.

[80] S. Poyet. Experimental investigation of the effect of temperature on the first desorption isotherm of concrete. *Cement and Concrete Research*, 39(11):1052–1059, 2009.

[81] C.A. Davy W. Chen F. Agostini F. Skoczylas X. Bourbon X.T. Chen, T. Rougelot. Experimental evidence of a moisture clog effect in cement-based materials under temperature. *Cement and Concrete Research*, 39:1139–1148, 2009.

[82] C. Gallé. Effect of drying on cement-based materials pore structure as identified by mercury intrusion porosimetry: A comparative study between oven-, vacuum-, and freeze-drying. *Cement and Concrete Research*, 31:1467–1477, 2001.

[83] L. Franke R.M. Espinosa. Inkbottle pore-method: Prediction of hygroscopic water content in hardened cement paste at variable climatic conditions. *Cement and Concrete Research*, 36:1954–1968, 2006.

[84] M. Mesa J. Restrepo A. Ramírez, L. Sierra. Simulation of nitrogen adsorption–desorption isotherms. hysteresis as an effect of pore connectivity. *Chemical Engineering Science*, 60: 4702–4708, 2005.

[85] S. Diamond. Mercury porosimetry: An inappropriate method for the measurement of pore size distributions in cement-based materials. *Cement and Concrete Research*, 30:1517–1525, 2000.

[86] J.W. Mc Bain. An explanation of hysteresis in the hydration and dehydration of gels. *Journal of American Chemical Society*, 57:699–700, 1935.

[87] V. Baroghel-Bouny. Water vapour sorption experiments on hardened cement based materials, part i: essential tool for analysis of hygral behaviour and its relation to pore structure. *Cement and Concrete Research*, 37:414–437, 2007.

[88] K. P. Lura, K. Van Breugel. *Autogenous Deformation and Internal Curing of Concrete*. Delft University Press, 2003.

[89] P.M. Michaud. *Vers une approche chimio-poro-visco-elastique du comportement au jeune age des betons*. PhD thesis, l'Ecole Nationale de Sciences Appliquées de Lyon, l'Université Laval, 2006.

[90] D.A. Quenard D.P. Bentz, E.J. Garboczi. Modelling drying shrinkage in reconstructed porous materials: application to porous vycor glass. *Modelling and Simulation in Materials Science and Engineering*, 6:211, 1998.

[91] M.J. Setzer R. Badmann, N. Stockhausen. The statistical thickness and the chemical potential of adsorbed water films. *Journal of Colloid and Interface Science*, 82:534–542, 1981.

[92] F. Benboudjema. Modélisation des déformations différées du béton sous sollicitations biaxiales : application aux enceintes de confinement de bâtiments réacteurs des centrales nucléaires, 2002.

[93] S. Zhutovsky K. Kovler. Overview and Future Trends of Shrinkage Research. *Materials and Structures*, 39(9):827–847, 2012.

[94] P. Mounanga. *Étude expérimentale du comportement de pâtes de ciment au très jeune âge : hydratation, retraits, propriétés thermophysiques*. PhD thesis, l'Université de Nantes, 2003.

[95] R.I. Razouk D.H. Bangham. Adsorption and the wettability of solid surfaces. *Trans. Faraday Soc.*, 33:1459–1463, 1937.

[96] L.J. Najjar Z.P. Bažant. Nonlinear water diffusion in nonsaturated concrete. *Matériaux et Construction*, 5(1):3–20, 1972.

[97] I. Soroka. *Portland Cement Paste and Concrete*. Macmillan, 1979.

[98] J.F. Shao N. Burlion, F. Bourgeois. Effects of desiccation on mechanical behaviour of concrete. *Cement and Concrete Composites*, 27:367–379, 2005.

[99] J.J. Beaudoin V.S. Ramachandran, R.F. Feldman. *Concrete Science: A Treatise on Current Research*. Heyden, 1982.